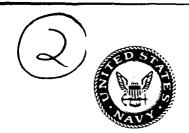


hington, DC 20375-5000



AD-A239 780

NRL Memorandum Report 6870

Advanced Concepts Theory Annual Report 1990

Final Report

Radiation Hydrodynamics Branch Plasma Physics Division



August 16, 1991

*Original comming ealer places: All DIIC respondencefond will be in black and white!

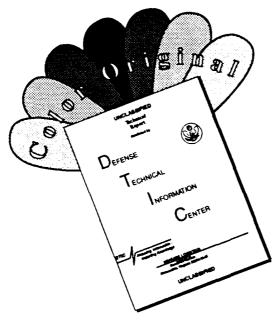
This research was sponsored by the Defense Nuclear Agency under Subtask RL RA/Advanced Technology Development, and Work Unit Title, 00079, "Advanced Technology Development," MIPR No. 90-580.

91-09040

Approved for public release; distribution unlimited.

91 8 27 071

DISCLAIMER NOTICE



THIS DOCUMENT IS BEST QUALITY AVAILABLE. THE COPY FURNISHED TO DTIC CONTAINED A SIGNIFICANT NUMBER OF COLOR PAGES WHICH DO NOT REPRODUCE LEGIBLY ON BLACK AND WHITE MICROFICHE.

REPORT DOCUMENTATION PAGE

Form Approved OMB No. 0704-0188

Public reporting burden for this collection of information is estimated to average 1 hour per response, including the time for reviewing instructions, searching existing data sources, gathering and maintaining the data needed, and completing and reviewing the collection of information. Send comments regarding this burden estimate or any other aspect of this collection of information, including suggestions for reducing this burden to Washington Headquarters Services, Directorate for information Operations and Reports, 1215 Jefferson Davis Holdway, Suret 1204, Arthroton, VA 22202-4302, and to the Office of Management and Budget, Paperwork Reduction Prosect (0704-0188), Washington, DC 20503.

collection of information, including suggestions for Davis Highway, Suite 1204, Arlington, VA 22202-4						
1. AGENCY USE ONLY (Leave blank,	1991 August 16	3. REPORT TYPE AND DA Final	TES COVERED			
4. TITLE AND SUBTITLE		5. 8	UNDING NUMBERS			
Advanced Concepts Theo	ry Annual Report 1990		PE — 62715H			
6. AUTHOR(S)			WU — DNA 880-191			
Radiation Hydrodynamics	s Branch					
7. PERFORMING ORGANIZATION NAI	MF/S) AND ADDRESS(ES)		PERFORMING ORGANIZATION REPORT NUMBER			
Naval Research Laborato	ory					
Code 4720			NRL Memorandum			
Washington, DC 20375-	-5000	ł	Report 6870			
9. SPONSORING/MONITORING AGEN	NCY NAME(S) AND ADDRESS(ES)		SPONSORING/MONITORING AGENCY REPORT NUMBER			
Defense Nuclear Agency						
RAEV						
A lexandria, Virginia 22310						
11. SUPPLEMENTARY NOTES						
12a. DISTRIBUTION / AVAILABILITY S'	TATEMENT	126	. DISTRIBUTION CODE			
		Ì				
Approved for pul	blic release; distribution u	ınlimited.				
13. ABSTRACT (Maximum 200 words))					
This report details th	ne work of the Radiation I	Hydrodynamics Branch	conducted in FY 90			
with respect to several cr.						
optimization of their radia						
z-pinch experiments, the						
models to describe z-pinch implosions, and the analysis of atomic number scaling of z-pinch						
K-shell emission.						
	•					
14. SUBJECT TERMS			15. NUMBER OF PAGES			
Z-pinch physics	Atomic data scaling		152 16. PRICE CODE			
Radiation MHD	Non-LTE dynamics					
17. SECURITY CLASSIFICATION 11. OF REPORT	8. SECURITY CLASSIFICATION OF THIS PAGE	19. SECURITY CLASSIFICATION OF ABSTRACT	ON 20. LIMITATION OF ABSTRACT			

UNCLASSIFIED
NSN 7540-01-280-5500

Standard Form 298 (Rev 2-89) Prescribed by ANSI Std 239-18 298-102

SAR

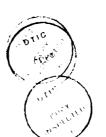
UNCLASSIFIED

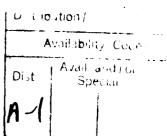
UNCLASSIFIED

Contents

EXECUTIVE PROGRAM SUMMARY

I.	SCALING KILOVOLT X-RAY EMISSION IN Z-PINCHES	1	
II.	ANALYZING EXPERIMENTAL DATA FOR LOAD SHORT CIRCUITS AND ANOMALOUS HEATING	28	
III.	THEORETICAL INVESTIGATION OF THE EFFECTS OF SHORT CIRCUITS AND ANOMALOUS HEATING ON A1 ARRAY YIELDS	60	
IV.	SCALING L-SHELL IONIZATION DYNAMICS	72	
٧.	AVERAGE ATOM MODELING OF L- AND M-SHELL IONIZATION DYNAMICS	78	
VI.	ANOMALOUS PLASMA HEATING AND RUNAWAY ELECTRON PRODUCTION	86	
VII.	2-D FLUID MODELING OF KINETIC ENERGY GENERATION	106	
VIII.	AXIAL FLOW AND STABILITY IN SCREW PINCH PRS LOADS	113	
IX.	ELECTROSTATIC TURBULENCE IN THE Z-PINCH CORONA	122	-





EXECUTIVE PROGRAM SUMMARY

The NRL Plasma Radiation Source (PRS) theory program in FY90 focused on several of the important issues that have arisen in the program over the last several years. They involve the scaling of x-ray emission with atomic number, the analysis of experimental data, the comparison of experimental z-pinch plasmas with their theoretical counterparts, the development of theories and theoretical capabilities to treat the problem of anomalous plasma heating, the development of a 2-D fluid code to calculate anomalous behavior in the acceleration of plasma loads, and the investigation of screw pinch plasmas with which to mitigate 2-D effects in order to achieve stable large aspect ratio implosions. These developments are discussed in sections I - VIII of this final report. All are essential for achieving the necessary understanding to design pulse power machines and PRS loads with desired emission capabilities. Some highpoints of the FY90 NRL program are

- o A thorough analysis of the Physics International aluminum data was made. The analysis clearly showed two aspects of array implosions. The acceleration phase was found to be important for igniting the K-shell on impact. The stagnation phase was found to be important for anomalously heating the plasma and sustaining x-ray emission.
- o A careful reanalysis of NRL Gamble II argon data was made to determine the effects of a short circuit and of a phenomenological anomalous heating on the interpretation of the data. A clear indication that some of the machine energy was short circuited from the load was found.
- o A theoretical parameter study of short circuiting and anomalous heating of aluminum array implosions was made and compared with PI data. Again, evidence was strong for the existence of a short circuit in the PI experiments.
- o A large data base of nickel 1-D implosion calculations was obtained. Preliminary analysis of them confirmed the scaling relations that had been derived from the FY89 aluminum data base. However, the analysis also showed an important influence of L-shell emissions on the K-shell yield scaling and of the severe effect that they have on the MHD.

- o Progress was made in scaling L-shell atomic data and of extending the K-shell ionization scaling behavior into the L-shell. Progress was also made in carrying out average atom calculations that will be useful in doing radiative collapse calculations with high Z elements.
- o Significant steps were taken to calculate the effects of anomalous plasma resistivity on the diffusion of magnetic fields and currents into a z-pinch and to set up some calculations of turbulence driven anomalous heating.
- o A 2-D fluid calculation of the acceleration of a plasma foil was made operational to investigate the effects of plasma instabilities on mass excretion and current penetration during the run-in phase of a z-pinch.
- o The stabilizing influence of axial flows and axial magnetic fields on z-pinch implosions was investigated. Axial fields may be an important design feature of future high current machines.

To summarize the status of the NRL Theory Program, much has been done and much has been learned. However, we need to build on our present capabilities because there is now much more that needs to be done. We now know from past and recent history of the PRS program, that there are many promising PRS design options. All of them will improve on DNA's present simulator capabilities, both in filling the x-ray kilovolt gap and in significantly enhancing the output of existing machine loads. However, we need to learn how to exercise these options intelligently; and thus we need to learn much more about how to utilize them by conducting more experiments on existing machines in order to evolve our understanding of the load plasma dynamics, to firm up how to control it, and then to design these controls.

This evolution is essential since we now know, in theory, how to drive loads to achieve the spectra and yields that are desired in a good simulator. However, we also know that the present experimental behavior of PRS loads departs significantly from the desired behavior that is calculated. We need, therefore, both to redesign our experiments to move them more closely in the direction of the 1-D dynamics that we know it is important for them to achieve

(and there are ways to do this) and to redesign the calculations to better explain why the experiments behave as they do. The NRL Theory Program is oriented toward these future problems. We plan to:

- (1) investigate radiative collapse mechanisms for increasing yields and shortening x-ray pulsetimes by continuing to develop and utilize the capability to implode mixed element loads,
- (2) develop a 2-D radiative hydrodynamics capability to determine to what degree fluid turbulence contributes to anomalous plasma heating and to what degree it reduces plasma compressibility and x-ray yield on axis,
- (3) develop models for plasma micro-instability generated turbulence and runaway electron production to determine to what degree this mechanism can explain anomalous plasma heating and energy coupling to the load,
- (4) apply an existing 2-D fluid capability to determine the degree to which plasma instabilities can degrade our ability to accelerate plasma to high kinetic energies and high x-ray conversion efficiencies,
- (5) continue to develop x-ray diagnostics in the L-shell to carry out unbiased data analyses of time resolved z-pinch x-ray data in order to compare theory with experiment in a variety of complementary and mutually supportive ways,
- (6) investigate the phenomena of short-circuit formation and its impact on PRS load performance.

These are the developments that need to be carried out.

ADVANCED CONCEPTS THEORY ANNUAL REPORT 1990 FINAL REPORT

I. SCALING KILOVOLT X-RAY EMISSION IN Z-PINCHES

INTRODUCTION

In this section, some calculations will be described that indicate clearly some directions that must be taken in pulse power machine and diode design in order to achieve higher kilovolt x-ray yields from PRS loads. Prior to these calculations, the only guidance on x-ray production that came from experiments on existing PRS machines was generally bad. In all cases, it was found that, as one extended the K-shell emission spectrum to higher energies by increasing the atomic number of the PRS load, the yield decreased. In general, therefore, a gap in the x-ray AGT simulation spectrum has existed between 1 to 20 keV in present PRS and bremsstrahlung simulators. The calculations to be described in this section, however, show that, by proper machine design, this gap can be closed, in principle, thereby greatly improving prospects for AGT PRS simulation fidelity. In this section, we will present a brief rationale for and a description of the calculations. A discussion of some important results from this "current-off" theoretical modeling and scaling will then be given, followed by a discussion of some experimental results, which include their analysis and interpretation vis-avis the theoretical calculations. Finally, a number of issues and questions arising from the theoretical/ experimental comparisons, will be discussed and some future program recommendations made.

RATIONALE FOR THE CALCULATIONS

As noted in last year's final report (Figure 6, p. 12), the K-series spectrum in different elements shifts to higher energies quadratically as a function of atomic number Z, reaching energies of ≥ 13 keV for krypton. For nickel, this spectrum is located at ≥ 7.8 keV. The L-shell spectrum also shifts upward with atomic number. For nickel, it overlaps with the aluminum K-shell spectrum, and fills in the region between 0.9 and ≈ 2 keV. The full nickel spectrum is shown in Figure 1. It was calculated, but the inset is a measured spectrum from Double Eagle. Note, the experimental plasma was not hot enough to ignite the L-shell lines at 2 keV. An important question is, why not?

For a plasma to be ionized to any particular ionization stage, it must have a minimum amount of energy per ion, E_{\min} , given by the sum of the plasma thermal kinetic energy and the internal energy of ionization. For ionization to the K-shell, this energy scales roughly as $Z^{3.662}$:

$$E_{min} = \left(E_{thermal}^{+E} internal \right)_{K}$$

= 1.012 $z^{3.662}$ eV/ion

In order to radiate from the K-shell, more than this minimum energy must be delivered to the plasma. One of the simplest ways to impart energy is to accelerate a plasma to a prescribed final velocity. To radiate in the K-shell, the resulting final kinetic-energy-per-ion can be conveniently expressed in multiples of E_{\min} :

$$(K.E.)_{ion} = \frac{1}{2} m_i v_f^2 = \eta E_{min}, \eta > 1.$$

Because of the Z-scaling formula for E_{min} , one concludes that the K-shell energy requirements for nickel are 16.6 times as large as those for aluminum:

$$(E_{\min})_{Ni} / (E_{\min})_{Al} = (28/13)^{3.662} = 16.6$$

Thus to accelerate aluminum to the same final kinetic-energy-per-ion as nickel would require an η value 16.6 times as large as that for nickel:

$$\eta_{Al} = 16.6 \eta_{Ni}$$

Two important questions are, if the ionization energy requirements for K-shell emission in nickel are met, what are the mass and current requirements to make it radiate efficiently in this case? In addition, how well will these requirements conform to the scaling predictions that were made from the aluminum calculations performed last year? Some preliminary answers to these questions are given in this section. Since we do not as yet possess a reliable Z-scaling law for E_{\min} in the L-shell, meaningful comparisons of, for example, aluminum K- to nickel L-shell emission scalings and efficiencies

cannot be made as yet. Work on this problem has been proceeding slowly but steadily, and will be discussed briefly in another section of this report.

During the acceleration phase of a z-pinch implosion, there is little kilovolt x-ray emission. When the on-axis collision occurs, the kinetic energy is thermalized and radiated and kilovolt x-rays are produced. Current in the pinch therefore plays two roles. Initially, during its rise, it supplies the forces to accelerate the plasma. Then, when the pinch stagnates on axis, the current has the potential to significantly cook it by means of a plasma's version of ohmic heating. The calculations described in this section treat only the initial phase of energy input to the plasma. The latter stage still poses significant theoretical challenges, and its evolving treatment will be discussed elsewhere in the report.

Because of the dual role played by the current in a z-pinch implosion, a strong analogy can be made between the PRS simulator program and the ICF laser fusion program. The goal of the ICF program is to generate a large flux of thermonuclear neutrons by means of plasma compression in a 1-d spherical implosion. This implosion is plagued with Rayleigh-Taylor plasma instabilities and with the problem of controlling them. Implosions must be designed to achieve ignition, which generates a self-sustaining thermonuclear burn. The goal of the PRS program, by analogy, is to generate a large flux of kilovolt x-rays by means of plasma compression in a 1-d cylindrical implosion. Plasma interchange and sausage instabilities must be controlled (and have been to some extent) to maintain the symmetry of the implosion. Moreover, as discussed above, the implosions must be designed to ignite whatever ionization shell (K, L, or M) is needed to produce the desired radiation, and the current must be controlled to continue the emission (or burn) process from that shell. The ICF program will succeed only by design, and the long term success of the PRS program will depend on its machine and load designs as well. The major experimental problem in both programs is to establish and maintain the 1-d symmetry of the implosions. Theoretically, the main problem is to thoroughly understand the 1-d physics and to determine the means to achieve and to utilize it experimentally.

CURRENT-OFF THEORETICAL MODELING

Figure 2 shows a typical current trace and kilovolt x-ray pulse recorded at Physics International Inc. during one of their nickel wire shots. The rise in current is approximately linear until just prior to the onset of the x-ray pulse. While the current continues to flow in the real experiment, it is convenient to turn it off abruptly in a theoretical calculation just before the plasma assembly on axis and the commencement of the kilovolt x-ray emission. When this is done theoretically, it is possible to accelerate any array mass to any given kinetic-energy-per-ion conveniently in order to calculate umambiguously how this energy alone is thermalized and converted into x-rays.

The fluid motion calculated when the current is terminated prior to stagnation is shown in Figure 3, which contains the trajectory of each plasma cell in a typical calculation. The implosion begins at t=0 with the array at a radius of 1 cm = 10^4 μ m. The linearly rising current is turned off when the outer cell reaches a radius of 1.4 mm. The plasma continues to move inward inertially. It then stagnates and recoils outward. The total kinetic-energy-per-ion generated by the implosion determines the temperature reached by the plasma (at 89 ns in the example shown), while the mass imploded controls the amount of x-radiation emitted during the collision process. Plasma expansion and cooling then terminate the x-ray emission.

The two basic assumptions of these calculations, are (1) that, during implosion, the jxB force acts on all of the initial load mass and (2) that enough kinetic-energy-per-ion is generated during the implosion to drive the plasma well into the K- or L-shell, i.e. plenty of excess energy is available to be radiated. The mass and peak current in these calculations is adjusted to vary the x-ray yield.

During FY 90, an extensive set of the 1-d radiative MHD calculations just described were carried out and analyzed for nickel. This data base of nickel calculations were similar in every respect to the data base of aluminum

calculations that was obtained and analyzed in FY 89. The coupled nonlinear MHD equations that were solved for aluminum and nickel were state-of-the-art. They contained

- (1) a self-consistent treatment of magnetic field and current diffusion into the plasma.
- (2) a structurally complete, state-of-the-art, atomic model of nickel; for aluminum, significant atomic structure was present in 6 ionization stages.
- (3) an extensive nonlocal description of line photo-couplings within the plasma; for nickel, these consisted of 20 major K-shell and 39 major L-shell lines; but no continuum; for aluminum, these couplings consisted of 12 super-kilovolt lines and 35 sub-kilovolt lines plus an approximate treatment of continuum transport. Levels were collisionally and photo-excited and ionized, and plasma opacity played a significant role in these calculations in controlling plasma conditions.
- (4) a fully consistent coupling of the atomic icnization and radiation transport to the array magneto-fluid dynamics.
- (5) a coupling to circuit equations that allow both current-on and current-off implosion dynamics to be studied. Consequently, future investigations of the importance of radiative collapse to the late time dynamics of the pinch can and will be made.

RESULTS FROM THE CALCULATIONS

A number of significant results emerged from these calculations. One of the most important was obtained from the aluminum calculation, and is displayed in Figure 4. In this figure, the yield of x-rays above a kilovolt is plotted as a function of the imploded aluminum mass for two η values, i.e. for two values of the maximum kinetic-energy-per-ion, K_i , that was generated during the implosion. (Since $(E_{min})_{Al} \approx 12$ keV/ion, in one case $K_i = 3.9$ x $12 \approx 47$ keV/ion; in the other case, $K_i \approx 125$ keV/ion.) As the aluminum mass was increased, the calculated yields changed from an I^4 (or I^4) to an I^4 0 to an I^4 1 (or I^4) to an I^4 3 (or I^4) to an I^4 4 (or I^4) to an I^4 5 (or I^4) to an I^4 6 (or I^4 6) to an I^4 6 (or I^4 7) to an I^4 8 (or I^4 8) to an I^4 8 (or I^4 8) to an I^4 9 (or I^4 9) to an I^4 9 (or I^4 9) to an I^4 9 (or I^4 9) to an I^4 9 (or I^4 9)

turn-off. Moreover, when η was increased, the breakpoint between the I⁴ and the I² scaling shifted to higher mass. Work that was carried out in FY 89 showed how the mass breakpoint would scale with Z for different values of η and this result is shown in Figure 5.

Two questions that we wanted to answer in FY 90, on completing the nickel data base, were (1) how well did the Al breakpoint predictions turn out and (2) how efficient was the nickel radiation conversion process as compared to aluminum? When the I^2 regime was reached in aluminum, a significant fraction f of the generated kinetic energy, $K_c = 1/2 \text{ mv}_f^2$, was converted into x-rays. For example, in the I^2 regime of the $\eta = 3.9$ implosions, which onsets when m > m_{BP} = 23 µg/cm, approximately 34% of K_c was radiated above a kilovolt. According to Figure 5, the breakpoint mass, m_{BP}, for nickel (Z=28) is expected to be = 800 µg/cm when $\eta = 3.9$.

Analysis of the nickel runs that were made in FY 90 showed that this prediction essentially held up, but in a significantly unpredicted way. Figure 6 shows the calculated yields normalized to $K_{\mbox{\scriptsize c}}$ from nickel implosions with $\eta = 3.9$ for x-rays emitted above 900 eV (≈ 1 keV). For nickel, this yield consists of both K- and L-shell x-rays, whereas, for aluminum, only the K-shell was involved. One sees in Figure 6 that the break in I4 scaling occurs at $\approx 100~\mu g/cm$ and not 800 $~\mu g/cm$, as predicted, but this is due to the L-shell emissions. However, only for nickel array masses larger than 800 µg/cm do the K-shell emissions dominate over those from the L-shell. Note that in the I^2 scaling regime, 35% of the nickel kinetic energy was converted into kilovolt x-rays. It appears that f is indeed independent of Z as had been assumed in deriving the scaling prediction. Note also that an h value of 3.9 for nickel corresponds to an energy of 780 keV being imparted to each nickel ion during the implosion. Thus, as should be expected, the K-shell of nickel is ignited for burn only when more ions are imploded and more energy per ion is imparted than is needed for aluminum. A larger current drive is therefore required for nickel than for aluminum. This, in turn, leads to more forceful and violent implosions and more demands on the MHD in order to accurately resolve and predict the dynamical consequences and behavior of these implosions.

The following calculations were made in order to compare the differences in implosions dynamics that result from the large differences in nickel/aluminum ionization and radiation dynamics. Equal masses of aluminum and nickel were taken. Both were accelerated to the same final kinetic-energy-per-ion, and the ensuing plasma dynamics were compared. Some of the results from these calculations are shown in Figures 7-11.

The first 4 figures present the density and temperature spatial profiles that were generated in the two plasmas at the time of peak compression when 80 µg/cm was imploded. Both implosions produced a hot underdense plasma core; however, in nickel the plasma gradients were much more severe than in aluminum. The nickel plasma shell was compressed to a peak density that was an order of magnitude larger than the peak generated in aluminum. This peak in density produced troughs in both the plasma temperature and the x ray emitted power, which is shown in Figure 11. These profiles constitute extreme plasma conditions for the heat and radiation transport calculations and require robust computer algorithms. The smooth and relatively well-behaved curve in Figure 6 offers some assurance that the MHD equations, as programmed, are reasonably well coupled and behaved. The strong gradients that are generated, however, suggest that the effects of electron transport and plasma microinstability generation will be be strong and will need to be addressed and incorporated into the MHD. Another area where better physics is needed is illustrated in Figure 12; where the two regions in Te-Ni space are shaded that contain all of the cell trajectories for two aluminum calculations at 3 and 1000 µg/cm. This figure shows that less massive implosions get hotter and stay less dense than more massive ones. This behavior occurs for two reasons. One, more massive implosions have larger forces acting on the plasma and are pushed to higher densities. Two, more massive implosions have higher radiation losses, stay cooler, and are, therefore, more compressible. Thus, if more massive, higher Z loads are to be properly analyzed, improved equations of state (EOS) should be developed for the MHD.

In all, we compared the total kilovolt yields from three, aluminum and nickel, equal mass implosions. The results are shown in Figure 13. In each case, the ions were accelerated to an energy of 250 keV/ion. At low masses, nickel performed better than aluminum because the aluminum was overheated. At 400 µg/cm, aluminum began to outperform nickel in total yield. The middle

row of the table indicates an important difference between the emitted spectra, however. At 400 μ g/cm almost half of the nickel output occurs in the K-series lines at \geq 7.8 keV.

THEORY COMPARISONS WITH EXPERIMENT

Theoretical efforts over the past several years in the Advanced Concepts Program have led to the development of three methods and procedures for analyzing experimental z-pinch data. One of these methods will be discussed in the following section. It involves comparing measured voltage and current traces and measured x-ray yields to these same quantities as they are obtained from a calculation of the load dynamics that is based on the measured open circuit voltage. By making this comparison, one can determine whether or not the energy flowing through the diode reaches the load or is short circuited from it. The application of the other two methods of data analysis will be The second method derives from the calculations discussed in this section. described above. In this case, the experimental mass that was imploded and the implosion kinetic energy are inferred from measurements of the implosion time and the load inductance change respectively. One then compares the calculated yield for these parameters with the measured yield in order to carry out an energy budget analysis. Finally, the third method of analysis was developed two years ago (see FY 88 final report). It was applied first to the analysis of a copper wire experiment and then to the analysis of three titanium wire experiments. It was extended in FY 90 to be applied to the aluminum wire experiments that had been conducted at Physics International in the fall of 1989. In this case, the x-ray data is analyzed exclusively to infer a self-consistent set of plasma temperatures, densities, and emission masses using simultaneously: x-ray yield, pulsewidth, pinhole picture, and spectral data, either time resolved or time integrated.

Because experiments cannot be carried out on a given machine in precisely the way that current-off calculations were carried out, the next best approach was adopted at PI in their series of aluminum wire shots. In these experiments, the time of implosion was chosen to coincide roughly with the time of peak current by the proper choice of mr_0^2 , where m was the mass per length of a 12 wire array and r_0 was the initial radius of the array. The mass was varied keeping mr_0^2 = constant. Thus, K_c , and not K_i , was held

constant in these experiments; that is, η increased and m decreased as r_0 was increased.

Results from the experimental/theoretical comparison are shown in Figure 14. The dots represent the experimentally measured kilovolt yields, the crosses are direct theoretical current-off calculations of the implosions, which were started at the initial radii of the corresponding experiments, and the line was obtained from the aluminum scaling laws, which were derived for the case $r_0 = 1$ cm. The shaded region represents implosions for which η was less than one and, therefore, for which the current-off 1-d calculations did not apply. The experiments appeared to know this fact since in the two experiments that were conducted in this region, the K-shell x-rays were observed to emanate from hot spots formed by plasma instabilities. Most importantly, the observed yields, which were produced over the duration of the sustained current pulse, were larger than the calculated current-off yields except for the largest diameter array. Large diameter implosions, however, are well known to cause experimental problems since it is difficult to maintain the symmetry of implosion with a small number of wires in this case. These results provide strong evidence that a significant (quantifiable) amount of anomalous heating is taking place that is not yet understood theoretically.

Time resolved x-ray data were also obtained in these experiments. In one particular well diagnosed shot, if one assumed that all of the aluminum mass were radiating, the pinhole pictures suggested that the density of the emission region was declining. The time resolved spectra suggested the plasma was heating up and burning through the K-shell; however, x-ray diode data showed that the power radiated continued to rise - a contradiction. The data analysis, on the other hand, showed that the mass in the emission region was rising along with the density and that the temperature was tending to hold steady (or rise slightly). These results are summarized in Figure 15. Note that the mass in the emission region rises until 86% of the initial mass is radiating. By contrast, when a titanium wire array shot was analyzed previously, it was found that only 9% of the original wire mass was involved in the K-shell emission.

SUMMARY AND CONCLUSIONS

Because of the size, complexity, and cost of high energy, pulse power machines, there is a tendency to regard their design and construction as the technology challenge, while, in fact, there are challenges equally as great in the areas of load design and in the problem of focusing the machine energy and in delivering it to the load as needed. When interpreting experimental results we need to known whether the machine power has reached the load or whether it has been short-circuited, whether or not it breaks down the load uniformly, and whether or not it can be made to flow through the load symmetrically to produce symmetrical implosions.

With regard to load design issues, the aluminum experiments produced the following findings. In the PI experiments, the plasmas were much less compressed and they emitted over a much longer time than in the current-off more current confinement than inertial calculations. Hence, there was Nevertheless, the experimental yields were found to be significantly larger than the theoretical yields calculated on the basis of kinetic energy conversion alone. This finding provides strong, direct evidence of the existence of a "burn" phase to the x-ray production that is caused by anomalous current heating. More importantly, the experimental yield dropped precipitously and hot-spots became the source of the radiation when η became less than 1. This finding provides strong evidence for the "ignition" concept, i.e. for the idea that the thermalization of kinetic energy is an important initiating process that drives the plasma into the correct ionization stages for subsequent efficient x-ray production.

One of the most important conclusions drawn from the theoretical/experimental comparisons was that the experiments do not always produce the conditions assumed in the theoretical calculations (although if carefully designed they may) and, therefore, they do not always give the predicted consequences. We have also learned from these comparisons the importance of complete data sets (time resolved if at all possible) in order that a consistent analysis of the experimental plasma dynamics be made and a better understanding of them be developed. In particular, it is important that the following questions be addressed in experiments:

1. Does all of the wire mass implode? It does in the calculations. Under the right conditions, it will in the experiments.

- 2. What is the η value achieved in experiments? Is it larger or smaller than 1? It makes no sense to analyze z-pinch experiments for their K-shell emissions using 1-d MHD models if η <1.
- 3. Is anomalous heating and plasma turbulence occurring? It is important we learn where, when, and how much of it occurs experimentally and how it scales with Z since theoretical guidance on this problem is under development and needs experimental support.
- 4. How strong are the effects of radiative collapse when anomalous heating and turbulence is present? We need experiments with wires that are alloyed with heavier Z elements.
- 5. How much mass is blown inward when the wires explode? Such mass can soften the pinch and reduce radiation efficiencies.
- 6. Can more methods be found to control instability growth and make the pinches more symmetrical? 1-d symmetry is essential for ICF and it is essential for x-ray simulation fidelity.
- 7. Can stable, large aspect ratio implosions be achieved for moderate 2 elements? The use of axial magnetic fields may be one answer, using more wires for greater symmetry may be another. Large aspect ratio implosions make it easier on machine design to obtain the high kinetic-energies-per-ion that are needed to ignite the K-shells of these elements.
- 8. Are plasma instabilities limiting the compression and stretching out the x-ray pulse or are they simply disguising, as has happened in the past, the presence of other physical phenomena that are causing these effects?

In summary, since machines must be designed to match the K-shell energy requirements of the load, it is important that reliable theoretical calculations of these requirements be made. Moreover, to design efficient high yield experiments with highly inelastic collisions, it is necessary to

implode and compress large masses. Calculations must be carefully constructed to guide load designs to achieve these conditions. The pulse power drivers are too large and the loads too small to be effectively designed without a good theoretical understanding of electrical power flow and power conversion phenomena.

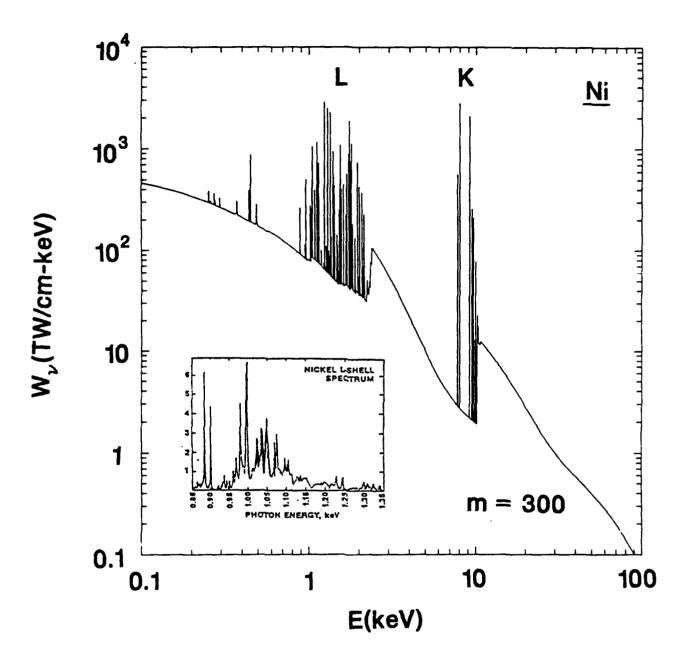


Figure 1

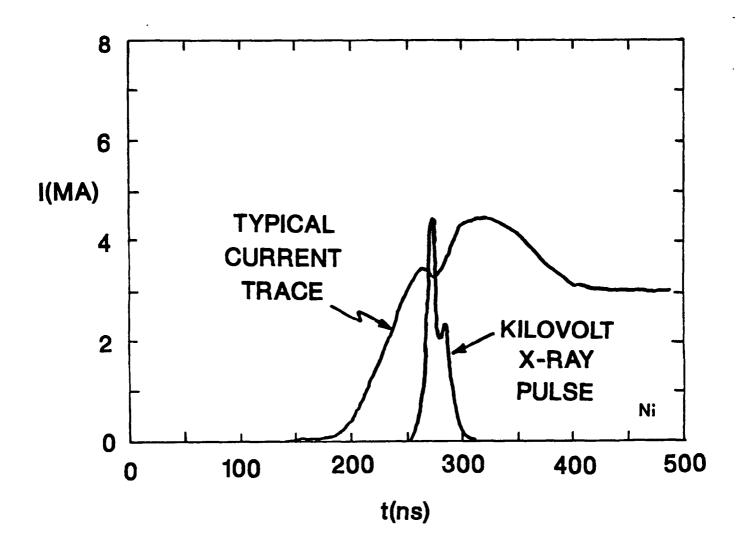


Figure 2

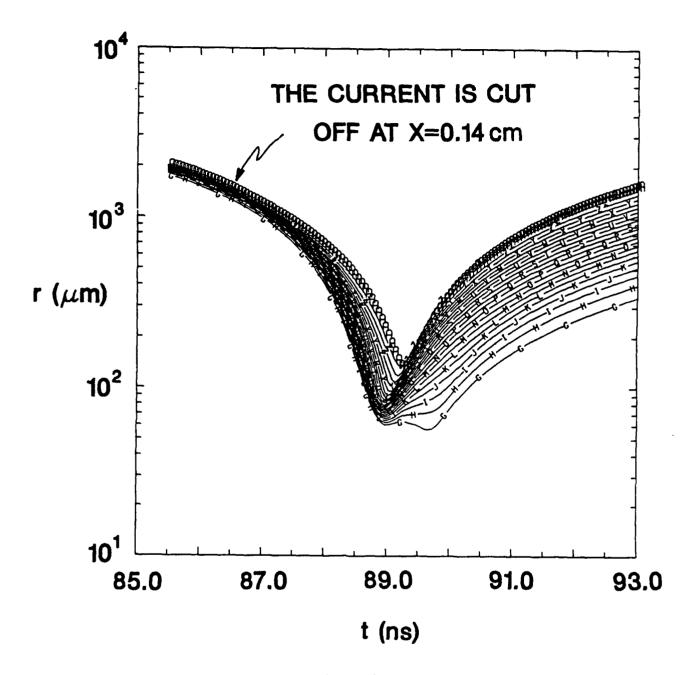


Figure 3

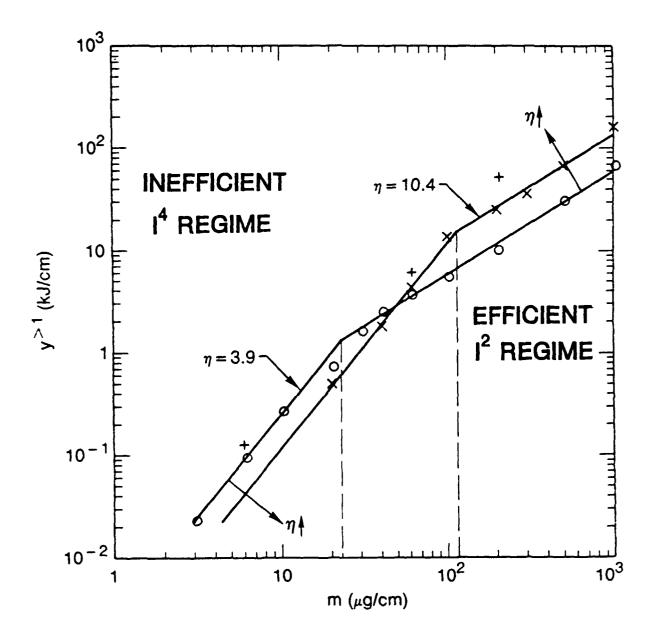


Figure 4

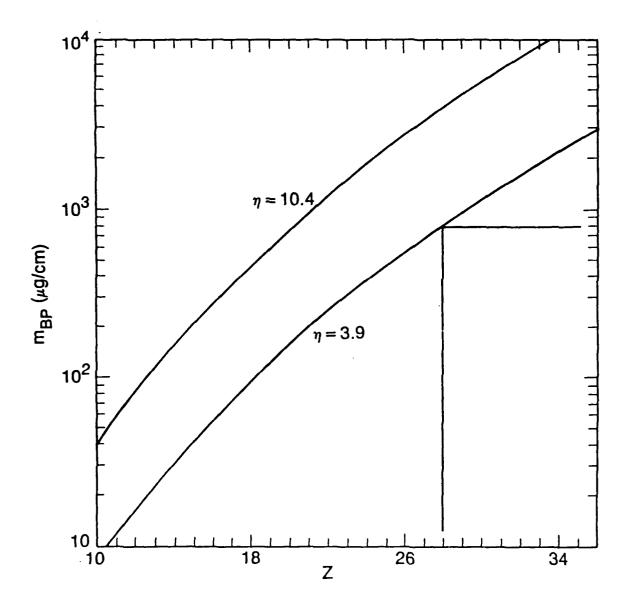
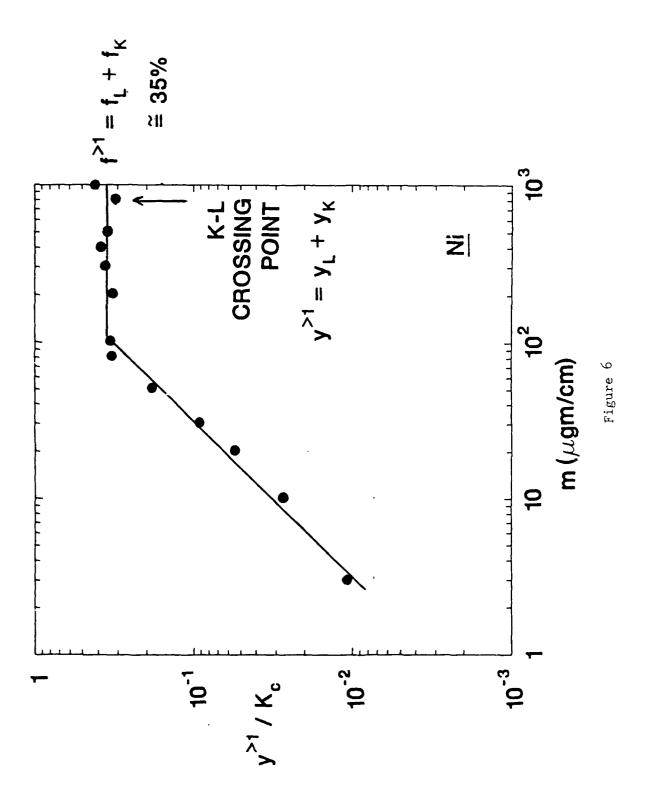


Figure 5



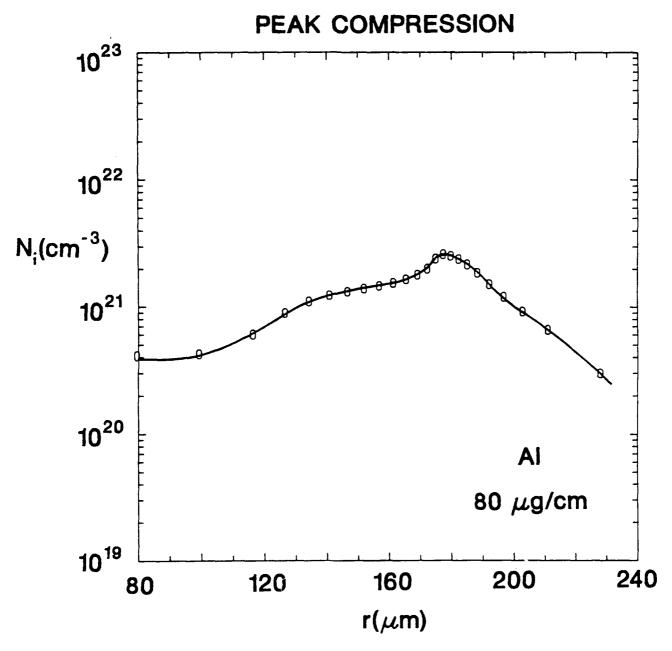


Figure 7

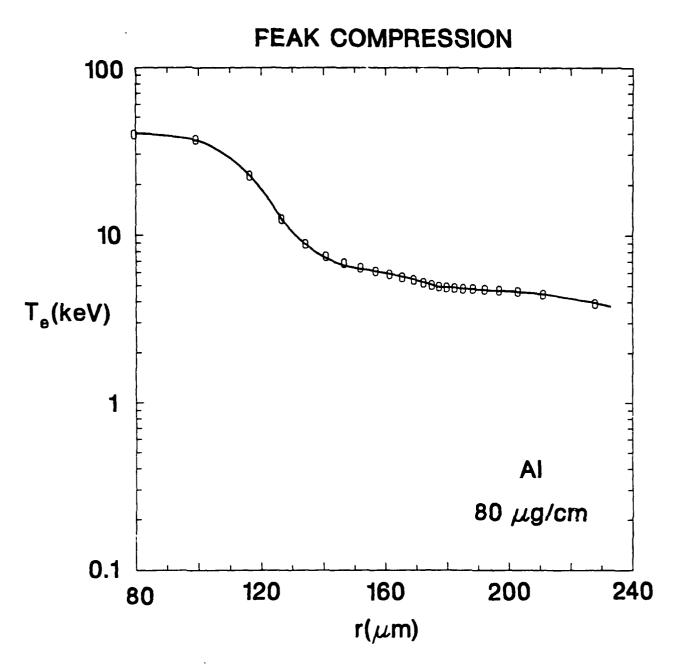


Figure 8

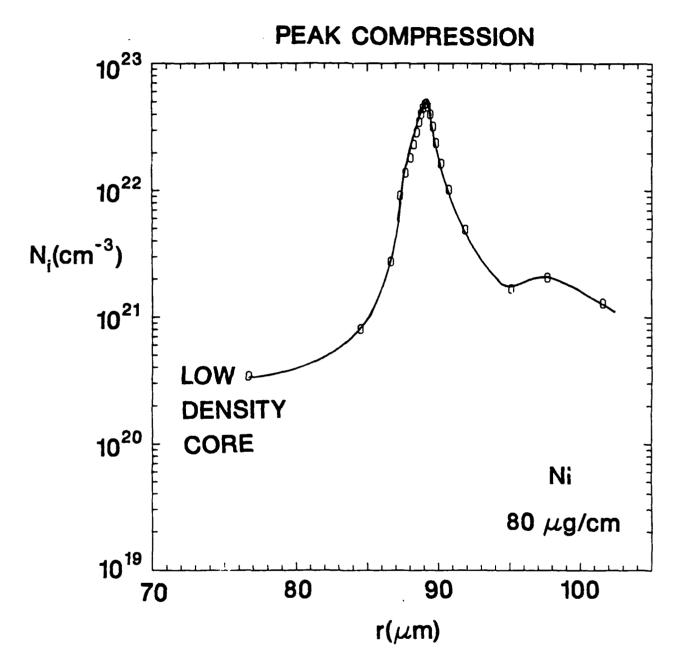


Figure 9

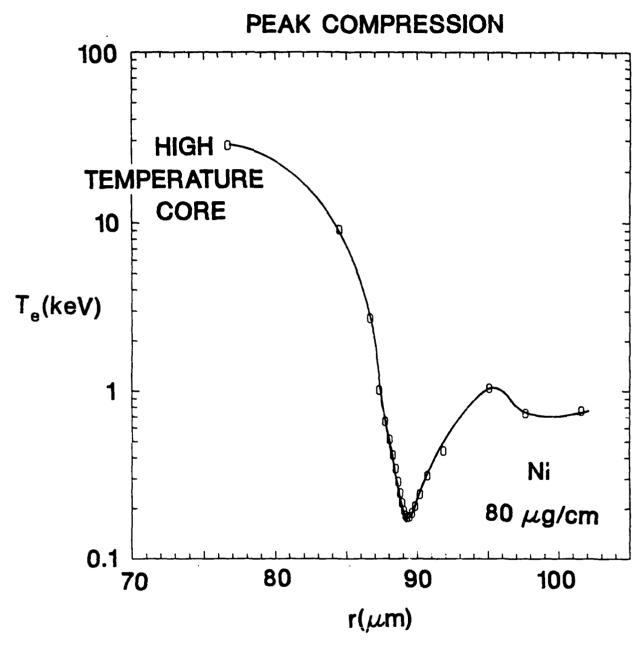


Figure 10

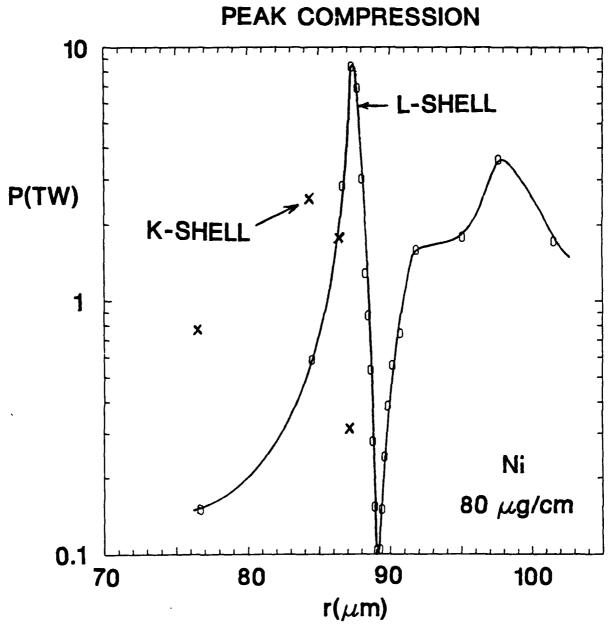


Figure 11

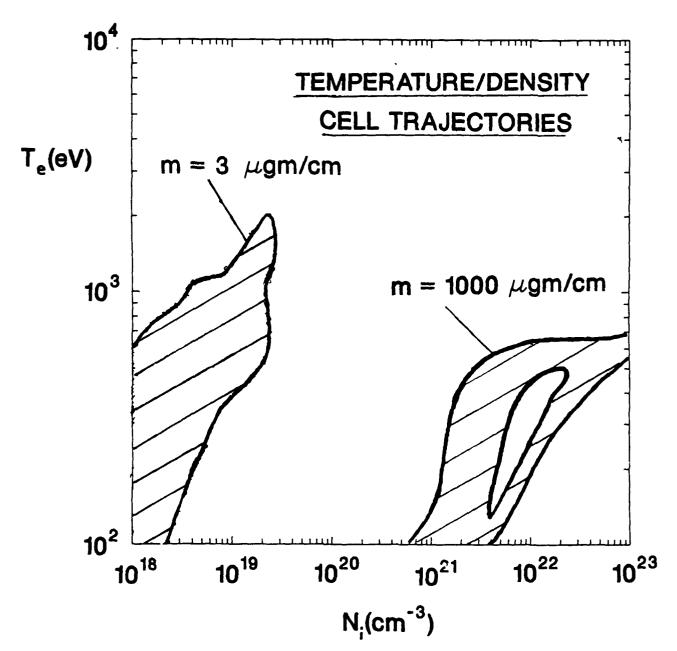


Figure 12

YIELD^{>1} (kJ/cm)

80 400 μg/cm	13.1 79.1	(1.9) _K (38.6) _K	5.4 90.3
20 µg/cm	2.0	(0.26) _K	0.4
ELEMENT		2	¥

250 keV/lon

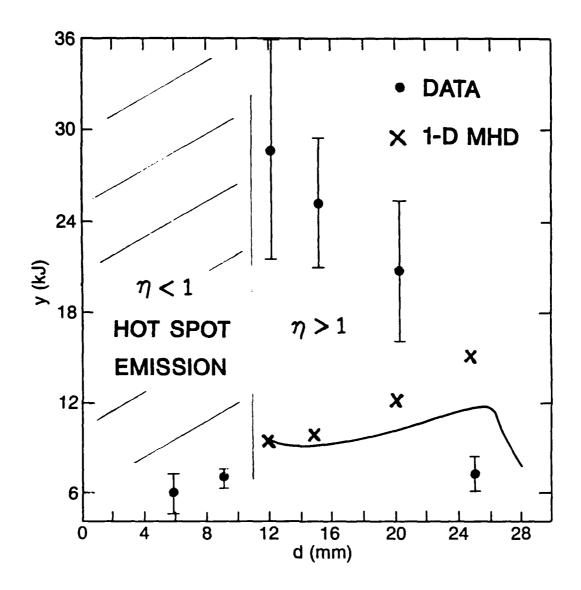


Figure 14

DATA ANALYSIS

TIME RANGE (ns)	T _e (keV)	N _i (cm ⁻³)	m _K (μg/cm)
95-105	1.1	4.5×10 ¹⁸	21
105-115	1.0	5.8×10 ¹⁸	60
115-125	1.2	6.6×10 ¹⁸	90

 $m_{initial} = 105 \ \mu g/cm$

Figure 15

II. ANALYZING EXPERIMENTAL DATA FOR LOAD SHORT CIRCUITS AND ANOMALOUS HEATING

I. INTRODUCTION

This work compares 1-D theoretical calculations with experimental results for a series of argon gas puff experiments performed on the NRL Gamble II generator. The NRL experimental arrangement and the 1-D theoretical model are discussed and then comparisons are made for: (1) K-shell and L-shell x-ray emission and (2) energy coupling between the machine and load. The results of this work show there may be better agreement between theory and experiment if additional physical mechanisms affecting the implosion dynamics are included (phenomenalogically) in the 1-D theory. The consequences of adding two phenomena, namely, anomalous resistivity and a short circuit are discussed. Similar comparisons between theory and experiment are also made for an aluminum wire array implosion that was performed on the PI Double Eagle machine.

We do not expect the results of the simulations to agree with experiment for all cases. There is no calculation (O-D, 1-D, 2-D, or 3-D) that claims to accurately solve the plasma dynamics of a pinch at small radii, especially in the presence of instabilities and inhomogeneities. Rather, the intent of this work is to compare two key areas, radiative emission and energy coupling, where theory and experimental measurements overlap. The general goal being to further our understanding of z-pinches so they can be designed and controlled to fit DNA's needs. This work is a refinement and extension of work presented at the DNA Nvoo meeting, 5-6 April, 1988.

II. NRL EXPERIMENTAL ARRANGEMENT

The experimental arrangement is shown in Fig. 1. A hollow cylindrical argon puff is injected across the anode-cathode gap using a high mach number nozzle. The nozzle is mounted on the center conductor. The anode is a wire mesh that provides a current path to ground through the current-return rods and allows gas to flow away from the diode region. The voltage is measured in the water just before the insulator interface. Current in the diode is measured with a Rogowski monitor located where the current I is shown. The (jxB) force

from this current drives the plasma radially inward until it implodes on axis. X-ray diagnostics view this implosion through gaps in the current-return posts as illustrated in the end view. A schematic diagram of the nozzle region is shown in Fig. 2. The return current rods are 4 cm in length and they are at a radius of 3.5 cm from the axis of the diode. The nozzle has an outside radius of 1.9 cm and an inner radius of .6 cm.

A complete summary of the experimental setup and results can be found in references 1 and 2.

III. THEORETICAL MODEL

The 1-D model numerically solves the continuity, momentum and energy equations in a Lagrangian reference frame with cylindrical geometry (30 radial zones) and axial symmetry. It solves for the ion and electron temperatures. The current density profile is calculated assuming magnetic diffusion is a valid approximation. Once the current distribution is known, the local values for (jxB) force and ohmic heating can be calculated.

The ionization and radiation dynamics is treated self-consistently using a time-dependent collisional radiative (CR) model. This model is a modified version of the collisional radiative equilibrium (CRE) models developed by the Plasma Radiation Branch at NRL³. The atomic states that provide the basis for the argon atomic physics model are all 19 ground states and 77 selected excited levels. Note, this is a significant enhancement of excited level structure over the earlier model employed for the work presented at the Nvoo meeting, which had only 44 excited states. Radiation is transported using a probabilistic scheme 4,5 which forms angle and frequency averaged escape probabilities for each line emission and recombination process.

Fig. 3 displays an estimate for the initial radial ion density distribution of the argon gas puffs. It is based on the radial pressure profiles that were measured at various axial distances from the cathode. The same distribution is used in the theoretical calculations. Units of the ion density are dimensionless so as to show only the relative value of the radial

dependence. Note, the density in the wings of this distribution corresponds to a background gas that is artificially added in order to insure numerical stability. Its presence does not significantly affect the numerical results.

The current I is calculated by solving a circuit equation that is appropriate for Gamble II, see Fig. 4. The impedance of the plasma load is assumed to be in series with the machine inductance and resistance. Once the current is obtained, it provides a boundary condition for the magnetic field B at the outer edge of the gas puff. The machine inductance L_0 is 58 nh and the resistance R_0 is 2 ohms. The circuit is driven by the Gamble II open circuit voltage profile $V_{\rm oc}$. The voltage that is measured in the experiment is $V_{\rm meas}$. L(t) and R(t) are the time dependent inductance and resistance of the plasma load.

The open circuit voltage profile that drives the above circuit is shown along with a calculated short circuit current profile in Fig. 5. This current profile is obtained by placing the plasma load with a short circuit. The purpose of displaying it is to show the general shape of a typical Gamble II current profile.

IV. EXPERIMENTAL AND THEORETICAL RESULTS

Before describing the details of comparisons between experiment and theory, the theoretical results need to be normalized to the experimental results. This is because loads that are used in the experiment are measured in terms of plenum pressure, whereas in the calculation the amount of plasma present in the z-pinch is needed in terms of mass per unit length. The normalization is accomplished by examining implosion time, which is defined as the time the peak in L-shell x-ray emission occurs. Plotting this time for the experiment and the theoretical calculation, see Fig. 6, reveals a two to one correspondence between plenum pressure (psi A) and mass per unit length (µg/cm) approximates this normalization. This result is in accordance with earlier work done at NRL⁶.

A. Comparison of L and K-shell emissions (NRL experiments)

The experiments only measured those L-shell x-rays with energies between 250 to 460 eV (Ti filter K-edge). We find that theoretical calculations for x-ray emission in this same energy range are in good agreement with the experiment as is clearly illustrated in Fig. 7. This is in contrast to the Nvoo results in which there was not enough excited state structure in the model to adequately characterize the L-shell emission.

A comparison of K-shell emission, Fig. 8, shows that the theoretical implosions consistently produced more K-shell radiation than the experiment for low mass loadings, 8 times as much for the 17.5 μ g/cm load. However, the 1-D calculations and experimental measurements agree for large mass loadings. The overall shape of the emission curves are the same and there is agreement that maximum K-shell emission occurs for a loading of ~ 18 μ g/cm. The η values displayed at each data point in Fig. 8 are an indicator as to whether the plasma has the necessary minimum energy E_{\min} needed to ionize to the K-shell. Where,

$$E_{\min} = (E_{\text{thermal}} + E_{\text{internal}})_{k}$$
$$= 1.012 \text{ z}^{3.662} \text{ eV/ion}.$$

If the energy is supplied by thermalization of kinetic energy, then the kinetic-energy-per-ion can be written as

$$(K.E)_{ion} = 1/2 m_i v_f^2 = \eta E_{min}$$

where m_i is the ion mass and v_f is the maximum velocity that occurs just before the plasma stagnates on axis. In the 1-D simulations, the magnetic field does a significant amount of work on the plasma during the stagnation phase of the implosion, which is due to the r^{-1} nature of the magnetic field at the boundary of the pinch. In order to more accurately account for the total (jxB) work done on the plasma we defined η^* from the following relation,

$$(jxB)_{\text{work per ion}} = \eta^* E_{\min}$$

Assuming it requires at least twice E_{\min} of thermalized energy per ion to enable the plasma to significantly radiate in the K-shell, the scaling work of Whitney and Thornhill^{7,8} predicts a minimum mass of 27 µg/cm of argon is needed in order to be in an I^2 scaling regime of K-shell emission with current. Because the mass loads in this study do not meet this requirement, even with η^* energy coupling, it appears theoretically that the experiments were performed in the very unpredictable I^4 scaling regime. Therefore, it is not surprising that there is a large difference between experiment and theory in regards to K-shell yields. In order to obtain a significant (per unit mass) enhancement in K-shell emission more mass needs to be imploded at higher velocities than is present in these experiments.

B. Comparison of energy coupling (NRL experiments)

The three curves shown in Fig. 9 pertain to the machine energy that is coupled to the plasma. Experimentally the amount of coupled energy, curve 1, is obtained by integrating the product of the current (I_{meas}) and voltage (V_{meas}), obtained from current and voltage traces, from time t = 0 to time $t = \tau_{end}$, where $I(\tau_{end}) = I(0) = 0$. If all the current passes through the load, this value should physically represent the sum of the kinetic and internal energies at time $t = \tau_{end}$ plus the total energy radiated from the plasma up until $t = \tau_{end}$. The second curve displays the theoretical calculation of this energy, again assuming that all the current passes through the load, up until the time $t = \tau_{end}$. The third curve shows theoretical maximum values for the sum of internal, kinetic and radiated energies at any time during the plasma evolution. In all cases, the maximum values occurred at the time of peak implosion t = τ_{imp} . The value for coupled energy is always lower at the time $t = \tau_{end}$ because the 1-D plasma does work against the magnetic field during expansion after the bounce. Some of the more massive loads implode late enough in time that there is not much magnetic field present at implosion. Therefore, their coupled energy is about the same at the end of the current pulse as it is at peak implosion. This is also partially due to the fact that the more massive loads tend to be good radiators. Thus, they radiate a significant amount of their energy away upon stagnation and there is not much available energy to do work against the magnetic field after the bounce.

A comparison between the first two curves shows that the experiment and theory are in agreement for the 30 µg/cm loading, but, for smaller mass loadings the agreement is poor. One can argue that instabilities and inhomogeneities are responsible for the large difference between theory and experiment in regards to the amount of energy coupled to the plasma load. If we included these mechanisms in the the theory, then curve 2 in Fig. 9 should begin to look like curve 3 because the plasma would no longer behave as a perfect piston, i.e. the radially directed kinetic energy would no longer be efficiently converted into thermal energy. This in turn would reduce the amount of work the plasma is capable of doing against the magnetic field after implosion. Instead, this work would remain coupled to the plasma as either internal energy or kinetic energy, not necessarily directed in the radial direction, or else it could be radiated away.

The 1-D calculation of energy coupling is optimistic in the sense that theoretical radial compressions are greater than observed in the experiments. From simple 0-dimensional analysis 9 , one can show that the maximum amount of energy that can be coupled to the load, in the absence of significant ohmic heating (which is the case in the 1-D calculations), is less than 1/2 2 L I 2 , where 4 L is the change in the inductance and I 4 is the peak current. The change in inductance for a 4 cm length plasma is 8 x 4 10 9 x 4 1n(4 1 8 1) henrys, where 4 1 and 4 2 are the initial and final radii of the pinch. Substituting the measured value for peak current, 4 1 mega-amperes, into the above expression for inductive energy reveals that the energy coupling is 11 kJ for a typical radial compression (experimental estimate) of 4 1 8 1 mega-amperes in order to couple 23 kJ of energy into the load as observed for the 18 ug/cm load requires a radial compression of 100 (ion densities 8 10 mega assuming that the plasma remains axially uniform). It is doubtful that such high densities are achieved, except possibly in a few isolated spots. The largest density achieved in the 1-D theoretical calculations was of the order 10 9 cm $^{-3}$ 2.

Unless one can show that the presence of inhomogeneities and instabilities can somehow further enhance the energy coupling to the load it is very difficult to explain the difference between curves 1 and 3 of Fig. 9, which represents the 1-D theoretical energy coupling, or the difference between measured (23 kJ) and estimates of experimental coupling (11 kJ). Some possible explanations for this difference in energy coupling include:

- 1) Instabilities and inhomogeneities, such as flaring, could create larger inductive coupling. For example, if an m=0 instability is present, there are regions of necked down plasma where the ratio of R_i/R_f is much greater than 10. This does not necessarily imply that the density of these regions would have to be large because some of the real 3-d plasma could have squirted axially out of the region.
- 2) If plasma instabilities and/or inhomogeneities do lead to regions of necked down plasma, then there could be significant energy coupling to the load via ohmic heating. This is due to the r^{-2} nature of the resistive electric field, given by I x η / (πr^2), where η is the (Spitzer) resistivity.
- 3) Again, if the presence of instabilities and/or inhomogeneities leads to constrictions of the plasma, then the r^{-1} nature of the inductive electric field and the r^{-2} nature of the resistive electric field could give rise to a total electric field large enough to cause the runaway of electrons.

Hares, Marrs and Fortner 10 discussed the later two explanations as possible heating mechanisms of hot spots in z-pinches. All of these explanations, with the exception of runaway electrons, can be considered anomalous heating. In the next section we treat anomalous heating as an anomalous resistance, which could be present in either a stable or unstable plasma, and discuss how it theoretically changes K-shell emission, L-shell emission, and energy coupling of the load.

C. Anomalous Resistance

Anomalous resistivity was modeled simply by multiplying Spitzer's cross field resistivity 11 by a factor of 200 (β =200) throughout the entire simulation. Fig. 10 displays the comparison of L-shell emission, Fig. 11 the comparison of K-shell emission, and Fig. 12 shows the comparison of energy coupling to the load. The agreement between theory and experiment for L-shell emission (250 - 460 eV) is very good and is about the same as the agreement achieved in the case with no anomalous resistance. The comparison of K-shell emission reveals that

the anomalous resistivity results are in better agreement with experiment then the original Spitzer (β =1) calculations. However, the energy coupling is less in agreement with experiment than the (β =1) results. In particular, the peak coupling curve (3) shown in Fig. 12 is significantly lower than the same curve for the (β =1) results illustrated in Fig. 9. The reason for this difference is the increase in anomalous resistance produced more ohmic heating and magnetic field penetration during the run-down phase of the implosion. Both of these effects make it more difficult to compress the plasma at stagnation. Thus, reducing the (jxB) work and K-shell yield.

Because there is less peak energy coupled to the plasma by this model than either experiment or the $(\beta=1)$ model, it appears that if anomalous heating behavior is present then it occurs just before or during the stagnation of the plasma. As suggested earlier it may result from isolated necked down regions of plasma where the r^{-2} nature of the electric field can give rise to significant ohmic energy coupling.

D. Short Circuit

Another mechanism that could enhance energy coupling is short circuiting of the diode. 12 If the diode is shorted during stagnation then the magnetic field energy in the diode becomes trapped and is eventually dissipated in the diode. This mechanism is modeled schematically in Fig. 13, for which the short is treated as a resistance, having the form $R_{shcrt} = 10^7 \times exp(-1/(r_o - .1))$ ohms, R_{short} is very large until the outer radius in parallel with the load. approaches .1 cm, thereafter, as the outer radius continues to move closer to the axis, $R_{\mbox{\scriptsize short}}$ rapidly becomes a small resistance and is effectively a short. Fig. 14 compares L-shell emission (250 - 460 eV) of the shorted load with experimental results. Again, the experimental and theoretical results are in reasonable agreement. A comparison of K-shell emission, Fig. 15, shows there is considerably more K-shell emission produced when a short is present in the circuit. The reason is the trapped magnetic field energy causes the plasma to ring, i.e. it repeatedly expands from the axis and stagnates on axis until all of the trapped magnetic field energy is radiatively dissipated. The whole system behaves like a damped oscillator in which the plasma gives energy to the magnetic field upon expansion until the magnetic field strength overcomes the

plasma pressure and recompresses the plasma. Every time the plasma stagnates on axis a pulse of K-shell radiation is emitted. The Energy coupling comparison shown in Fig. 16 is very interesting in that we find excellent agreement between theory and experiment, with the exception of the lowest mass loading, which inherently has the most experimental error.

E. Comparison with Double Eagle Results

Now we compare theory with experiment for an implosion of an aluminum wire array plasma. It is a 105 µg/cm load that consists of 12 aluminum wires that are configured in a 2 cm diameter array. The return cage of the machine is 2.6 cm in diameter. The implosion is modeled using the Double Eagle circuit diagram displayed in Fig. 17. The open circuit voltage profile that drives this circuit is shown in Fig. 18. This figure also illustrates the short circuit current profile.

The experimental results are summarized in Fig. 19. 12 We see that the total x-ray yield was 60 kJ of which 18 kJ was emitted from the K-shell. The K-shell power as a function of time is graphed in this figure as well as estimates, based on x-ray pinhole data, of the radius at which the plasma is emitting Kshell and L-shell emission. The change in inductance of the experimental pinch is estimated to be 6.2 nh and the peak current was ~ 3.5 MA. Substituting these numbers into the formula for inductive energy coupling $E = .5 \times \Delta L I^2$, gives about 38 kJ. Since there is more energy than this radiated from the plasma ~ 60 kJ, it appears that there is some anomalous heating taking place during and after the stagnation and/or the diode has shorted. Theoretical results are shown in Fig. 20 for K-shell powers as a function of time for simulations with $(\beta=100)$ and without $(\beta=1)$ anomalous resistivity. The theoretical plasmas where such prolific radiators that eventually they radiatively collapsed. For this reason, the total and K-shell yields given in Fig. 20 are valid for a time of ~ 114 ns. There is little K-shell radiation emitted after this time but there is a significant amount of softer x-ray emission. Comparison with experiment reveals that K-shell yields are about the same, which is surprising since it appears that the theoretical plasma conditions are different than exists in the experiment. Specifically, the theoretical outer plasma radius is orders of magnitude smaller than the experimental radius. In addition, the time over

which K-shell radiation is emitted is much shorter in the simulation, i.e. K-shell radiation was observed over 35 ns time scales whereas in the simulations the time was about 1 ns.

V. DISCUSSION

NRL Argon Gas Puff Experiments

Theoretical calculations revealed that there was insufficient mass imploding at high velocity to efficiently produce argon K-shell emission, and this was corroborated by the experimental measurements. Comparisons of predicted versus measured energy coupling showed evidence that our understanding of this area of z-pinch phenomena is incomplete and deserves further investigation. This evidence applies to mass loads that stagnate on axis near the time of peak current, it includes: (1) experimental energy coupling is significantly larger than theory predicts, (2) inductive energy coupling (.5 Δ L I²), based on estimates of the final experimental compression radii, are less than 1-D theory predictions, and (3) this experimental inductive energy coupling only accounts for about half of the total energy believed to be coupled to the load.

1-D theory predicts that most energy coupling to the load is inductive. However, the above evidence supports the conclusion that another mechanism is responsible for a significant portion of the energetics. We modeled phenomenologically a few possible mechanisms with inconclusive but informative results. For example, the litany of possible anomalous heating mechanisms that might be due to unstable plasma behavior was treated as an anomalous This produced anomalous heating and enhanced magnetic field penetration that limited the compression radius and 1-D inductive portion of the overall energy coupling, which gave better experimental agreement in these areas. However, the increase in ohmic heating was insufficient to offset the decrease in inductive energy coupling and therefore the disagreement between total energy coupling was even more pronounced than the case without anomalous resistivity. The second phenomenological mechanism modeled entailed including a The purpose of the short is to trap short in the driving circuit of the diode. all of the magnetic field energy present at stagnation in the diode, where the

energy will be forced to dissipate in the plasma. Excellent agreement with experimental energy coupling is achieved, however in this case, the dynamics of the implosion is not changed significantly from the original 1-D calculation. Again, experimental estimates show larger final compression radii and less inductive energy coupling than 1-D theory predicts.

Double Eagle Aluminum Wire Array Experiments

There were several comparisons in agreement with the Gamble II results: (1) simple estimates of the experimental inductive energy coupling reveal that it is not sufficient to account for all of the overall energy coupling; actually, it could not even account for all of the radiated energy, and (2) the 1-D theoretical inductive energy coupling was significantly larger than the experimental observation, which is a reflection of the fact that radiative collapse was observed in the 1-D simulations.

The XRDs and time resolved x-ray pinhole diagnostics that were fielded in these experiments allow us to make the observation that K-shell radiation was emitted over a much longer time scale ~ 35 ns as opposed to the 1 \sim ns theoretical time scales.

All of the above comparisons indicate that there is substantially different physics taking place in these experiments than is being modeled in the 1-D theory. We are currently investigating a number of possible resolutions to these differences, which were outlined in the first section of this report. If through well diagnosed experiments and thoughtful theory we can begin to understand some of the complexities of a z-pinch implosion, we may be able to control the z-pinch in order to take advantage of additional energy coupling and 1-D behavior to give optimal x-ray fluence.

References

- 1) F.C. Young, S.J. Stephanakis, and V.E. Scherrer, Rev. Sci. Instrum. 57, 8, August (1986).
- P.G. Burkhalter, G. Mehlman, F.C. Young, S.J. Stephanakis,
 V.E. Scherrer, and D.A. Newman, Journal De Physique 47 Oct. (1986).
- 3) See references contained in D. Duston, R.W. Clark, J. Davis, and J.P. Apruzese, Phys. Rev. A 27, 1441 (1983).
- 4) J.P Apruzese, J. Davis, D. Duston, and R.W. Clark, Phys. Rev. A 29, 246 (1984).
- 5) J.P Apruzese, J. Davis, D. Duston, and K.G. Whitney, J. Quant. Spectrosc. Radiat. Transfer 23, 479 (1980).
- 6) F.C. Young, private communication NRL.
- 7) K.G. Whitney, J.W. Thornhill, J.P. Apruzese, and J. Davis, J. Appl. Phys. 67, 1725 (1990).
- 8) J.W. Thornhill, K.G. Whitney, and J. Davis, J. Quant. Spectrosc. Radiat. Transfer 44, 251 (1990).
- 9) D. Mosher, private communication NRL.
- 10) J.D. Hares, R.E. Marrs, and R.J. Fortner, J. Phys. D. Appl. Phys., 18, 627 (1985).
- 11) D. Book, NRL Plasma Formulary, NRL Publication 0084-4040 (1986).
- 12) Christopher Deeney, private communication, Physics International Lab.

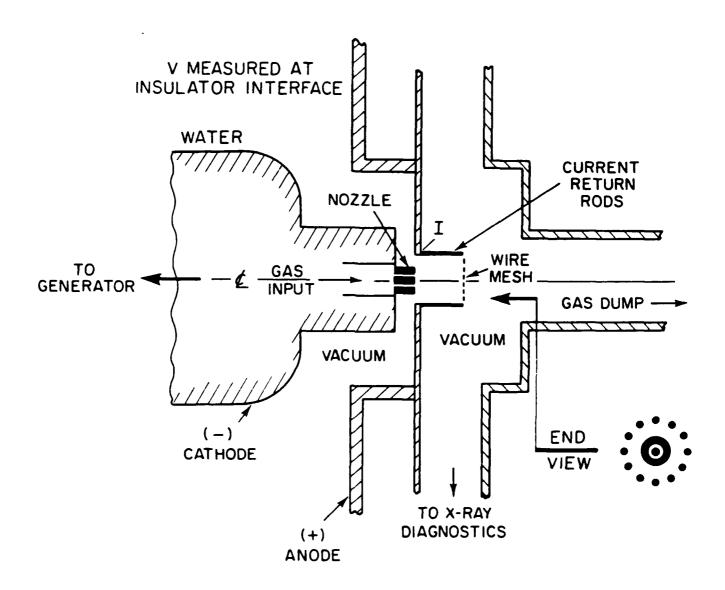
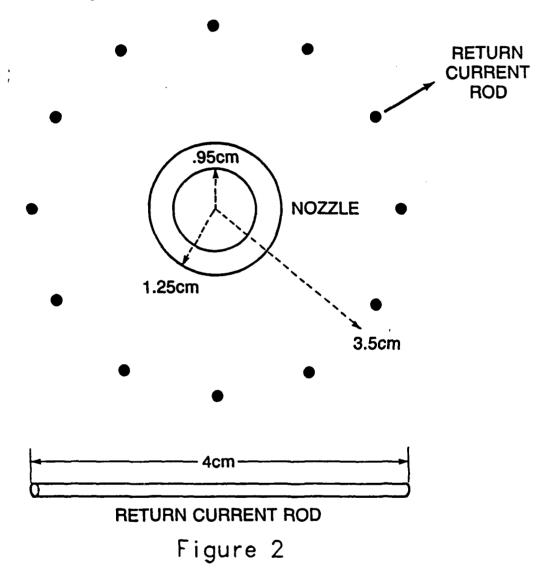
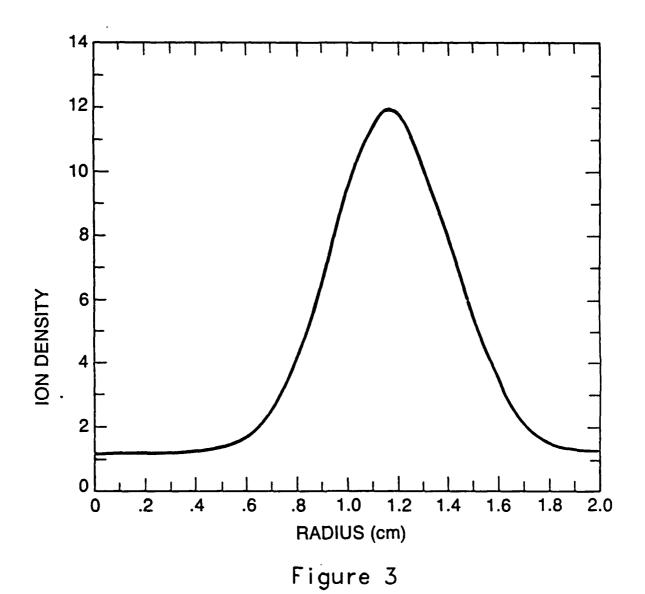


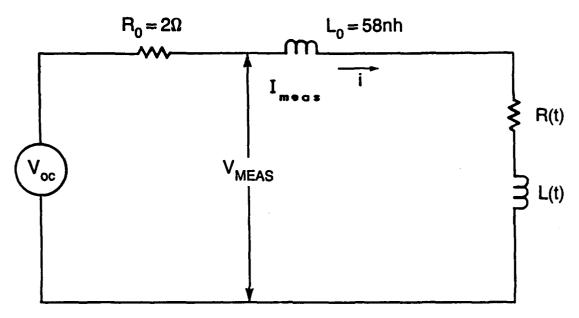
Figure 1

Schematic Diagram of the Gamble II Diode Region





Gamble II Circuit Diagram



 V_{oc} - OPEN CIRCUIT VOLTAGE

R₀ - MACHINE RESISTANCE

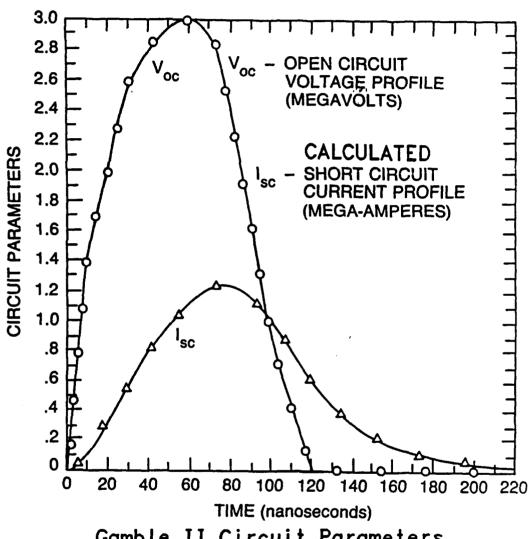
LO - MACHINE INDUCTANCE I - MEASURED CURRENT

R(t) - TIME DEPENDENT LOAD RESISTANCE

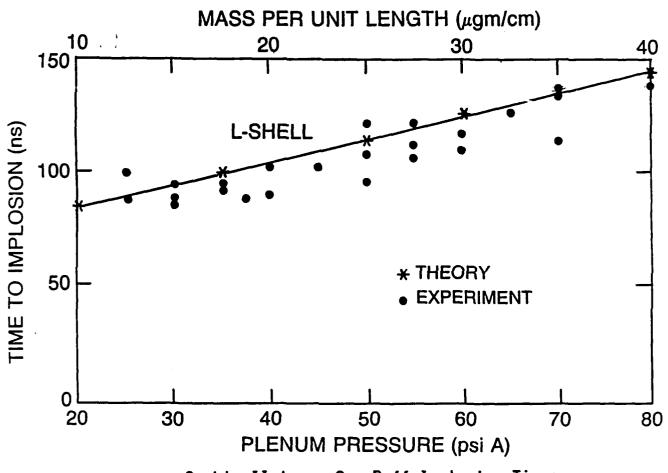
L(t) - TIME DEPENDENT LOAD INDUCTANCE

 $V_{\mbox{\scriptsize MEAS}}$ - MEASURED VOLTAGE

Figure 4

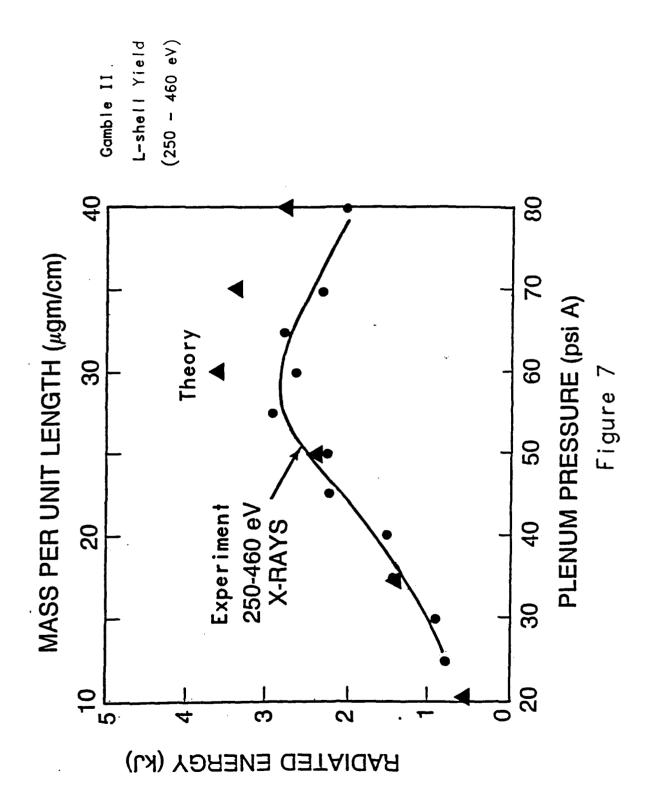


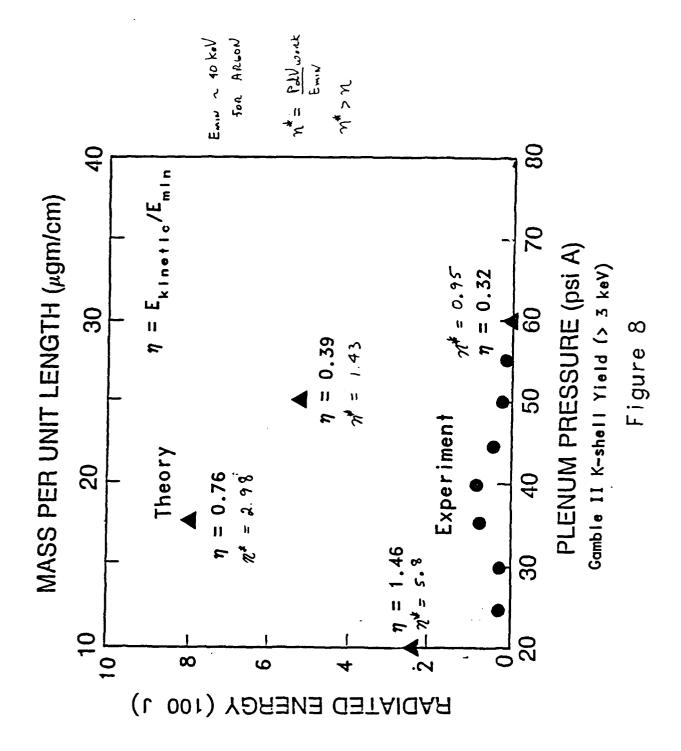
Gamble II Circuit Parameters
Figure 5

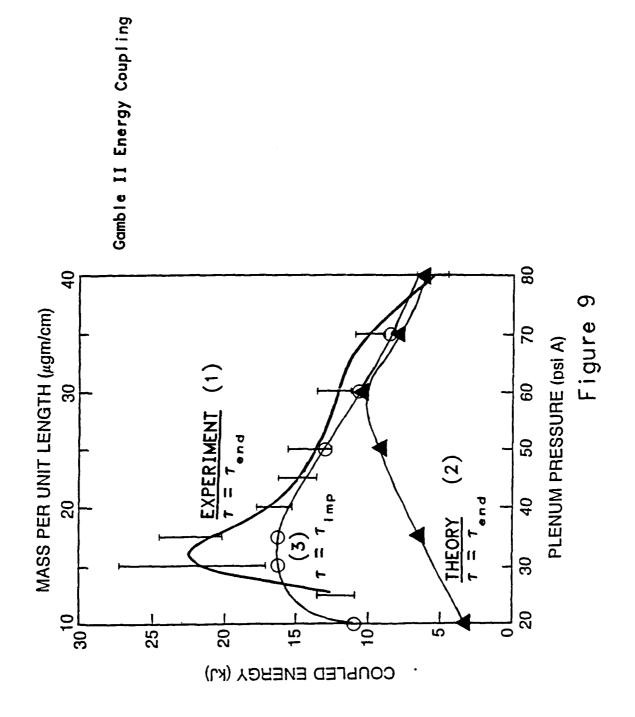


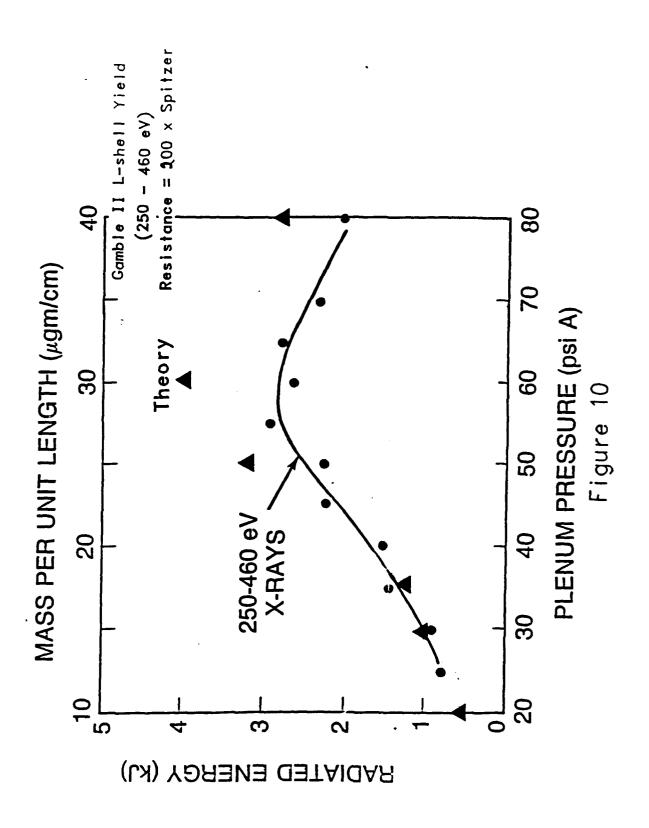
Gamble II Argon Gas Puff Implosion Times

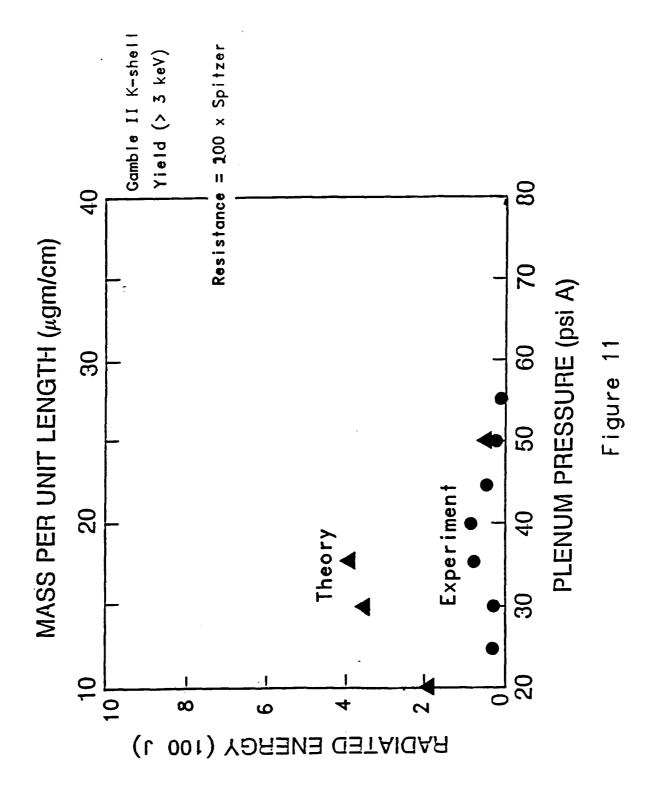
Figure 6

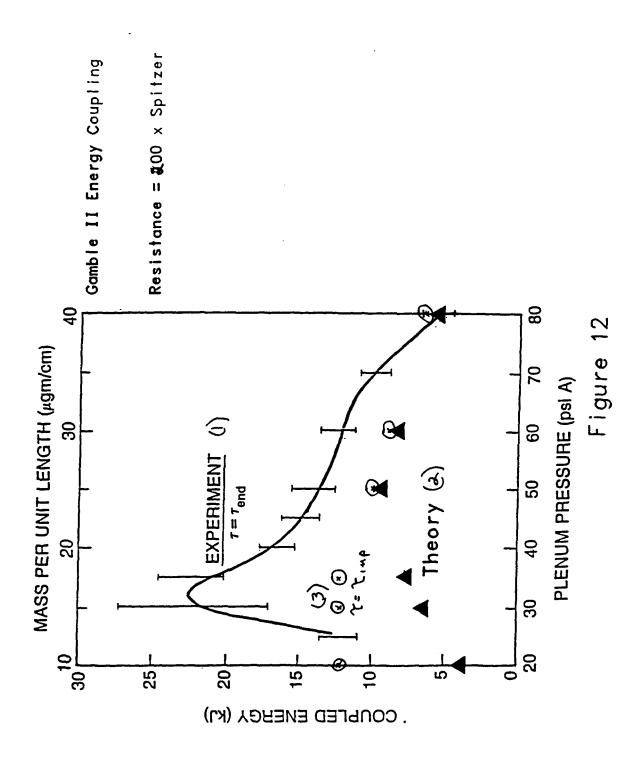




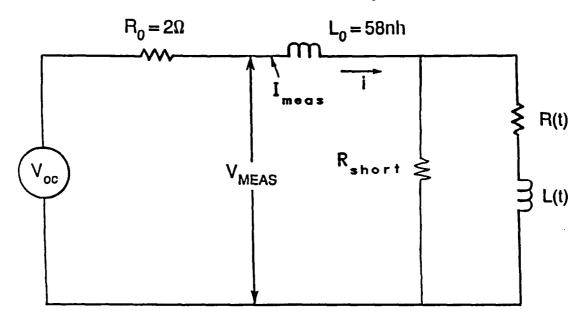








Gamble II Circuit Diagram

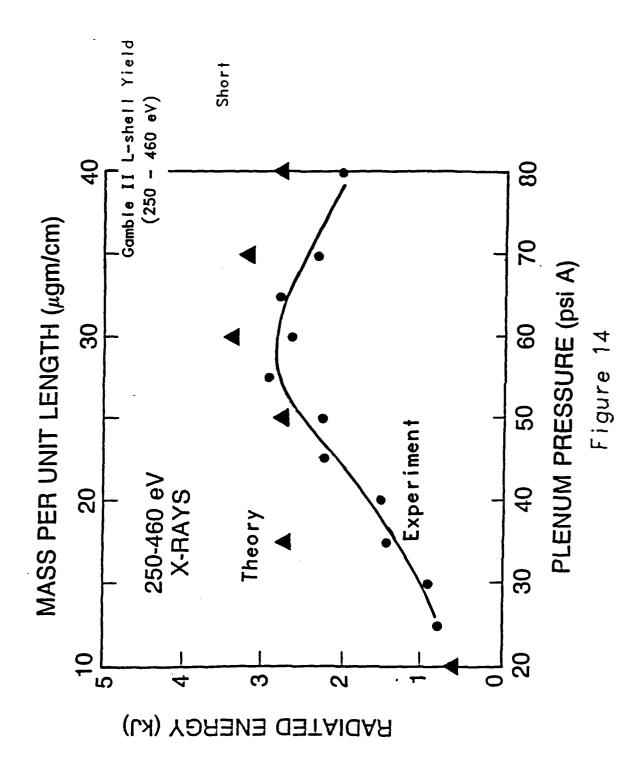


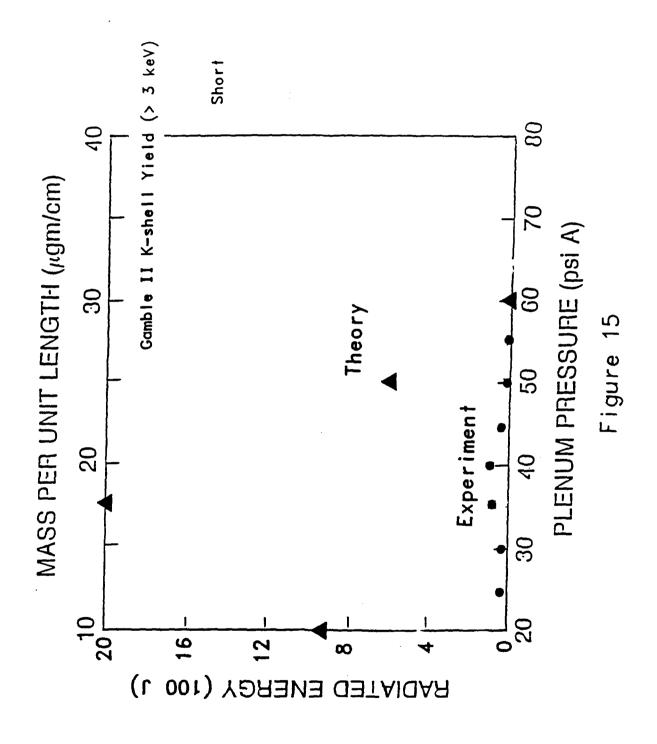
 $R_{\scriptsize{\texttt{short}}}$ is the resistance of the short

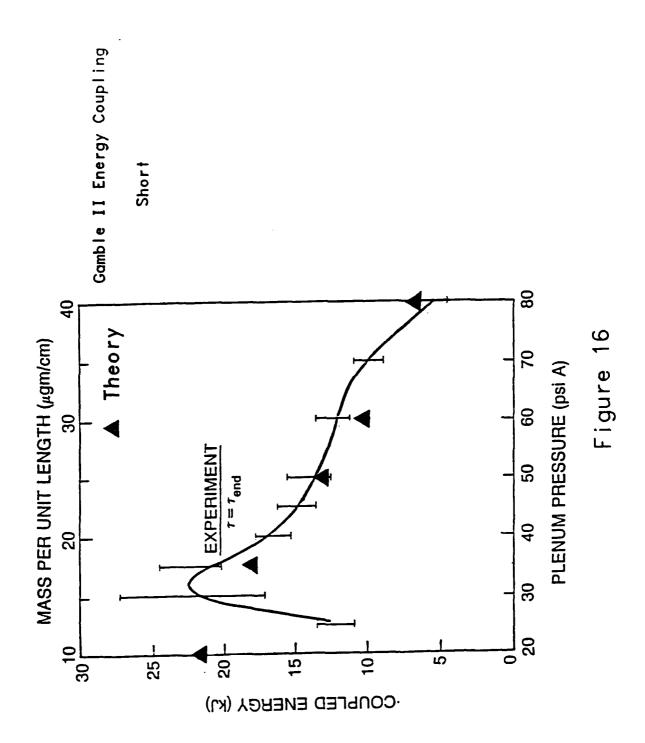
$$R_{short} = 10^7 \text{ x exp}(-1/(r_o-.1)) \text{ ohms}$$

r is the outer radius (cm)

Figure 13







Double Eagle Circuit Diagram

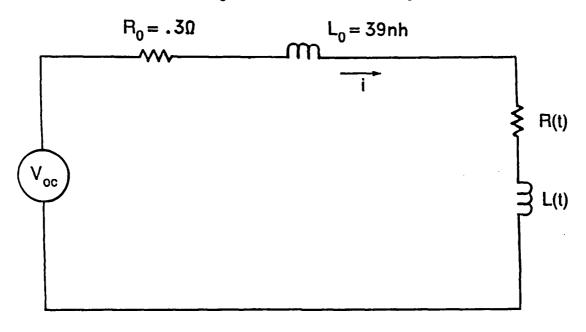


Figure 17

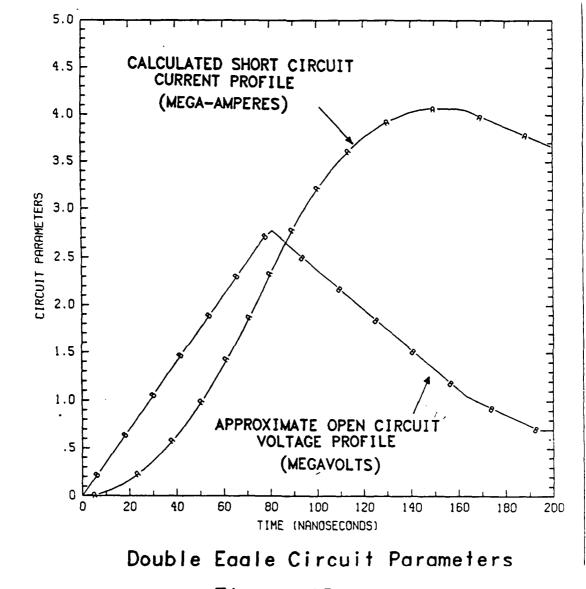


Figure 18

Physics International Aluminum Data

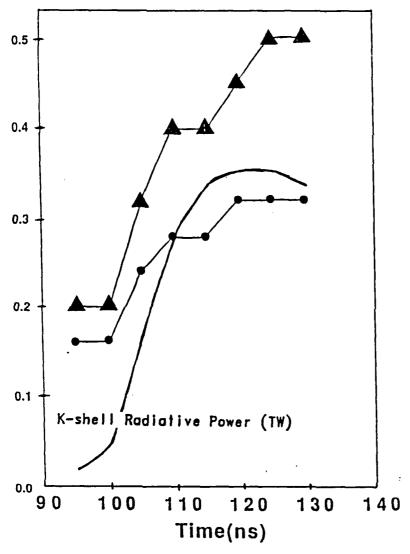


Figure 19

(Chris Deeney)
Mass -- 105 μg/cm
12 wires
20 mm diameter array
26 mm diameter return cage
K-shell yield -- 18kJ
Total yield -- 60 kJ
XRD FWHM -- 35 ns

- ▲ L-shell Radius (cm)
- K-shell Radius (cm)

$$\Delta L = 6.2 \text{ nh}$$

$$\frac{1}{2}\Delta L I^2 < 38 \text{ kJ}$$

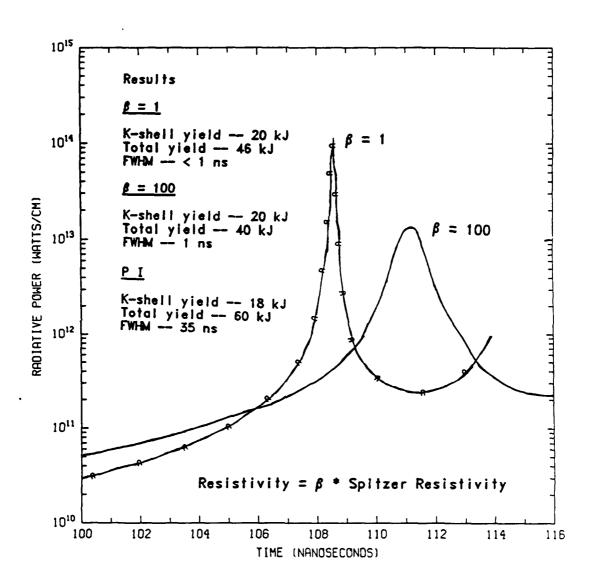


Figure 20

III. THEORETICAL INVESTIGATION OF THE EFFECTS OF SHORT CIRCUITS AND ANOMALOUS HEATING ON AI ARRAY YIELDS

A. INTRODUCTION

An important objective of the Radiation Hydrodynamics Branch is to promote understanding, interpretation, and prediction of the dynamics and radiation from a Z-pinch implosion based upon numerical simulations. Such studies can lead to new methods and approaches for improved coupling between the pulse power machine and the pinch load, as well as enhancement in the radiative yields from the implosion. The focus of the present work is a direct comparison between experiments and numerical simulations of imploding aluminum wire arrays on the DOUBLE EAGLE generator. In order to reproduce the observations the analysis led to the inclusion of a short circuit in the feed and anomalous resistive heating within the imploding plasma.

The DOUBLE EAGLE generator of Physics International Company consists of a 1.5 MJ Marx generator with a water pulse line to the front end load through a 39 nh vacuum transmission line (VTL). The generator has an output impedance of 0.3 W. The voltage pulse peaks at 2.75 MV with a 120 nsec FWHM. The current for a fixed load of negligible inductance rises to 4.5 MA approximately 50 nsec after the peak of the applied voltage. Up to 6 TW of electrical power can be delivered to the VTL. A 2 cm long cylindrical array of 12 aluminum wires was strung at the center of the converging VTL geometry. The array mass M and initial radius $R_o(0)$ were varied but in such a manner that the energy coupling from the generator to the imploding load was kept nearly constant. According to simple thin shell implosion modeling, this constraint can be realized as long as the product $MR_o^2(0)$ is constant. Table 1 lists the initial array radius $R_o(0)$, the total mass of all wires M, the line mass density $MR_o^2(0)$, and the number of experiments run with these initial conditions. Other experiments were performed, but we limit the discussion in the present report to those experiments with a line mass density near 200 μ gm cm².

TABLE 1. Experimental Array Configurations.

$R_o(0)$	M	$MR_o^2(0)$	number of shots	
(cm)	$(\mu \mathrm{gm})$	$(\mu { m gm~cm^2})$	3 - 3 - 3 - 3 - 3 - 3 - 3 - 3 - 3 - 3 -	
0.45	948	192	4	
0.625	554	216	3	
0.75	328	185	6	
1.0	210	210	2	
1.25	160	250	2	

In the systems simulation the pulse power generator DOUBLE EAGLE was treated as a voltage driven circuit as in Fig.1. The source voltage $V_s(t)$, total inductance, and impedance of the VTL were listed above. For some of the runs in the present study a short circuit path was added in parallel to the pinch voltage load. The short represents radial arcing within the VTL which, from the geometry of the VTL, most likely occurs 4 nh upstream from the pinch. Thus the total inductance of the VTL was spit into an upstream $(L_a = 35 \text{ nh})$ and a downstream $(L_b = 4 \text{ nh})$ component. The arcing was modelled by having the resistance across the short circuit path decrease from 1000 Ω to 10^{-3} Ω in 2 nsec once the load voltage exceeds 3 MV. As the pinch implodes the load voltage grows rapidly due to the motional resistance. Hence the precise load voltage at which the short is triggered is not a sensitive parameter, as long as the value is larger than the maximum of V_s .

The radiation-hydromagnetic simulation of the implosion on DOUBLE EAGLE is comprised of a single zone radiation-hydromagnetic code fully coupled to an equivalent circuit model described above. Separate momentum equations for the leading and trailing plasma-vacuum interfaces were followed. Detailed atomic excitation and ionization rate equations were solved for the equation-of-state, and the probability-of-escape formalism was used for the radiation transport. Initial calculated results of the implosion and resulting radiative yields were found to be quite discrepant from the observations. In the interest of bringing the simulation results more into line with those of the experiments, we subsequently include (i) a short circuit in the vacuum transmission line and (ii) an arbitrarily enhanced resistivity in the model.

TABLE 2. Simulation Conditions in the Run Sets.

Run Set	Short	Resistivity
A	No	Spitzer
В	Yes	Spitzer
C	Yes	eqn.(1) with $\beta = 100$

We considered three separate sets of simulation runs depending on the presence of the short circuit and the anomalous resistivity. The conditions for each set are listed in Table 2. For the simulations of set A, termed the standard case, there was no short circuit in the VTL and Spitzer resistivity was used. For set B, a short circuit was added according to the conditions discussed above. The runs of set C also have a short but, in addition, we employed an enhanced resistivity η which increased as the plasma pinches. Specifically,

$$\eta = \eta_{Spitzer} \times \{1 + \beta [1 - (\frac{R_o(t)}{R_o(0)})^2]\}. \tag{1}$$

B. RESULTS

Figure 2 displays the implosion time t_{imp} as a function of the initial wire array radius $R_o(0)$. The average t_{imp} for those experiments at the same $R_o(0)$ are shown as circles with the error bars extending to the maximum and minimum of the observed values. The implosion times for the experiments are determined by extrapolating the linear section of the rising current trace back to zero and measuring the temporal delay till the onset of the K-shell pulse. The results from the simulation sets, determined by the same prescription and with the same intrinsic error, are also displayed in Fig.2. These results are fairly close to the experimental points, except at $R_o(0) = 1.0$. Of the two experiments performed at this radius only one measurement of t_{imp} could be obtained. So the error bars on this data point are uncertain. On the other hand, the two experiments at $R_o(0) = 1.25$ cm both gave the same t_{imp} . We note that the implosions all occur long before the peak of the machine current at 125 nsec. This feature of the present series of experiments is opposite from most of the previous studies on wire array and gas puff implosions.

We compare the observed total (Y_{tot}) and K-shell (Y_K) radiative yields against the results from set A in Fig. 3. The simulation results are plotted as a solid line for the Y_{tot} , and a dashed line for Y_K . The dotted line is the maximum kinetic energy E_K of the imploding shell. We note that the yields from the simulations both exceed the measured values and display a broader distribution as a function of $R_o(0)$. In addition to this first (i) problem of the yield comparison, we found other pertinent differences between the experiments and the results using the standard set A conditions. (ii) The calculated current displays a rapid drop from a peak of 3.3 MA at the time of implosion and subsequently either decays or undergoes a series of oscillations with sharp minima. The observed current trace shows no such dramatic behavior. (iii) The minimum pinch radii $R_{o,min}$ for the models of set A are about 1×10^{-2} cm, much smaller than the observed 0.1 cm radius for the x-ray emitting region. (iv) Finally, the K-shell radiation in the models of set A emerge as a spike spanning less than 1 nsec about the implosion time, while the observed K-shell pulse width is over 20 nsec FWHM. The excessive yields in the regime of small $R_o(0)$ reflect a radiative collapse after implosion in the simulation models.

These problems for the set A simulations indicate that the physical model is incomplete. Let us concentrate on the first problem of the excessive yields. This discrepancy suggests that more energy is coupled to the pinch load in the simulations than in the actual experiments. One way to reduce the yields in the simulations would be to reduce the electrical energy reaching the pinch. Since the implosion occurs before the peak of the machine current, the energy coupling between the generator and the pinch would be reduced if arcing in the VTL occurred upstream of the load. Furthermore, whether the plasma bounces or undergoes radiative collapse, the load voltage reaches values several times larger than the maximum of the source voltage. Such large voltages would lead to a breakdown in the VTL. This led us to consider run set B wherein arcing is modelled by a radial short circuit in the VTL once the load voltage exceeds 3 MV. After the short occurs, negligible energy can be transferred from the generator to the pinch and the amount of energy already in the pinch region downstream of the short is trapped. The objective of reducing Y_{tot} and Y_K from the values for the standard conditions was accomplished as shown in Fig. 4, although Y_{tot} is somewhat too small for the massive arrays and the

distribution of Y_K as a function of $R_o(0)$ is still broader than the same distribution for the data. Moreover, the last two problems with the standard set runs remain: (iii) the pinch radius is too small, and (iv) the K-shell pulse width is too narrow compared to the observations. We emphasize that the discrepancies in the radii and pulse widths are also characteristic results from multi-zone 1-D radiation-hydromagnetic codes, and are not a peculiarity of our computationally faster one zone modelling.

It appears that some further physical mechanism not considered in run sets A or B causes a rapid thermalization of the imploding plasma before the pinch contracts to such high densities that a radiative collapse ensues, as in the simulations. Moreover, this thermalization process must force a gentle bounce of the plasma in order to produce the observed long K-shell pulse widths. Within the confines of a 1-D cylindrically symmetric simulation code we can mimic the effects of a rapid thermalization by employing an enhanced resistivity as in eqn. (1) for run set C. Since the velocity increases dramatically just prior to assembly on axis, the earlier bounce means a reduction in the kinetic energy of implosion. This reduction in energy available for radiation should be compensated by the enhanced resistive heating.

The results for the radiative yields for run set C are shown in Fig.5. We note the improved agreement with the observations for Y_{tot} and the significantly more narrow distribution of the calculated K-shell yields over $R_o(0)$. But the peak of Y_K has been increased above the results of run set B and is larger than the data by a factor of ~ 3 . As in Sets A and B, the resistive heating dominates the implosion energy input to the plasma for small $R_o(0)$. In this domain the models of set C do maintain a Bennett equilibrium for ~ 10 nsec during which the K-shell radiation emerges. But then, unlike the models of the previous sets, they rebound instead of collapsing to a state with the Pease-Braginskii current. One of the main problems uncovered in the runs for sets A was the smallness of the minimum pinch radius $R_{o,min}$. There is slight improvement in agreement as we add a short in the VTL (set B) and then enhanced resistivity (set C), but the calculated pinch radii remain too small.

A second problem in the simulations of run set A was the narrow K- shell pulse width, calculated to be < 1 nsec. A specific comparison of the calculated and measured currents and the K-shell pulse for $R_o(0) = 0.625$ cm is shown in Fig.6. In Fig.6a, from set A, the large increase in the load voltage at the time of assembly on axis causes the current to drop abruptly. In Fig.6b, from set C, there is also a decrease in the current through the load (I_b) . But the current upstream of the short (I_a) undergoes an inductive notch, then rebounds and continues to rise. These features are qualitatively similar to the measured current profile displayed in Fig.6c. In Figs.6a and 6b the normalized K-shell pulse for the models is shown for comparison with the filtered XRD signal in Fig.6c. Again the addition of an enhanced resistivity leads toward agreement with observations, but the calculated widths are still too narrow.

We have presented a quantitative comparison between experiments and simulations of several dynamic and radiative features of imploding z-pinches. The experiments were performed on DOUBLE EAGLE with aluminum wire arrays. The simulations used a single zone, non-LTE radiation-hydromagnetic code in order to survey a large range of parameter space in an efficient manner. For the standard models (set A) we found that the total and K-shell radiative yields were larger, while the pinch radii and K-shell width

pulse widths were smaller than the observed values. These last two problems are likewise found in muti-zone codes. In order to bring the simulations more into agreement with the experiments we added to our models a short circuit in the vacuum transmission line (set B) and then an arbitrarily enhanced resistivity (set C). We saw from sets A and B that a short in the feed does reduce the total energy coupled into the load but does not significantly affect the yield distribution, even when the short occurs before peak current. Only with the inclusion of an enhanced resistivity was a noticeable change found in the distribution of yields with initial radius. This improved the simulation modelling for the total yield, current profile, and K-shell pulse width. However there still remain discrepancies, and an explanation of the observed narrow distribution of the K-shell yield remains an unsolved problem. Further details can be found in the published paper by Giuliani et al¹.

C. DISCUSSION

Future research on PRS should emphasize an interplay between experimental diagnostics and systems simulations. The presence of a shorting arc in the vacuum transmission line is very relevant for implosions which occur before the peak in the generator current. If the time of implosion occurs after the current peak all of the generator energy destined for the front end has been put into the pinch. Hence shorting will not reduce the total energy coupled to the plasma. However, a controlled short which can be triggered after the implosion may trap the electromagnetic energy in the front end region and the plasma can continue to draw upon this energy supply. Possible consequences could range from an elongated K-shell pulse width to a faster disruption of the confined plasma pinch. It would be useful to a systems analysis if the current (I) and the time derivative of the current (dI/dt) could be measured as close as possible to the pinched plasma. If a short is occuring a comparison of I upstream and near the pinch would be indicated by a splitting of the two currents. In addition, it has been found from other studies of pinch phenomena that dI/dt is a very sensitive indicator of the resistive and inductive coupling between the generator and the plasma.

Although the present theoretical analysis points toward the development of a predictive capability, the existence and physical mechanism driving any enhanced resistivity cannot be ascertained from the present model. It does not seem likely that an enhanced resistivity arises from some micro-instability, for the imploding plasma is quite collisional and the drift velocities are smaller than the sound speed of the plasma. On the other hand, the use of an anomalous resistivity in the models to better match observations may be a consequence of a rapid thermalization during the implosion. This thermalization could arise from compression of axial magnetic fields arising from the self-generated field instability in the azimuthal direction, or from rapid magneto-hydrodynamic convective or sausage instabilities in the plasma shell during the implosion phase. These latter processes would lead to turbulence which is in effect a transfer of the directed kinetic energy of implosion into a random kinetic energy of macroscopic eddies. As in classical trubulence, the eddies motion can lead to effective diffusion processes which in turn mimic an enhanced resistivity.

In the simulation domain the investigation of such phenomena should be addressed in several stages. First, 2-D simulations of the implosion with initial small perturbations

should be carried out to determine effective growth rates, lengthscales and the responsible driving term in the equations. If it is found that the rates and lengths are small compared to the implosion time and pinch length then a detailed simulation of the macroinstability would be prohibitively expensive. Instead a $\kappa - \epsilon$ turbulence model for magnetohydrodynamic plasmas needs to be incorportated into the simulations. In the experimental domain the employment of high resolution time and space spectroscopy for optically thin transitions radiating during the implosion phase could reveal the velocity structure of the plasma. An emitting shell with only radially inward velocities would present a bimodal distribution in frequency space which would separate as the plasma approaches the axis. If the shell does go unstable, the line profile would fill in, and the degree of filling in would be indicative of the conversion of directed kinetic energy into turbulent energy.

REFERENCES

1. J. L. Giuliani, Jr., J. E. Rogerson, C. Deeney, T. Nash, R. R. Prasad, and M. Krishnan, Journal of Quantitative Spectroscopy and Radiative Transfer, 44, 471-484 (1990).

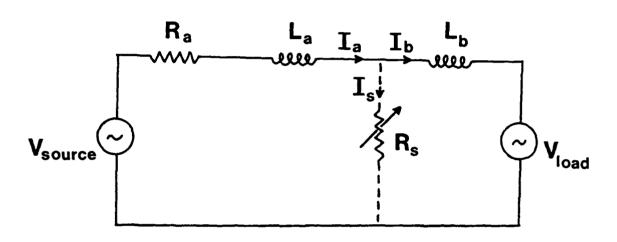


Fig.1 Circuit model used for DOUBLE EAGLE pulse generator. Ia is the current through the vacuum transmission line (VTL), and Ib is the current through the pinch load. Arcing in the VTL is modelled by the short circuit with variable resistance.

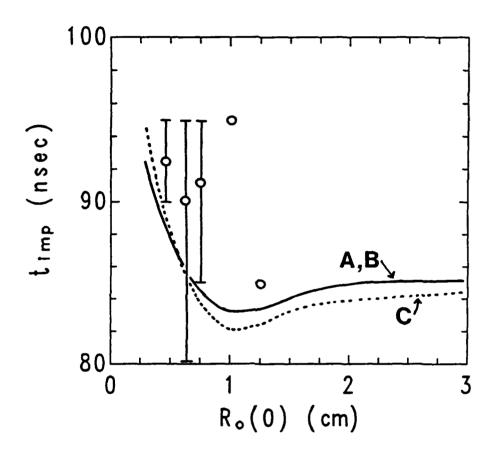


Fig.2 The implosion times timp for the models of sets A, B and C versus the initial array radius $R_o(0)$. Circles represent the average values for the experimental data and the extent of the error bars indicate the extremes of the measurements.

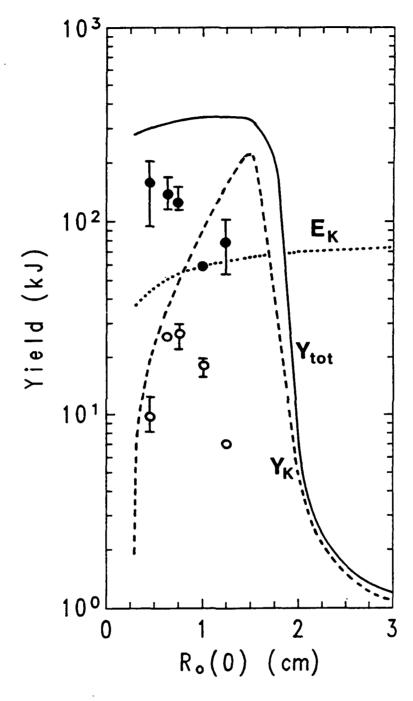


Fig.3 The total yield Y_{tot} (solid line) and the K-shell yield Y_K (dashed line) for the simulations of set C versus initial array radius $R_o(0)$. Filled circles are the average values of the experimental data for the total yields; empty circles for the K-shell yields. The error bars extend to the extremes of the measurements. The dotted line is the maximum kinetic energy E_K of the implosion.

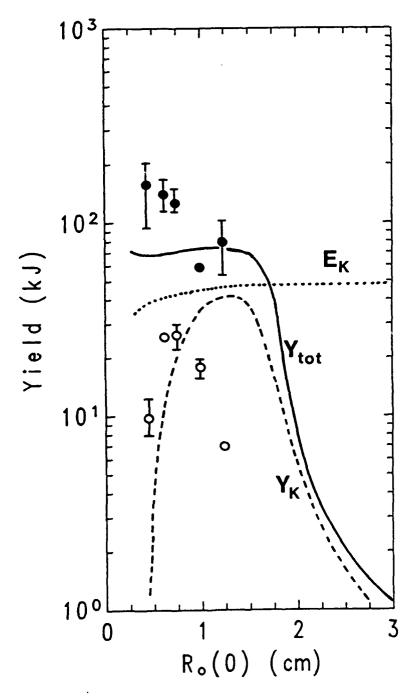


Fig.4 The same as Figure 3 but for run set B.

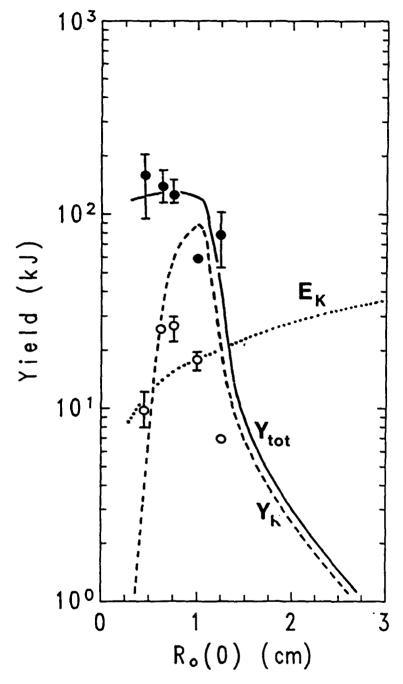
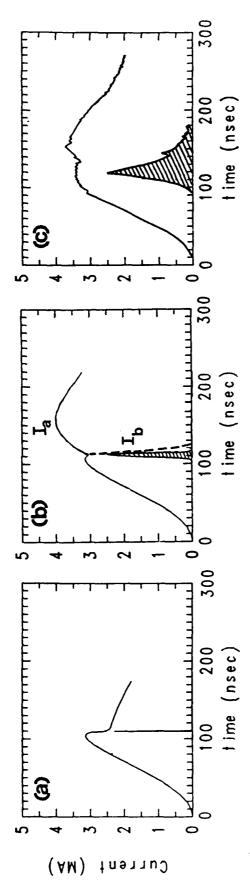


Fig.5 The same as Figure 3 but for run set C.



short is triggered. (c) Experimental current profile for the same initial conditions. The K-shell pulse is shown as a spike in (a) and hatched in (b). The filtered XRD signal is also Fig.6 (a) Calculated current for $R_o(0) = 0.625$ from the model of set A without a short through the pinch (Ib) follows the current in the vacuum transmission line (Ia) until the shown hatched in (c). The units for the intensity are arbitrary since the peak has been circuit. (b) Same run but from set C with a short and enhanced resistivity. The current normalized to the same value in (a), (b), and (c).

IV. SCALING L-SHELL IONIZATION DYNAMICS

Any upgrades made to the atomic rates used in the radiation-hydrodynamic calculations, automatically lead to improved diagnostics and predictions. Over the past few years, a fairly extensive atomic data base covering the K-shell region has been built up and used to obtain detailed diagnostics [1] and K-shell emission scaling relationships [2,3]. In the past, most work was done with low Z materials, such as aluminum. Recently, however, interest is turning to higher Z materials, such as nickel and selenium.

The higher the atomic charge Z is, the harder it is to ionize to the K-shell, which means that the L-shell becomes important. A detailed L-shell atomic data base, comparable to the existing K-shell one, could result in improved an detailed diagnostics and in reliable scaling relationships in the L-shell region. To do this work, however, requires accurate L-shell atomic data.

In the K-shell region, the two most dominate processes that determine the degree of ionization balance are collisional ionization and radiative recombination. Recent work has shown that in the L-shell region of selenium, dielectronic recombination is about three or four orders of magnitude larger than radiative recombination [4]. Therefore, in the L-shell region, the two dominate processes are collisional ionization and dielectronic recombination. To neglect, or to use inaccurate, dielectronic recombination or collisional ionization rates would be tantament to using incorrect physics in calculating the atomic spectra. In the existing atomic models, the collisional ionization and the dielectronic recombination rates are calculated using the average atom method. It is important to improve these rates. The dielectronic rates have been calculated and scaled [5] for F-like Ar, Ti, Fe and Se ions. The ionization collision strengths have been calculated and need to be scaled for Li-like through Ne-like Fe and Se ions.

1. Atomic Models for Se and Fe

Two large L-shell atomic data bases for Se and Fe have been developed over the last three years. From them by scaling, we hope to obtain models for nearby moderate Z elements. For energy level and oscillator strength calculations, the three stage computational atomic structure package of R. D. Cowan was used. The first stage (called RCN) is a bound-state radial wavefunction code which uses Hartree Fock (HF) or a modified Hartree Fock (HFR) approximation to solve for the configuration average energies, bound and continuum wavefunctions, Slater integrals, and spin-orbit parameters. The HFR approximation modifies the differential equation to contain relativistic corrections for the mass-velocity and Darwin terms. The second code (called RCN2) calculates configuration-interaction integrals and multipole moments by using the bound and continuum radial orbitals from RCN. The third code in this package is a configuration-interaction structure code (RCG) which computes energy levels and intermediate-coupling eignevectors by diagonalizing the Hamiltonian matrix in any one of seven different pure coupling schemes. For the models under development, LS coupling was used. The energies are provided for each individual j value by RCG. There were 7 individual energy levels included in this model. The $2s^22p^53s$, $2s^22p^53p$, $2s2p^53d$, $2s2p^63s$, $2s2p^63p$, $2s2p^63d$, $2s^22p^5(n=4)$ were averaged over to obtain the average energies and Einstein A values.

Collision strength calculations for electron impact excitation were completed using two different techniques. All dipole transitions were calculated using the semiclassical impact parameter method [6]. The energy levels and oscillator strengths generated using Cowan's code were used as input in these calculations. All other collision strengths were calculated using the more sophisticated distorted-wave approximation [7,8].

There are several weaknesses in this model. First, all mixing between the energy levels was ignored, i.e. each level was assumed pure. Because of the inflexibility of the available software, not all excited-state transitions were calculated. In most cases, this tends to be a good approximation as transitions were the spin changes tend to have smaller collision strengths and transitions where the spin is unchanged.

2. Scaling

Although, for more accuracy, it would be good to have collision strengths from a third ion in addition to iron and selenium, the two sets of collision strengths can be scaled in energy and in Z using the formula give in Ref. 9:

$$CS(X,Z) = \frac{[CO + C1/X + C2/X^2]}{(Z-B1)^2} + \frac{C3*LN(X)}{(Z-B2)^2}$$

where Z is the atomic nuclear charge and X is the ratio of the collision energy of the electron to the threshold energy of excitation. CO, Cl, C2, C3, Bl and B2 are constants to be determined. The scaling for a fix Z, produces collision strengths that agree with the data (obtained previously from Cowan's codes as described above) to within 10%. In trying to scale with Z and X, we have run into some numerical inconsistencies between the data and the fitting curves which need to be investigated. Figure 1 shows a ground to excited transition for Ne-like iron and selenium where the fit (solid line) and the data (crosses and stars) agree quite well. Figure 2, however, shows an excited to excited transition for Ne-like iron and selenium in which the fit is very poor at low X. A better fit may need to be found. collision strengths can be scaled in Z, atomic models can be constructed for any Z between 26 (iron) and 34 (selenium) and possibly beyond.

With the collision strengths scaled in Z and dielectronic recombination rates calculated for all of the L-shell, we can determined accurate scaling relationships for the emission, similar to the work done in references 2 and 3 in the K-shell. Spectral diagnostics can also be developed from the same data base to test consistently the consequences of these predictions experimentally.

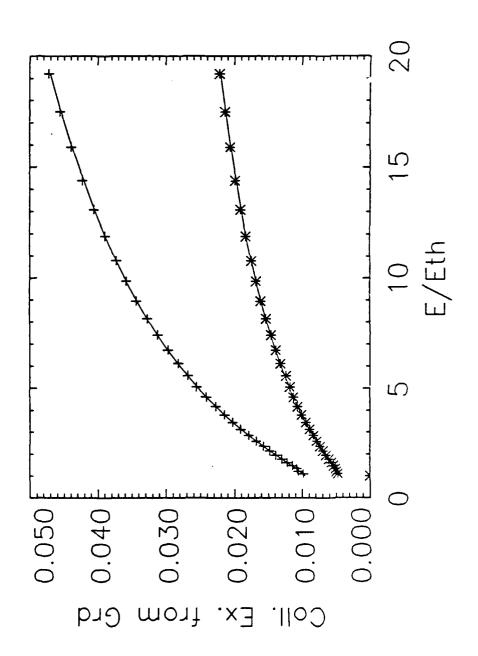


Fig. 1. The $2s^22p^6$ to $2s^22p^53s$ ground to excited transition in Ne-like iron (+) and selenium (*). The solid line is the fit in X and Z to the data points.

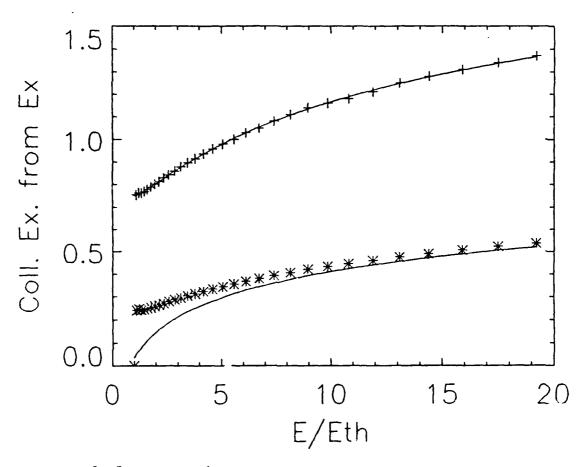


Fig. 2. The $2s^22p^53s$ to $2s2p^63s$ excited to excited transition in Ne-like iron (+) and selenium (*). The solid line is the (preliminary) fit in X and Z to the data points.

References

- 1. Coulter, M. C., K. G. Whitney, and J. W. Thornhill, J. Quant. Spectrosc. Radiat. Transfer 44, 443 (1990).
- 2. Whitney, K. G., J. W. Thornhill, J. P. Apruzese and J. Davis, J. Appl. Phys. 67, 1725 (1990).
- 3. Thornhill, J. W., K. G. Whitney and J. Davis, J. Quant. Spectrosc. Radiat. Transfer 44, 251 (1990).
- 4. Dasgupta, A., K. G. Whitney and M. Buie, Bull. of the Am. Phys. Society 35, 2077 (1990).
- 5. Dasgupta, A., K. G. Whitney, Phys. Rev. A 42, 2640 (1990).
- 6. Cowan, R. D., "The Theory of Atomic Structure and Spectra", Univ. of California, Berkeley (1981).
- 7. J. Davis, J. Quant. Spectrosc. Radiat. Transfer 14, 549 (1974).
- 8. Milan Blaha's Code
- 9. Magee, N. H. and A. L. Mertz, Appendix B of LA-8267-MS Los Alamos Report.

V. AVERAGE ATOM MODELING OF L- AND M-SHELL IONIZATION DYNAMICS

Detailed calculations of radiation from high temperature plasmas, particularly from elements with high atomic numbers, generally involve the solution of a large set of coupled rate equations. This requires the storage of a significant amount of atomic data and the usage of large amounts of computer time to treat these phenomena accurately. To get around this problem, an average atom $\operatorname{model}^{1-4}$ is sometimes used. This method replaces the ensemble of actual specific ionization stages and electronic configurations by a single fictitious hydrogen-like ion with a set of shell populations P_n . In our case, these shells are connected by a set of n hydrogenic rate equations which are solved for the P_n ; using these P_n , various atomic processes are treated. Hopefully, the results are a reasonable approximation of the behavior of the actual physical system.

Our effort has been based primarily on the work of Post, et.al.⁴, who have developed an extensive model for the coronal regime. They use a detailed scheme for treating line emission from transitions in which the principal quantum number n does not change. In our model, the nl subshells are assumed to be statistically populated, and their energies are estimated using hydrogenic formulas for the level-splitting and the average energy of the shell. Thus we can treat the same type of transitions.

Hydrogenic energy levels are calculated using atomic screening parameters developed by $More^5$. Once we have the average charge, the P_n , and the energies E_n , we can generate line, bound-free, and free-free radiation.

Apruzese and Kepple⁶ have calculated line emission from cylindrical Krypton plasmas using a detailed atomic model (DCA); their Krypton model has 162 levels and 511 lines. Using a constant line density of 1.55*10¹⁷ ions/cm and an **lectron temperature of 1.0 keV, they calculated the cooling coefficient for line radiation at various ion densities by changing the cylinder radius. Local angle and frequency averaged escape probabilities were used in calculating this emission, and Voigt profiles were assumed for the line shapes.

The rate equation average atom model was used to estimate the optically thin line radiation cooling rate for the same conditions. The equations were solved in the steady-state approximation to obtain the E_n and P_n . The results are shown in Figure 1, where the Apruzese-Kepple optically thin calculations are also given. For ease of plotting on the VAX, the cooling coefficient was multiplied by 10^{-10} , and the ion density was multiplied by 10^{-10} (the cooling rate range is 10^{-28} W*cm³ to 10^{-25} W*cm³, and the ion density ranges from 10^{16} cm⁻³ to 10^{23} cm⁻³). The solid line is the DCA result, and the dashed line is the average atom approximation. Considering the simplicity of the average atom model, the agreement is not bad, being within a factor of about two at the low and high density ends and becoming equal near 10^{21} ions/cms.

Figure 2 shows the average ionic charge obtained in the two treatments for the thin case. The differences are within about 13 per cent. These results indicate that the average atom is capable of yielding reasonably good results for high atomic number plasmas at high temperatures.

In the DCA routines, bremsstrahlung emission is treated via a frequency-by-frequency algorithm rather by escape probability methods. Following Bekefi⁷, an optical depth expression for total bremsstrahlung has been developed, and an escape probability approximation has been proposed.

In the limit of strong self-absorption at all frequencies, a plasma radiates as a blackbody with flux given by the Stefan-Boltzmann law. Consider an infinitely long cylinder of radius R. As R increases, the reabsorption increases until a point is reached at which the volume emission just balances the blackbody radiation from the surface. Equating the two emissions gives

$$1/R_o = 8.20 \times 10^{-38} N_i N_e Z^2 / T_e^{7/2} cm^{-1}$$
,

where T_e is the electron temperature in eV, N_i and Ne are the ion and electron densities in cm⁻³, and Z is the ionic charge. $1/R_o$ represents an effective absorption coefficient integrated over frequency. Thus, for a plasma of effective length L, the optical depth for bremstrahlung can be estimated by

$$\tau = L/R_0$$
.

In the average atom approximation, L is the single path approximation representing an average over all the ray paths^{8,9}. This relation has been used in an escape probability approximation to estimate bremsstrahlung emission from plasmas under a variety of conditions. The escape probability is assumed to be

$$P_{e} = (1 - e^{-\tau})/\tau$$
.

The optically thick radiation is estimated by multiplying the thin emission by P_e . The results have been compared with an exact solution for bremsstrahlung emission from a solid cylinder with constant temperature and density 10 .

Figure 3 gives the exact results and the escape probability approximation for the same Krypton plasma at 1.0 keV as discussed in Figures 1 and 2. Here the bremsstrahlung is given as a function of ion density. The agreement is very satisfactory except at the highest density, where the approximation is 79 per cent low. (Here again the ion density has been scaled down by 10^{10} for ease of plotting on the VAX.)

Figure 4 plots bremsstrahlung calculations for a cylindrical plasma at a constant density of $1.2*10^{19}$ ion/cm³ over a range of electron temperature. Here again, good agreement is obtained except at 1.0 eV, where the approximate result is larger by almost a factor of two.

In this effort thus far, unit Gaunt factors have been assumed. Using actual Gaunt factors could result in some improvement; the exact solution calculates a Gaunt factor at each frequency.

The results in Figures 3 and 4 indicate that this probabilistic approach can be of some use in estimating bremsstrahlung radiation.

References

- 1. B. Stromgren, Z. Astrophys 4, 118(1932).
- S. Chandrasekhar, An Introduction to the Study of Stellar Structure,
 (University of Chicago Press, Chicago, 1939).
- 3. W. A. Lokke and W. H. Grasburger, "XSNQ-U: A Non-LTE Emission and Absorption Coefficient Subroutine", UCRL-52276 (1977).
- 4. D. E. Post, R. V. Jensen, C. B. Tarter, W. H. Grasberger, and W. A. Lokke, Atomic Data and Nuclear Tables 20, 397 (1977).
- 5. R. M. More, JQSRT 27, 345 (1982).
- 6. J. P. Apruzese and P. C. Kepple, JQSRT 44, 529 (1990).
- 7. G. Bekefi, Radiation Processes in Plasmas, John Wiley and Sons, Inc.,
 New York (1966).
- 8. J. P. Apruzese, JQSRT 25, 419 (1981)
- 9. J. P. Apruzese, JQSRT 34, 447 (1985)
- 10. J. L. Giuliani (private communication)

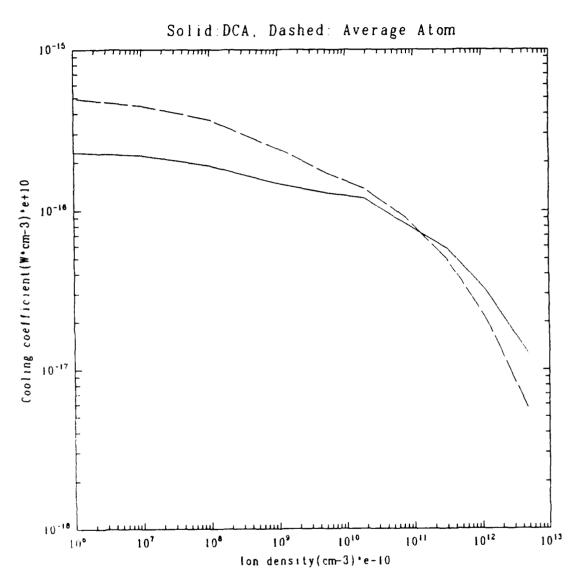


Fig. 1. Line emission cooling coefficient for a cylindrical Krypton plasma at 1.0 keV as a function of ion density. The solid line is the detailed atomic result(DCA); the dashed line is the average atom approximation.

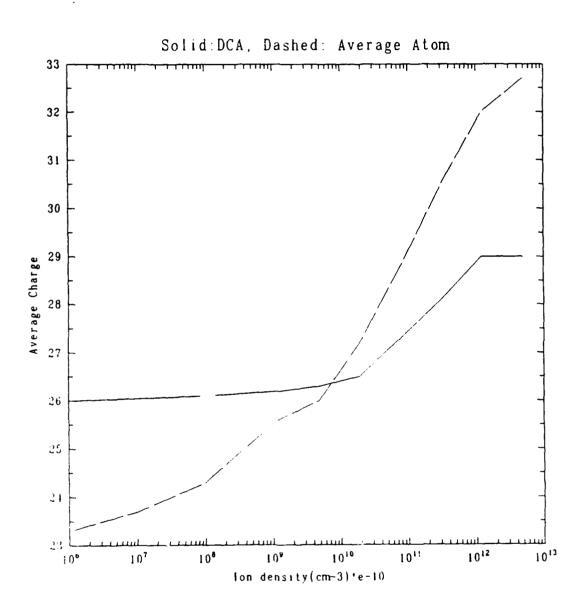


Fig. 2. Average charge for the same plasma as in Figure 1 as a function of ion density.

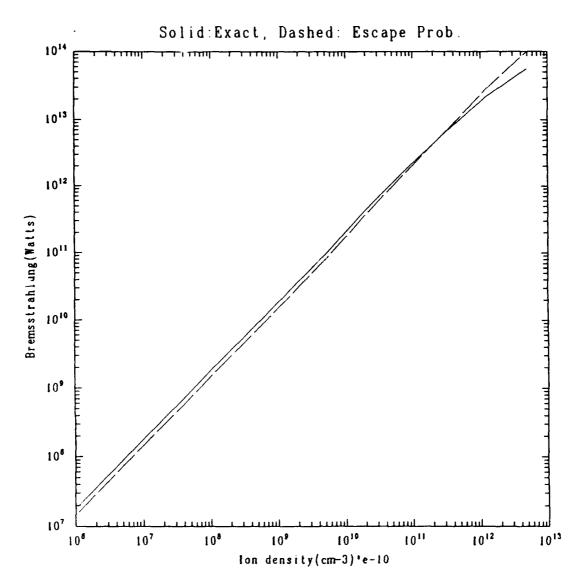


Fig. 3. Bremsstrahlung emission for a plasma at 1.0 keV as a function of ion density. The solid line is the exact calculation; the dashed line is the escape probability approximation.

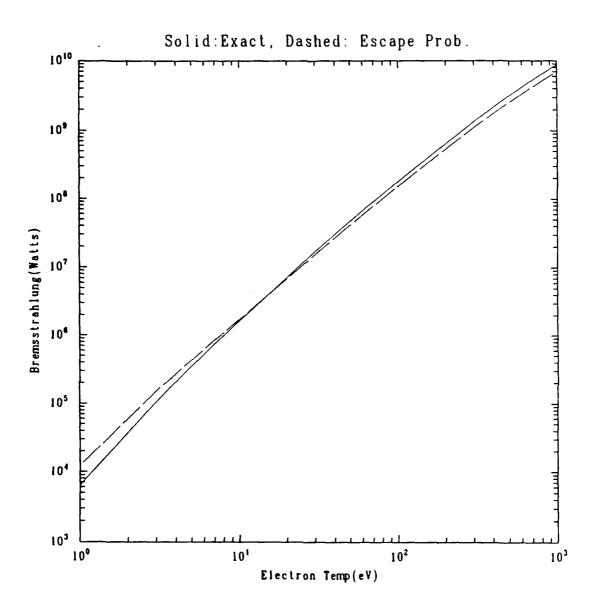


Fig. 4. Bremsstrahlung emission from a plasma at a density of 1.2×10^{19} ions/cm 3 as a function of electron temperature.

VI. Anomalous plasma heating and runaway electron production

INTRODUCTION

Investigations of electron kinetics in PRS loads in the past year have been concerned with the question of runaway production and energy generation in the z-pinch system, and have focused on (1) field diffusion into the plasma and (2) anomalous plasma heating. The formation of high-energy electron beams within a z-pinch may be associated with the "bright spots", which, when prominent, can generate most of the K-shell pinch radiation. In fact, experimental measurements of on-axis bremsstrahlung in z-pinch implosions have shown the existence of electron "runaways", with energies up to several MeV, at times just before the emergence of the pinch bright spots [1,2].

Non-thermal phenomena like these high-energy electron beams are also important aside from their association with bright spots because they can carry a disproportionately large fraction of the current, and because high-energy electrons interact much less with the surrounding plasma than those in the bulk of the distribution. Electron beams promote the formation of hydrodynamic instabilities, (e.g., the m=0 instability), as well as microinstabilities and turbulence, all of which should be important factors in PRS dynamics. Low collisionality at high relative velocity (the runaway effect) means that electron beams formed in the current channel act nonlocally, transporting energy directly to the anode and thus decoupling the PRS device from its power source. The azimuthal magnetic field inhibits this near the edge of the pinch, but as the magnetic field weakens near the axis this nonlocality becomes more important; in addition, it is possible for the plasma to generate a strong enough electric field (E > B, in Gaussian units) to overcome magnetic confinement [3,4].

Our model of these important phenomena is based on a formulation of the Fokker-Planck equation [5], which we have used in conjunction with hydrodynamic simulations [6] to determine the electron energy distribution function during a z-pinch implosion. In the following, we first describe qualitatively our results of how the electron dynamics are shaped by the electric and magnetic field strengths; we note that our model predicts few runaways because electric field effects are smaller than magnetic field effects inside the pinch, and that relatively stronger electric fields and more runaways would be expected if the plasma resistivity were higher than

the commonly-used Spitzer value. The conclusion that an "anomalous resistivity" is important in z-pinch dynamics is consistent with the experimental evidence suggesting that ohmic heating gives a substantial contribution to z-pinch energy production, and that the average pinch resistivity may be 100 times higher than the conventionally-used Spitzer value [1]. As a result, up to four times the theoretically predicted energy has been observed to be coupled into the z-pinch load, indicating more than expected efficiency in generating x-ray radiation. Pulse-width measurements also point to an anomalously high pinch resistivity, and imply as well a pinch structure with turbulence-dominated regions (e.g., a corona).

It seems natural to attribute this anomalous resistivity to plasma turbulence, in a corona outside the pinch and/or in the body of the pinch itself, especially since other PRS devices (e.g., theta pinch) are well-known to be strongly turbulent. We then describe our investigations of z-pinch field diffusion and resistivity: we solved for the diffusion of current into a simulated implosion using artificially enhanced values of the resistivity and analyzed the resulting profiles to see if they promoted or inhibited runaway production. As expected, higher pinch resistivity resulted in a greater enhancement of the distribution function tail and tended to promote runaways. This result motivates the development of a more physical model of turbulent resistivity, a quasilinear theory capable of accurately following the nonlinear and dynamical development of plasma turbulence, and which also is easily incorporated into the collisional Fokker-Planck model that we have used successfully [5] to study z-pinch electron dynamics.

MAGNETIC FIELD EFFECTS ON HEATING AND RUNAWAYS

The theory of electron runaway is well-established for the case of zero magnetic field, or, equivalently, for parallel electric and magnetic field (as in a tokamak). The perpendicular fields found in a z-pinch complicate the situation, however, and whether or not a high-energy electron beam or beams will form in a z-pinch depends on both the absolute magnitude and the relative strengths of the electric and magnetic fields. The electric field must be strong enough to drive the electrons across the collisional and magnetic drag, while the magnetic field determines the electron energies that are most heavily populated by the heating. In addition, the magnetic field acts to isotropize the electron distribution, so that even electric-field-induced enhancements in the high-energy electron population do not necessarily lead to the hydrodynamical instability

and nonlocality associated with high-energy electron beams.

We have investigated electron heating in transverse electric and magnetic fields [5], and summarize here the important points. The electric field, of course, heats the plasma and generally promotes runaways. In the absence of a magnetic field, any electric field causes some degree of electron runaway from the high-energy tail of the distribution; a significant number of electrons run away when the field exceeds the Dreicer field [7] $E_D = mv_{th}\nu_R/e$, where e and m are the electron charge and mass, v_{th} is the thermal velocity, and v_R is the electron-electron collision frequency at the thermal velocity. A magnetic field confines the electrons to their Larmour radius, and increases the electric field needed to produce a significant effect on the electron distribution. In the limit of a very strong magnetic field (cyclotron frequency $\omega_c \gg Z\nu_R$, where Z is the degree of ionization), an electric field of $(\omega_c/Z\nu_R)E_D = mv_{th}\omega_c/Ze$ is needed for significant heating. Thus, in a strong magnetic field the ohmic heating is proportional to $(E/B)^2$, compared to E^2 in the unmagnetized case.

The transverse magnetic field determines at what energy the greatest enhancement of the distribution function will occur. The maximum heating occurs at energy

$$\epsilon_0 = \frac{3}{2}kT \left(\frac{\nu_{\epsilon i}^2}{2\omega_c^2}\right)^{1/3} \tag{1}$$

where kT is the electron temperature and ν_{ei} is the electron-ion collision frequency at the thermal velocity. The ratio of the heated distribution to a same-temperature Maxwellian distribution peaks at this energy, with a sharp falloff both in the low-energy and the high-energy tail of the distribution (the low-energy end tends to be repopulated by Coulomb collisions, while heating of the high-energy tail is inhibited by the magnetic field). A "strong" magnetic field is one that pushes the heating below the thermal energy, so that a depleted-tail distribution results; for a typical z-pinch, this is $B > 2.5 Z n_{18}/(kT)^{3/2}$ megagauss, where n_{18} is the electron density in units of 10^{18} cm⁻³.

The magnetic field also affects the directionality of the electron distribution. If a simple Cartesian expansion of the distribution function is used:

$$f(\vec{v},t) = f_0(v,t) + \hat{v} \cdot \vec{f}_1(v,t), \qquad (2)$$

then f_0 describes the energy distribution and $\vec{f_1}$ gives the directionality (to first approximation) of the electrons (the function $\vec{f_1}$ determines the electric current, to all orders in the expansion).

Ohmic heating increases f_1 and so promotes anisotropy; for a quasi-Maxwellian distribution f_0 , the maximum enhancement of f_1 from ohmic heating is at $\epsilon_{max} \approx 1.6\epsilon_0$. In the magnetized system, the directionality of the distribution changes with energy ϵ , such that the angle $\theta(\epsilon)$ between \vec{E} and $\vec{f_1}(\epsilon)$ satisfies

$$\tan \theta \sim \frac{\omega_c}{\nu_R} \left[\frac{\epsilon}{kT} \right]^{3/2} \tag{3}$$

Thus, at each energy the differential current is in a slightly different direction. An increased magnetic field increases the rate of variation of θ and so promotes mixing (isotropy).

The electric field \vec{E} changes direction during the implosion, and this has an important influence on electron directionality and effective conductivity, and so on runaways. If the relaxation time of the system is long ($\omega_p \ll \omega_c$, where $\omega_p = \sqrt{4\pi ne^2/m}$ is the plasma frequency), the total electric field is mostly in the \hat{z} direction and the current density has a radial as well as axial component; but if the system has time to equilibrate, the current is forced by the system boundaries to be wholly axial and the electric field will then have a possibly substantial radial Hall component.

THE FIELD DIFFUSION PROBLEM

Contrary to experiment, the electric and magnetic field profiles predicted in a z-pinch by MHD simulations do not induce substantial runaway electron production [8]. Because of the slow diffusion of the current into the pinch, the significant electric field effects are always muffled by the accompanying strong magnetic field. Some enhancement of the distribution is seen for intermediate radii, where the magnetic field is still moderate in strength at the diffusive arrival of a significant electric field, but at the pinch edge, the large electric fields actually produce a depleted-tail distribution because of strong magnetic field. Even where enhanced-tail distributions are seen, directionality of the electrons is generally low.

The accuracy of the hydrodynamically-predicted field profiles is difficult to ascertain. Surprisingly little research has been done on the subject of current and field diffusion in any conductors, let alone the z-pinch. Experimental measurements of electric and magnetic fields in the evolving z-pinch have hitherto lacked radial resolution. Numerical studies of the low-density plasma in a plasma opening switch [9] have suggested that conduction patterns are very sensitive to boundary conditions, both in time and space. Recent experimental results on current

penetration in metals [10] are among the first in this area, and not straightforward to interpret.

The relevant equations for current and field diffusion into an azimuthally and axially symmetric pinch are Faraday's, Ampere's and Ohm's Laws, which are, respectively:

$$\frac{\partial B}{\partial t} = c \frac{\partial E}{\partial r} \tag{4}$$

$$j = \frac{c}{4\pi r} \frac{\partial}{\partial r} (rB) \tag{5}$$

$$j = \sigma \left(E + \frac{v}{c} B \right), \tag{6}$$

where in this system E and j are in the \hat{z} direction, v is in the \hat{r} direction and B is in the $\hat{\phi}$ (azimuthal) direction; σ denotes the conductivity perpendicular to the magnetic field. (Displacement current could be important on very short timescales, but is generally ignored when the conductivity is large). These relations can be combined to give diffusion equations for E and B; the latter one, for example, is

$$\frac{\partial B}{\partial t} = \frac{c}{4\pi\sigma} \frac{\partial}{\partial r} \left[\frac{1}{r} \frac{\partial}{\partial r} (rB) \right] - v \frac{\partial B}{\partial r}. \tag{7}$$

This is most conveniently solved in the comoving reference frame, where the last term is not present.

A variety of profiles, static and dynamic, can result from the diffusion equations. The static solution near the axis is $B \propto r$, which is the Bennett model of a uniform current density across the pinch; the electric field dominates near the axis, where $B \to 0$ but $E \neq 0$. When the current oscillates with frequency ω , the solution is well-known: the fields are confined to within a "skin depth" $\delta = c/\sqrt{2\pi\mu\omega\sigma}$ of the surface:

$$j = \begin{cases} j_0 e^{(r-R)/\delta} & (r \le R) \\ 0 & (r > R) \end{cases}$$
 (8)

where the susceptibility $\mu \sim 1$, and the conductivity is assumed constant throughout the plasma. This skin current model may apply to the z-pinch, for short timescales $\tau \sim \omega^{-1}$, but the nonperiodicity of the z-pinch system means a much greater role for boundary conditions in determining the current dynamics. Whatever the actual current distribution in the z-pinch, the skin-current model illustrates the role of conductivity in a typical system: a smaller conductivity enhances the electric field strength relative to the magnetic field at each point in the plasma, as is shown below.

The magnetic field profile for a skin current can be easily found:

$$B(r) = \begin{cases} \frac{4\pi j_0}{c} \delta e^{(r-R)/\delta} \left[\frac{r/\delta - 1 + e^{-r/\delta}}{r/\delta} \right] & (r \le R) \\ \frac{RB(R)}{r} & (r > R) \end{cases}$$
(9)

Near the axis, B(r) depends linearly on r. The ratio of magnetic to electric field inside the wire is

$$\frac{B(r)}{E(r)} = \frac{4\pi\sigma\delta}{c} \left[\frac{r/\delta - 1 + e^{-r/\delta}}{r/\delta} \right]. \tag{10}$$

This is roughly proportional to $\sqrt{\sigma}$: a greater conductivity results in a stronger magnetic field in the current region, implying a smaller tendency for a peaked or directional electron distribution. A greater resistivity, on the other hand, would result in a relatively large electric field, and a greater possibility of runaway generation. Note that both with high and low conductivities it is possible to obtain significant high-energy electron production, but the electric fields required would be smaller for the low-conductivity case.

Motivated by the evident influence of the conductivity on field diffusion, we numerically investigated the direct effect of enhanced plasma conductivity on runaway electron production. The procedure was to first obtain time histories of the positions, temperatures and densities of an imploding z-pinch. These were obtained from a 1D MHD z-pinch simulation, and included the fluid velocity and transverse resistivity as a function of radius as well as the electric and magnetic fields on the pinch border. The diffusion equation for the fields was then solved, using the Spitzer resistivity used in the MHD model and also two sharply higher values of the resistivity. The resulting electric and magnetic field spatial profiles just before stagnation were then used as input to a time-dependent Fokker-Planck code to determine if they gave rise to enhanced-tail or depleted-tail electron energy distributions.

The results of this investigation can be seen in figs. (1-5). The three, progressively higher, resistivity profiles can be seen in fig. (1) (the Spitzer value is the lowest); the diffused electric and magnetic fields resulting from each of these sets of resistivities are shown in fig. (2) and fig. (3), respectively. Fig. (4) shows the consequent time-evolution of the electron distribution function for the lowest, Spitzer resistivity, while fig. (5) shows the same for the highest of the three resistivities. Plotted is not the actual distribution function, but the ratio of this with a same-temperature Maxwellian. In both of these figures, the distribution is shown at three locations;

each plot corresponds to a different radial position, with the three curves on each plot depicting the electron energy distribution at that position at different times as it evolves.

These results show that the "low", Spitzer resistivity results in greater enhancement of intermediate-energy electrons towards the edge of the pinch than the augmented resistivity (compare fig. (4b) and fig. (4c) with fig. (5b) and fig. (5c)); at these positions, however, the high magnetic field constrains these enhancements and, equally importantly, prevents the electrons from acquiring significant directionality. The augmented-resistivity diffusion produces much larger enhancements in high-energy electron populations on axis, (compare fig. (4a) with fig. (5a)), where the small magnetic fields focus the heating towards high enerhies and permit the formation of highly-directional electron beams. In short, this study showed that increased plasma resistivity would allow a significant electric field to penetrate to the pinch axis without the runaway-inhibiting effects of a strong magnetic field. Thus, an "anomalously high" resistivity could possibly underlie the theoretical description of the observed pinch runaways.

ANOMALOUS RESISTIVITY AND TURBULENCE

A likely cause for the indicated anomalously-high resistivity in the pinch is plasma turbulence. Turbulence results from interaction between particles (electrons) and the oscillatory modes of the plasma system, interaction that is particularly strong when the particle velocity is close to the phase velocity of the waves. In the turbulent z-pinch plasma, energetic electrons lose energy by generating plasma waves, and a large amount of wave energy builds up in the fluctuations of the system. The particles act as if they are scattered from the waves, and this new resistive process increases the resistivity over the Spitzer value.

Turbulent resistivity is nonlinear, and can grow rapidly when there is an energetic imbalance in the system, for example when two nearly monoenergetic beams intersect each other (Buneman instability). Because turbulence-generated anomalous resistivity is dynamical, it cannot be adequately represented as an additive or multiplicative term augmenting the equilibrium (Spitzer) resistivity. Energetic electrons excite all possible modes as they transit the plasma; the excited modes are both longitudinal and transverse, and large contributions to turbulence by obliquely directed modes may require an additional dimension in the analysis. The plasma modes important in particle turbulence usually have relatively slow phase velocity; the very important ion-acoustic

mode is the best example of this. Table 1 lists the most important candidates of turbulent modes in the z-pinch.

Table 1: Possible Instabilities [14]

Instability	Threshold	Frequency	Growth Rate
Buneman	$v_{drift} > v_e$	ω_{pi}	ω_{pi}
Ion-acoustic	$c_s < v_{drift} < v_e$	$<\omega_{pi}$	$(v_{drift}/v_e)\omega_{pi}$
Magnetized ion-acoustic	$c_s < v_{drift} < v_e$	ω_{LH}	ω_{LH}
Electron-cyclotron drift	$v_{drift} < v_e$	$\ell\omega_{ce}$	$(v_{drift}/v_e)\!\omega_{ce}$
Lower-hybrid drift	$v_{drift} < v_i$	ω_{LH}	ω_{LH}

Other research has shown that plasma turbulence can dominate the plasma resistance in PRS devices. For example, current conduction in the theta-pinch system has been extensively studied and the effects of turbulence in broadening the current sheath, decreasing the current penetration time, and distorting the electron distribution functions have been well documented [11], both theoretically and experimentally. Most important in the theta pinch are the ion-acoustic, Buneman (two-stream) and lower-hybrid instabilities. An important role for turbulence has also been established in lower-density systems, like the vacuum spark and the plasma opening switch.

Modeling of hot, dense z-pinch systems has been hitherto distinguished by detailed radiation transport[12], but only rudimentary particle dynamics. Only a few exploratory studies of turbulent effects in z-pinch plasmas have appeared in the literature [13], though slightly more work has been reported on the similar plasma focus device [14]. In the relatively high-density z-pinch system, turbulence would probably be most effective near the edge of the pinch or in a blowoff corona,

and in establishing the boundary conditions that determine the field penetration parameters into the pinch. The linear character of a z-pinch, which tends to promote electron runaway (unlike the theta pinch), may also promote other instabilities, such as those involving of synchrotron radiation and the Doppler resonance, and enhancements in the distribution function tail might excite the "bump-on-tail" instability[15]. In the z-pinch the collisional effects that have been ignored in other turbulent systems must be considered, and the parameter regime where collisional and turbulent resistance are comparable could be an important one in z-pinch dynamics.

We have already studied the dynamics of a z-pinch corona with turbulence-limited conductivity [16], and have found the corona to be an extremely effective carrier of current, with plasma conditions radically different from those in the bulk of the pinch. The major limitation of that work was the lack of a good model of energy transfer between the corona and the bulk of the pinch, which led to an unrealistically rapid heating of the corona. Other simplifications in the model, such as the force balance in the corona, should also be investigated in more detail.

QUASILINEAR THEORY

The quasilinear theory commonly used to describe turbulent resistivity can be incorporated very naturally into the Fokker-Planck equation which has earlier been formulated and solved by us [5]. This is now shown.

Turbulence is effectively an increase in fluctuations of the system over the small levels found in thermal equilibrium. These fluctuatuations are space and time-dependent variations which persist because of the collective properties of the system. To evaluate the magnitude of these fluctuations and their influence on the average distribution we separate the actual electron distribution function f(x,v,t) into an average term $F(v,t) \equiv \langle f(x,v,t) \rangle$ and a fluctuating term $\delta f(x,v,t)$:

$$f(x,v,t) \equiv nF(v,t) + \delta f(x,v,t). \tag{11}$$

A similar procedure is carried out for all other variables, such as the particle acceleration $\vec{a} \equiv e\vec{E}/m + (e/mc)\vec{v} \times \vec{B}$.

With these definitions the spatial (ensemble) average of the Vlasov equation for f(x, v, t)

is

$$\frac{\partial F}{\partial t} + \langle \vec{a} \rangle \cdot \vec{\nabla}_{v} F = -\frac{1}{n} \left\langle \delta \vec{a} \cdot \vec{\nabla}_{v} \delta f \right\rangle. \tag{12}$$

The average distribution F(v,t) is influenced by the product of the density fluctuations and the field fluctuations through the term on the right-hand side. Because of this nonlinear term the theory is not linear, but "quasilinear".

Subtracting the averaged equation from the full Vlasov equation gives an equation for the fluctuations:

$$\left[\frac{\partial}{\partial t} + \vec{v} \cdot \vec{\nabla} + \langle \vec{a} \rangle \cdot \vec{\nabla}_{v}\right] \delta f + \delta \vec{a} \cdot \vec{\nabla}_{v} f = -\delta \vec{a} \cdot \vec{\nabla}_{v} \delta f + \langle \delta \vec{a} \cdot \vec{\nabla}_{v} \delta f \rangle$$
(13)

This equation is linearized by setting the right-hand side to zero. This is consistent with keeping the nonlinear term in the average equation because, it can be argued, the terms neglected here are third-order. The linearized equation is identical to that obtained by linearizing the Vlasov equation, and there is such an equation for each type of particle α in the system (the simplest system has just electrons and ions). Solutions to this equation can be found by Fourier transforming the perturbing distribution δf ; the frequency and wave number of the resulting solution satisfy the dispersion relation

$$1 + \sum_{\alpha} \frac{4\pi q_{\alpha}^2}{m_{\alpha} k^2} \int \frac{\vec{k} \cdot \vec{\nabla} F_{\alpha}}{\omega - \vec{k} \cdot \vec{v}} d^3 v = 0$$
 (14)

where the sum is over all particle species α (with charge q_{α} and mass m_{α}) in the system.

If only electrostatic perturbations are considered, then the density fluctuations represented by δf are directly proportional to the electric field fluctuations δE that are solely responsible for δa . The quasilinear term $\left\langle \delta \vec{a} \cdot \vec{\nabla}_v \delta f \right\rangle$ can then be written in the same form as the Fokker-Planck electron-electron collision term, so that

$$\frac{\partial f}{\partial t} + \langle \vec{a} \rangle \cdot \vec{\nabla}_{v} f = \frac{\partial}{\partial v} \left[D_{ij} \frac{\partial f}{\partial v} \right], \tag{15}$$

where

$$D_{ij} = \frac{8\pi^2 q^2}{m^2} \int \frac{k_i k_j}{k^2} \mathcal{E}(k) \delta(\omega(k) - \vec{k} \cdot \vec{v}) d^3k$$
 (16)

is the turbulent diffusion tensor, and $\int \mathcal{E}(k) dk \equiv \langle \delta E^2/8\pi \rangle$ is the average electrostatic energy of the fluctuations. In following the evolution of the turbulent system, the increase in the magnitude

of \mathcal{E} is also followed; this tells what fraction of the system energy is in the fluctuating fields. Modification of the pinch radiation due to these fluctuating fields should provide a diagnostic test of the quasi-linear model. The study of radiation from such turbulent systems is a rapidly developing specialty [17].

These equations can now be incorporated into the numerically-solved Fokker-Planck equation [5] by first solving the dispersion relation to get $\omega(k)$ for the mode of interest and then evaluating the diffusion tensor $D_{\alpha\beta}$ for this mode. The process can be very time-consuming and an analytical study is being made to identify the important modes and parameter ranges so that the process can be as focused and so as economical as possible.

CONCLUSIONS

- 1. The effects of electric and magnetic fields on electron dynamics have been summarized:
 - Electric fields heat the electrons, but the heating depends on $(E/B)^2$, not E^2 , at high magnetic fields.
 - The magnetic field strength determines which electron population is most affected by ohmic heating.
 - Strong magnetic fields isotropize the electrons and prevent runaways from forming.
 - Runaway electrons require strong electric fields with not-too-strong magnetic fields.
- 2. Electric and magnetic field profiles predicted by MHD simulations do not predict adequate runaway electron production. This is probably because those models use a too-low (Spitzer) electrical resistivity.
 - Experimental resistivity measurements are higher than Spitzer values.
 - Higher resistivity promotes increased electric fields in low-magnetic-field regions (on the pinch axis).
- 3. Increasing the pinch resistivity promotes runaway production.
 - Simulations with artificially increased resistivity have greater on-axis tail enhancement, anisotropy.

- 4. Anomalous resistivity is probably due to turbulence.
 - Turbulence is well-studied in other systems, but hitherto ignored in z-pinch.
 - Turbulent regions determine boundary conditions of the pinch, develop electric properties of pinch plasma (see fig. (6)).
 - Z-pinch system is unique in being highly-collisional, straight-line system.
 - An appropriate quasi-linear model is developed with simple connections to earlier kinetic investigations of collisional, ohmically-heated z-pinch electrons.
- 5. Questions to be addressed in the coming year include:
 - What are the important plasma micro-instabilities influencing self-consistent current flow?
 - Can current-generated plasma instabilities generate enough anomalous resistivity to explain experimental current sheath, radiation, pulse duration and output measurements?
 - What is the mechanism and speed of current and field penetration in theturbulent z-pinch? How important are boundary conditions and state variables?
 - To what extent do micro-instabilities give rise to configuration- space instabilities in hot dense plasmas? Specifically, can the enhanced field diffusion resulting from turbulence generate a strong enough electron beam to explain "bright spots" a z-pinch implosion?

References

- 1. M. Krishnan, "PRS A critical assessment," Physics International Company Report PITR 3992-01 (1989).
- 2. C. Deeney, private communication.
- 3. B.A. Trubnikov, "Particle acceleration and neutron production at the necks of plasma pinches," Sov. J. Plasma Phys. 12:271 (1986).
- 4. B.A. Trubnikov and S.K. Zhdanov, "Particle acceleration by breaking the constrictions of a z-pinch and a plasma focus," Sov. Phys.-JETP 43:48 (1976).
- 5. P.E. Pulsifer and K.G. Whitney, "Non-Maxwellian electron distribution functions in z-pinch plasmas," NRL Memorandum Report 6662 (1990).

- 6. P.E. Pulsifer, K.G. Whitney and J.E. Thornhill, "Electron thermalization and runaway production in a titanium z-pinch," Bull. Am. Phys. Soc. 33:1909 (1988).
- 7. H. Dreicer, "Electron and ion runaway in a fully ionized gas," Phys. Rev. 115:23 (1959).
- 8. NRL Plasma Radiation Branch, "Advanced concepts theory annual report 1988," NRL Memorandum Report 6517 (1989), pp. 37-66.
- 9. J.M. Grossmann, P.F. Ottinger and R.J. Mason, "Current channel migration and magnetic field penetration in a perfectly conducting plasma with emitting, conducting boundaries," J. Appl. Phys. 66:2307 (1989).
- 10. P.H.Y. Lee, J.F. Benage, Jr. and R.D. Fulton, "Nonlinear diffusion of mega-Oersted fields or megaampere currents into conductors," Bull. Am. Phys. Assoc. 35:1965 (1990); J.F. Benage, Jr., R.R. Bartsch, J.C. Cochrane, R.D. Fulton, H.W. Kruse, P.H.Y. Lee, J.V. Parker and D.L. Weiss, "Measurement of megaampere current diffusion into copper," Bull. Am. Phys. Assoc. 35:1965 (1990).
- 11. R.C. Davidson and N.A. Krall, "Anomalous transport in high-temperature plasmas with applications to solenoidal fusion systems," Nucl. Fusion 17:1313 (1977).
- 12. D. Duston and J. Davis, "Line emission from hot, dense aluminum plasmas," Phys. Rev. A21:1664 (1980); D. Duston and J. Davis, "Usefulness pf x-ray diagnostics in dense-plasma gradients," Phys. Rev. A24:1505 (1981).
- 13. A.E. Robson, "Anomalous resistivity and the Pease-Braginskii current in a z-pinch," Phys. Rev. Lett. 63:2816 (1989).
- 14. V.V. Vikhrev and V.M. Korzhavin, "Effect of anomalous conductivity on the dynamics of the plasma focus," Sov. J. Plasma Phys. 4:411 (1978).
- 15. E. Moghaddam-Taaheri and L. Vlahos, "Synchrotron radiation from dynamically evolving runaway tails," Phys. Fluids 31:99 (1988); V. Fuchs, M. Shoucri, J. Teichmann and A. Bers, "Runaway electron distributions and their stability with respect to the anomalous Doppler resonance," Phys. Fluids 31:2221 (1988).
- 16. NRL Radiation Hydrodynamics Branch, "Advanced concepts theory annual report 1989," NRL Memorandum Report 6612 (1990), pp. 80-99.
- 17. F. Rogers and H. deWitt, eds., Strongly Coupled Plasma Physics, Plenum Press (1987).

Figure Captions

- Figure 1. Plasma resistivity, in ohm-cm, as a function of radius for an aluminum implosion. Data was taken from an MHD simulation at a time just before stagnation of the pinch. The three curves correspond to the Spitzer value from the simulation (curve A), four times the Spitzer value (curve B), and sixteen times the Spitzer value (curve C).
- Figure 2. Electric field as a function of radius, as a result of diffusion into the pinch with the different resistivities from fig. (1).
- Figure 3. Magnetic field as a function of radius, as a result of diffusion into the pinch with the different resistivities from fig. (1).
- Figure 4. Time-development of the electron energy distribution function under the influence of the fields of fig. (2) and fig. (3), for the plasma decribed in fig. (1). Here are shown the results for the Spitzer resistivity (curve A in fig. (1)). Fig. (4a) plots the distribution near the axis; fig. (4b) plots the distribution midway between axis and edge; and fig. (4c) plots the distribution at the pinch edge. Curve A, B and C in each plot give the distribution after one, 10 and 20 electron-electron collision times, respectively.
- Figure 5. Time-development of the electron energy distribution function under the influence of the fields of fig. (2) and fig. (3), for the plasma decribed in fig. (1). Here are shown the results for 16 times greater than the Spitzer resistivity (curve C in fig. (1)). Fig. (5a) plots the distribution near the axis; fig. (5b) plots the distribution midway between axis and edge; and fig. (5c) plots the distribution at the pinch edge. Curve A, B and C in each plot give the distribution after one, 10 and 20 electron-electron collision times, respectively.
- Figure 6. A schematic picture of the model z-pinch, showing possible effects of turbulence in each region.

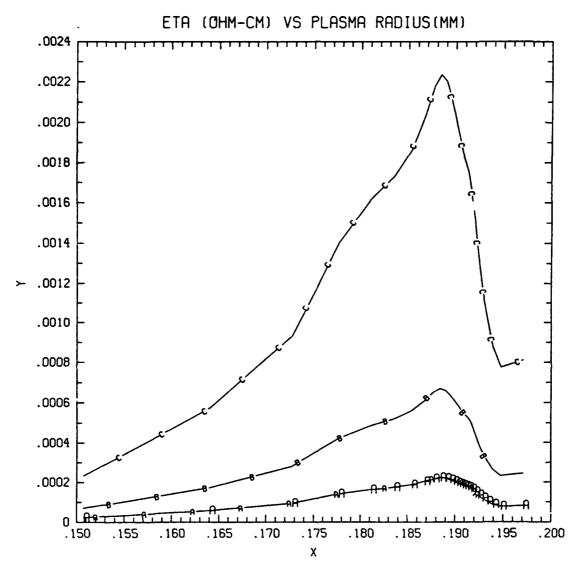


Figure 1

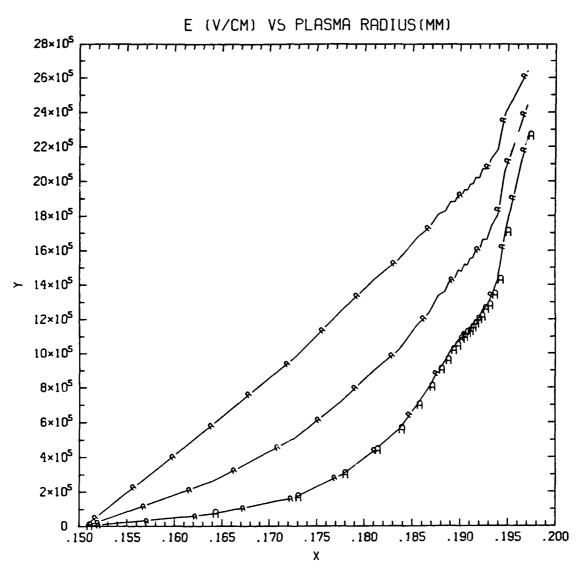


Figure 2

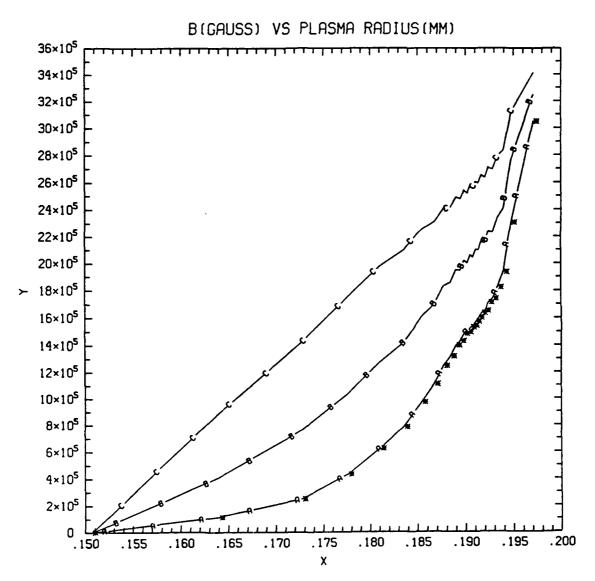
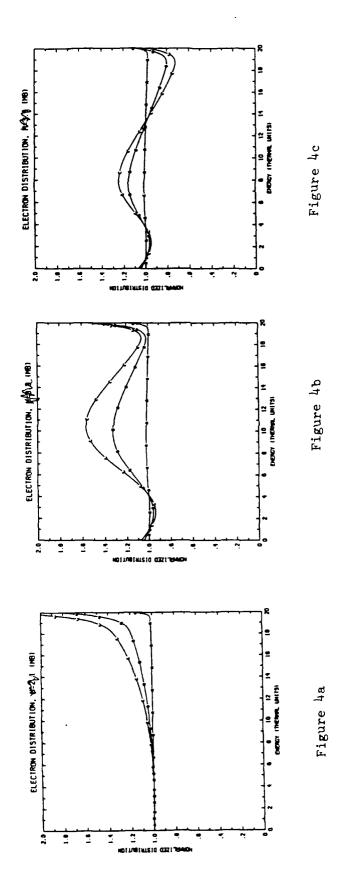


Figure 3



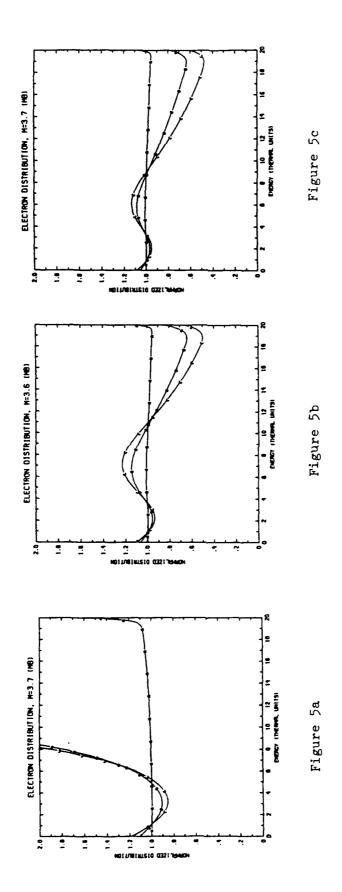


Figure 6

VII. 2-D FLUID MODELING OF KINETIC ENERGY GENERATION

During the past fiscal year, code 4720 has begun to look at the dynamics of imploding array Z-pinches from the perspective of two-dimensional radiation hydrodynamics. This follows naturally from our previous work on the dynamics of X-pinch implosions that was reported on in the previous final report. However, there are significant differences in the modeling of these two types of loads. The motion of an X-pinch is primarily along the z-direction with limited expansion and contraction in the radial direction. The motion of an imploding gas-puff, or wire array, is quite different since there is considerable runin It is during this runin phase that the before the implosion occurs on axis. pinch plasma is accelerated and is most susceptible to instabilities. This unstable region occurs along the backside of the pinch where the density and magnetic pressure gradients are in opposite directions. Although this region can be quite narrow and limited to only a small region near the back of the pinch, the instability may grow at a rapid enough rate so that the imploding shell of plasma is disrupted before arriving on axis.

Unfortunately, these simulations present a more difficult problem from a numerical standpoint when comparing against the modeling of an X-pinch. In the X-pinch problem, one can choose an appropriate mesh and leave that mesh fixed during the simulation. In our X-pinch simulations we advanced the mesh in a Lagrangian fashion each cycle, and then remapped back to the original rectangular mesh so that the calculation was effectively Eulerian. This prevents the mesh from becoming tangled in the manner which often characterizes multi-dimensional This technique does not work nearly as well in Lagrangian calculations. implosion problems where the aspect ratio of pinch radius to the thickness of the plasma shell is large. In this case, a mesh which remains fixed in time would result in the shell being resolved by only a few zones. The region over which one could expect instability activity would have even less resolution. A failure to have resolution in this region would result in a distortion of the instability and consequently, the underlying physics would also become distorted. In order to correct for this problem we have employed a method which moves the mesh with the imploding shell. Initially, a high percentage of the total number of zones is placed in the shell mass. As the shell implodes towards the axis, the radial mesh velocity is calculated according to an average (or, mass averaged) velocity along the axial nodes at each radial node. Usually, there is compression prior

to the acceleration or, runin, phase as mass is picked up and a narrow, high density shell is formed. The mesh also becomes compressed during this process so that it is necessary to include an artificial viscosity similar to that which is commonly employed in a Lagrangian calculation. If there is no instability activity along z, the average velocity will be the velocity of the plasma shell and the calculation will indeed be Lagrangian. On the other hand, if the backside is unstable, the average velocity at which the remapping takes place will cause the mesh to be less compressed in this region and will automatically accommodate the larger region necessary to model this activity.

We have found that this method works quite well for the imploding shells of current driven Z-pinch plasmas of interest to PRS applications. An example is shown in Figs. 1-4 which display density contours using an asinh (arc hyperbolic sine) scale that is linear near the maximum value of the density. The contours become more logarithmic as the ratio of peak density divided by the density becomes large. Plot times are given in nsec. At implosion, the peak density is $1.85 \times 10^{-1} \text{ gm/cm}^3$. The plasma shell is initially uniform with an inner radius of 0.7 cm and an outer radius of 0.8 cm. The length of the computational box is 0.8 cm in the z-direction. The linear mass density was chosen to be 500 µgm/cm and the driving current was chosen to correspond to that of the Saturn accelerator at Sandia National Laboratory ($dI/dt = 2.5 \times 10^{14} \text{ Amps/sec}$ for 40 nsec). The initial density perturbation was chosen to be random at a level of 10 percent over the inner portion of the plasma shell. For numerical reasons, the outside portion of the shell was left unperturbed. The first plot, at 30 nsec, shows the contours just after the inward acceleration has begun. The unstable activity is evident on the backside. At 44 nsec, the shell shows both large and small scale distortions. The large gradient on the backside is evident in the closely spaced contours. Peak compression occurs at 52 nsec. Although the density on axis shows variations along the z-direction, the overall appearance seems to be relatively uniform. The final contour plot at 64 nsec shows the bounce or expansion after implosion.

The set of equations used in the 2-D model are:

$$\frac{d\rho}{dt} = -\rho \vec{\nabla} \cdot \vec{u} \tag{1}$$

$$\rho \frac{d\vec{u}}{dt} = -\vec{\nabla}(P_e + P_i + Q_a) + (\vec{J}x\vec{B})/c , \qquad (2)$$

$$\frac{d\varepsilon_{e}}{dt} + P_{e} \frac{dV}{dt} = -V\vec{v}.\vec{q}_{e} + V\eta J^{2} + P_{rad} + VC_{ei} (T_{i} - T_{e}), \qquad (3)$$

$$\frac{d\varepsilon_{i}}{dt} + (P_{i} + Q_{a}) \frac{dV}{dt} = -V\vec{V}.\vec{q}_{i} + VC_{ei} (T_{e} - T_{i}). \tag{4}$$

To these equations are added Maxwell's equations, viz.,

$$\vec{\nabla} \times \vec{B} = 4\pi \vec{J}/c \tag{5}$$

$$\vec{\nabla} \times \vec{E} = -\frac{1}{c} \frac{\partial \vec{B}}{\partial t}$$
 (6)

along with Ohm's law,

$$\vec{E} = \eta \vec{J} - (\vec{u} \times \vec{B})/c \tag{7}$$

In Eqs. (1) - (7) $P_{e,i}$ are the material pressures for electrons and ions, $\varepsilon_{e,i}$ are the specific energies, ρ is the density, V is the inverse of the density, $\vec{q}_{e,i}$ are the heat fluxes, $C_{e,i}$ is the electron-ion energy exchange term, and ηJ^2 is the ohmic heating. The P_{rad} term in Eq. (3) is the radiation source or sink term. In Eqs. (3) and (4), Q_a is an artificial viscosity used for numerical stability in regions of strong compression.

In the future, we will use these studies to concentrate on several important issues which are relevant to understanding PRS loads. First, how much of the mass of the original load actually implodes on axis? It is apparent form the figures that in the process of disrupting the implosion, some mass is left behind. When radiation is added to this type of calculation, it is obviously important to know how the unstable activity affects the output of the implosion in terms of both total and K-shell radiation. It is equally important to understand how such activity modifies the width of the radiation pulse. Other important questions are: (1) How does the unstable activity affect current penetration and hence, acceleration of the plasma shell? (2) When does the instability begin to grow and how is this sensitive to the acceleration of the plasma shell? Does a modification in the current risetime affect this growth and is there an optimum risetime which introduces the least amount of damage to an imploding load? (3) Finally, what is the length scale of the instability? Does it match the thickness of the shell and thus destructive to the integrity of the shell? If the length scale is shorter than the shell thickness, then the instability will be confined to the outside region and the majority of the mass may implode relatively intact.

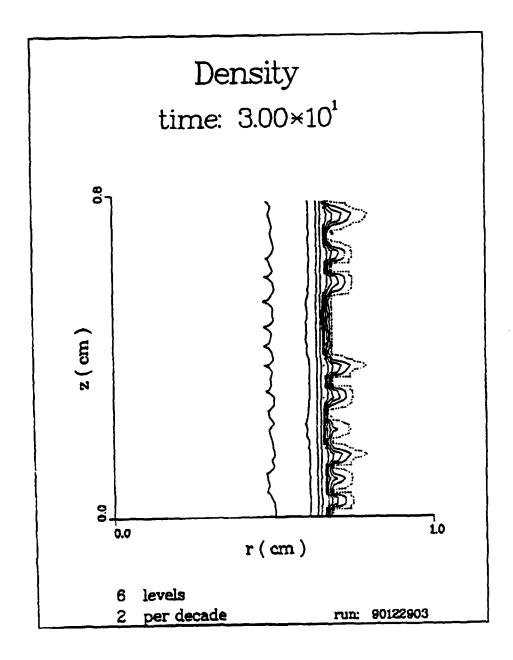


Figure 1. Density contours at 30 nsec.

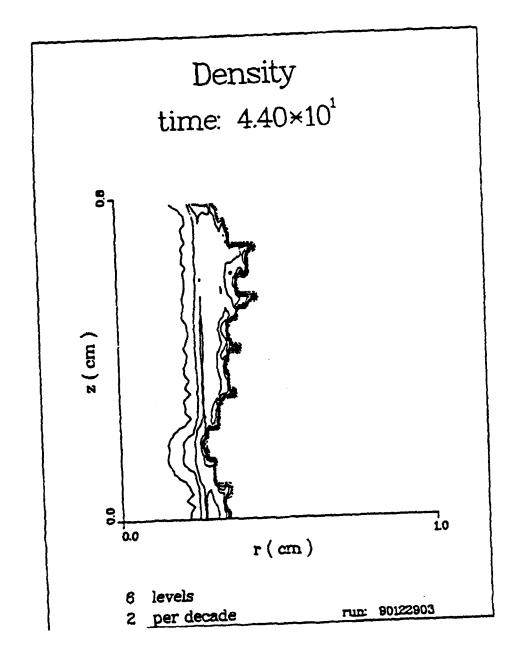


Figure 2. Density contours at 44 nsec.

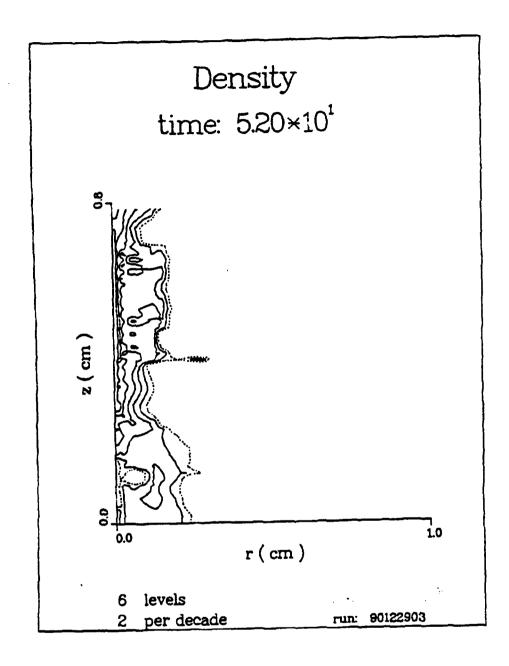


Figure 3. Density contours at peak compression (52 nsec).

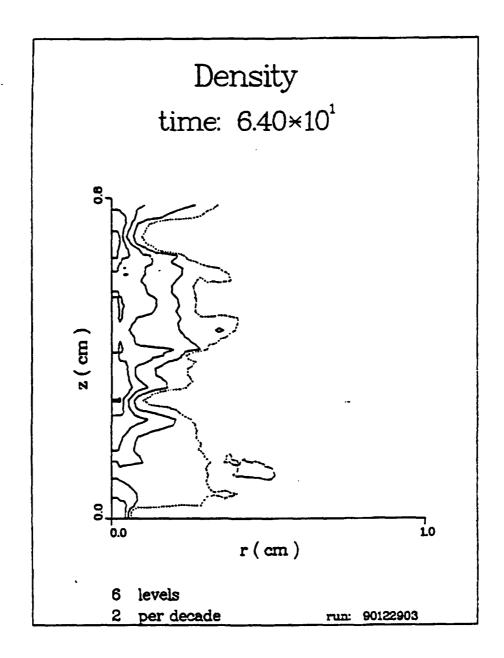


Figure 4. Density contours at 64 nsec.

Introduction

The great radiative efficiency of one dimensional PRS models in converting implosion kinetic energy to heat and (k-shell) light leads naturally to the attempted stabilization of these pinches and modern stability theory provides some guidance suggesting that such stability depends upon the radial profile of the axial flow. There is no shortage of data indicating that both m=0 and m=1 motions are present in PRS loads, but the most disruptive of these is the "sausage" mode. The general strategy in sausage stabilization is to provide an axial magnetic field component which cannot be "sidestepped" by the plasma through an interchange of field and fluid, nor can the axial field be as easily compressed - it builds "backpressure" with an r^{-3} scaling as compared with the r^{-1} scaling of the pure z-pinch stress. The next order of refinement of this basic idea involves the details of the magnetic shear profile in the load, for in the simplest limit it is not so much the absolute magnitude of the axial field as the rapidity of spatial change in the "safety factor" which stabilizes things. The next order of refinement involves balancing the radial shear of the axial flow, associated with gas or metal vapor puff annular loads, to enhance the load stablity. If one can find a practical, effective balance of flow and axial or azimuthal magnetic fields, there will result a close laboratory approximation to the idealized one-dimensional implosion process and a wider variety of load options, probably more forgiving in design tolerances, becomes accessible.

The blend of z and θ pinch field sets (respectively, the TM and TE modes) into a helical magnetic field has been explored extensively in the CTR community. For fusion devices global stability is essentially the only issue and perturbations must be damped on very long timescales compared to the PRS problem. In contrast, for a modern pulseline driver, the stability is needed for 100 ns timescales only and the load can be annular for much of the rundown. Since the annular load has the advantage of avoiding any substantial backpressure, it is (at least marginally)

stable until the stagnation and compression phase wherein the timescales are futher reduced to 10 ns. Since the energy coupling efficiency between pulseline and load is improved with a greater dynamic range in load inductance during the rundown, the ability to achieve a stable compression over several centimeters of radius using a screw pinch load would be extremely beneficial to the PRS effort in general.

The screw pinch could therefore be an attractive PRS load if (i) it achieves a reasonable measure of stability against m=0 deformations, (ii) it can maintain good power coupling to modern generators, and (iii) these things can be achieved with little or no loss in radiative efficiency. The question we wish to treat here can be addressed through our 0-d ideal MHD fluid model equipped with an appropriate equation of state, the global stability of various initial shear profiles in axial field and axial flow can then be explored with modest effort.

Until recently, the local stability criterion due to Suydam, as generalized to a screw pinch by Hameiri³, was the most general applicable test. It is now established that global modes can exist in a screw pinch under some conditions, and the assessment of stability on any 1-D set of plasma profiles now rests on several distinct tests, following Bondeson^{4,5}, et.al.

There is one local criterion (generalizing Hameiri's result), in either the magnetohydrodynamic (MHD) or guiding center plasma (GCP) limit. Bondeson finds in the absence of axial or azimuthal flow that the "modified Suydam" spectrum is stable at $any r_o$ unless

$$-\frac{2p'}{rB_z^2(\frac{\mu'}{\mu})^2} > \frac{1}{4} .$$

Such a local criterion is not sufficient for stability in the ideal MHD limit for there global modes can arise. These modes are stabilized in the GCP limit but, if one has an MHD profile such that $S(r_o) = (B^2 - \gamma P)\rho\tilde{\omega}^2 - \gamma P(k \cdot B)^2 = 0$ anywhere, then the "global slow modes" are unstable if

$$D_S(\frac{v_S}{v_A}, S'', B, B', k \cdot B, k) > \frac{1}{4} .$$

Alternately, if one has a MHD profile such that $A(r_o) = \rho \tilde{\omega}^2 - (k \cdot B)^2 = 0$ anywhere,

then the "global Alfven modes" are unstable if

$$D_A(\frac{v_S}{v_A}, A'', B, B'_z, B'_{\theta}, k \cdot B) > \frac{1}{4}$$
.

In these expressions $\tilde{\omega}$ is the local Doppler shifted frequency, $\tilde{\omega} = \omega + mv_{\theta}/r - kv_z$, γ is the adiabatic index, while μ is the winding number (it's derivative is the magnetic shear). It is related to the usual "safety factor" by $qR = \mu^{-1} = B_{\theta}/rB_z$. The expressions D_A and D_S are complicated functions of the arguments listed, which we do not need to examine here. Those modifications are quite important in the MHD limit, however, and will be included below as the model develops.

In the next section we review some variations on well-known self-similar MHD flows which admit (i) a basic set of benchmark problems and (ii) a very straightforward (0-d) "gas bag" model that in turn allows us to simulate existing screw pinch load schemes.

In the final section we discuss the detail results with the "gas bag" model and examine the implied options for achieving stable operation.

Model Formulation

The self-similar implosions used heretofore as benchmarks have a second application as generic pinch models. The utility of such models is clearly limited to the identification of trade-offs in load mass, initial position and the like; the caveats associated with their application are numerous. In PRS theory, whenever such a model is used, we are implicitly saying that either (i) the detailed profiles of the 0-d model are really accessible, or (ii) some interior dissipative process acts to make such profiles emerge, or (iii) they represent some radially averaged load state. Here a mix of all these limits is contained in the model.

Are these special profiles in any sense accessible to the load? Plasma viscosity could play a role in producing and maintaining self-similar states if it is both non-local (characterized by a mean relaxation time $\tilde{\tau}$) and much stronger than classical small angle collisions would predict. Clearly the current programming path to homogeneous compressions is not general enough to be a dominant process, so some

dissipative mechanism would be required. A second ingredient of homogeneous compressions is an isothermal temperature profile. In the loosely defined "gray body" limit, viz. sufficient opacity to make the radiative cooling profile peak near the surface, the interior radiative exchange of energy is usually very effective at keeping the temperature constant over the bulk of the pinch. This implies that ohmic heating, if included, can be done in a spatially averaged sense without accounting for the detailed (and nonuniform) current profiles implied by the self-similar motion – only form factors of $\mathcal{O}(1)$ would modify the resistance in that case. The Gaussian density profile is surely not the only one likely to emerge from the closure of an annular PRS load, but it does resemble the density profiles obtained in 1-d calculations. So, in a very approximate sense, PRS loads can be imagined which are not very different from the ideally self-similar ones.

On the other hand, even when the special profiles are not "launched at t_o ", the resulting ODE for \dot{U} possesses the proper scalings with radius (α) for all the separate components of the stress – pressure (ν_S^2) , axial magnetic field pushing in or out $(\nu_{B_x}^2)$, azimuthal magnetic field $(\nu_{B_\theta}^2)$, and viscosity $(\tilde{\tau})$. If instead of separating the momentum equation and solving for profiles, we had spatially integrated the separate stress components and used the average values to assign a strength to each of the separation constants, the result would have been the same. In other words, profiles in r_o which differ from the special self-similar ones would simply produce slightly different values of the (arbitrary) separation constants if averaged over some spatial domain. The details of such form factors are hopefully less important in the pinch dynamics than the radial scalings of each competing stress component, although certainly these details are not trivial. Only comparisons with full 1-d calculations can resolve the most salient of these differences but in the spirit of a "coarse grained" examination of screw pinches in modern pulselines one may state the "gas bag" model as follows.

The differential equaiton for the relative radial motion is

$$\dot{U}(\alpha) = r_o \left(\frac{2\nu_S^2}{\alpha} - \frac{i\nu_{B_z}^2 - ii\nu_{B_z}^2}{\alpha^3} - \frac{\nu_{B_{\theta}}^2}{\alpha} - \frac{\dot{\alpha}}{\alpha^2} \frac{2}{3} \tilde{\tau} \nu_S^2 \right)$$

with $\alpha = r(\tau)/r_o$, $\Theta_e = T_e + (\frac{2}{3})\frac{\epsilon_I}{2}$, and

$$\nu_S = \sqrt{(\mathcal{Z}+1)T(\Theta_e)/m_{ion}r_o^2} .$$

The axial magnetic frequencies are split into current dependent, compressing exterior (i) and initially fixed, retarding interior (ii) components; while the azimuthal magnetic frequency is related to a generalized Bennett current, viz.

$$_{i}
u_{B_{z}} = \frac{\pi N I(\tau)}{c\sqrt{\Upsilon}} \ , \ _{ii}
u_{B_{z}} = \sqrt{\frac{_{ii}B_{z}^{2}}{4\pi m_{ion}n_{o}r_{o}^{2}}} \ ,$$

and

$$\nu_{B_{\theta}} = \frac{I(\tau)}{r_o^2 \sqrt{\pi c^2 m_{ion} n_o}}.$$

The inductance and impedance can be shown to be

$$L = 1.8 \cdot 10^{21} l_p / c^2 \left(\ln \frac{r_w}{r} + \frac{1}{2} (r_w^2 - r^2) [2\pi N]^2 \right) [nH] ,$$

$$Z = Z_o - \left(\frac{\dot{r}}{r} + [2\pi N]^2 \dot{r}r \right) 1.8 \cdot 10^{12} l_p / c^2 [\Omega] ,$$

$$Z_o = 3.257 \cdot 10^{-6} (l_p / \pi r_o^2) \left(\frac{\Lambda}{10} \right) \frac{\mathcal{Z}}{\alpha^2 T_o^2} [\Omega] .$$

Here l_p is the pinch length, N is the return current winding number (per cm), and r_w is the radius of the return current cage. The factors Υ and n_o are the pinch mass per cm and mean ion density; for a strictly self-similar Gaussian they are related by $\Upsilon = m_{atom} n_o \pi r_o^2$. The heating equation can be written

$$\dot{\Theta}_{e} = -\frac{4}{3}\frac{\dot{\alpha}}{\alpha}T_{e}(\Theta) + \frac{8}{9}(\frac{\dot{\alpha}}{\alpha})^{2}\frac{1+\mathcal{Z}}{\mathcal{Z}}T_{e}(\Theta)\tilde{\tau} + Z_{po}\frac{I^{2}\mathcal{Z}}{\alpha^{2}T_{e}^{\frac{3}{2}}} - P_{rad},$$

where $Z_{po} = Z_o(1.0375733 \cdot 10^{-11} A/l_p \Upsilon)$ is the specific impedance (per ion).

Because of the strong radial scaling of the type *i* axial magnetic compression it is possible for this model to fall into a radiative collapse phase toward the end of an implosion cycle. In contrast to the more common notion of refrigerative collapse however, the compression here is driven from the exterior axial magnetic field and cannot terminate unless either the current is depleted from the pinch due to high terminal impedance or the equation of state changes rapidly to stiffen the radial scaling of the retarding pressure term.

For Argon at modest density the equation of state and radiation loss terms can be represented by rational functions of the total internal energy Θ_e , this allows a considerable saving of computation effort in the model. For example the branching ration can be represented by $B_{lo}(\Theta_e) = \frac{4.35-257.05\Theta_e}{1-51.69\Theta_e-674.77\Theta_e^2}$ and, $B_{hi}(\Theta_e) = \frac{1.72-46.27\Theta_e+203.81\Theta_e^2-601.91\Theta_e^3+305.84\Theta_e^4-295.29\Theta_e^5-34.18\Theta_e^6+1.85\Theta_e^7-0.036\Theta_e^8}{1-5.89\Theta_e-462.78\Theta_e^2+2589.74\Theta_e^3-5396.53\Theta_e^4+2963.45\Theta_e^5-1098.55\Theta_e^6},$ such that

$$B(\Theta_e) = B_{lo}(\Theta_e)$$
 for $\Theta_e < 0.096 keV$

$$B(\Theta_e) = Exp(B_{hi}(\Theta_e))$$
 for $\Theta_e > 0.096keV$.

Similar expressions are available to model the radiation loss terms and the overall "grayness" of the Argon source in order to effect a simple black body limit in the model. Fig. 1(a,b) shows the resulting curves for Ar at a central density of 10^{19} ions/cm³, and a mm range scale height for $0 < \Theta_e < 2.0 \text{ keV}$

Effects of Flow on Stability During Compression

The generalized Suydam criterion for the case of only axial flow is given by

$$S_{y}(r) = \frac{(1 - M^{2})}{8} \left(\frac{\mu'}{\mu}\right)^{2} r B_{z}^{2} + p' - \frac{2\beta M^{2}}{\beta - M^{2}} r^{-1} B_{\theta}^{2} . \tag{1}$$

where M measures the shear of the axial flow, and β measures the usual energy ratio, viz.

$$M^2 = \rho \left(\frac{v_z'}{B_z'}\right)^2 .$$

When the expressions for the self-similar adiabatic oscillator solutions are expanded out in this result the function becomes

$$S_{y} = \rho \left(\frac{16D_{\theta}I_{p}^{2}M\beta\pi}{I_{b}^{2}\alpha^{3}(M-\beta)\rho^{5}} + \frac{D_{z}(1-M)(\frac{\mu'}{\mu})^{2}\pi\left(\frac{\nu_{z0}}{\mu_{0}} + 4N_{wnd}^{2}\pi^{2}\right)}{\alpha^{5}} - \frac{2}{e^{\rho^{2}}\alpha^{\frac{18}{8}}} \right) ,$$

with the energy ratio

$$\beta = \frac{1}{1 + \frac{24\pi}{5}\alpha^{\frac{16}{3}} \left(\frac{I_p^2(e^{\rho^2} - \rho^2 - 1)}{I_b^2 \rho^2} + \frac{((e^{\rho^2} - 1)\epsilon_1 + \epsilon_2)\nu_{x0}}{\nu_0} \right)},$$

and the magnetic shear

$$\frac{\mu'}{\mu} = -\frac{\left(\epsilon_1 - \epsilon_2\right)\rho}{D_z e^{\rho^2}} + \frac{\frac{2\rho^2 + \rho^4 - 2}{e^{\rho^2}}}{D_{\theta}} ,$$

completing the description. In these relations several auxilliary variables are needed.

The functions

$$D_z = \left(1 - e^{-\rho^2}\right)\epsilon_1 + \frac{\epsilon_2}{e^{\rho^2}} ,$$

and,

$$D_{\theta} = \rho \left(1 - \frac{1 + \rho^2}{e^{\rho^2}} \right)$$

are form factors for the two field components. The ratios

$$\epsilon = \frac{\nu_0}{\nu_{z0}} (2\pi N_{wnd})^2 ,$$

$$\epsilon_1 = \frac{\epsilon I_p^2}{(1+\epsilon)\,I_b^2} \;,$$

and

$$\epsilon_2 = \frac{1}{1+\epsilon}$$

set the relative strengths of the two field components, while

$$M = \frac{\eta^2}{4e^{\rho^2}\pi}$$

sets the overall strength of the axial gas flow relative to the (axial) component of the Alfven speed. The radial variable ρ is relative to the initial scale radius, and time invariant, while all time dependence is confined to α .

Since the compression history is determined by the solution $\alpha(\tau)$ to the characteristic ODE for the model, one can examine the stability as a function of ρ , α and η to get a picture of the operating paths available. In Fig.2a the function $S_y(\rho, \eta, \alpha = 1)$ is plotted for a value of ϵ which provides a oscillatory motion for the pinch, while in Fig. 2b is a similar plot for a case which would represent a radiative collapse. In both cases the ability to increase the value of η (presumably) through axial field coil or nozzle design would enhance the radial domain of stability for the screw pinch load.

A straightforward inspection of the stability expression for adiabatic compression shows that in the absence of flow $(\eta \to 0)$ the compression could not alter the stability because the scaling with α favors the stabilizing term. In the case of axial flow the result is not so clear as can be seen in FIg. 3. Here the flow parameter is fixed to a normally stabilizing value (at $\alpha = 1$), then the compression is simulated by letting $\alpha \to 0$. Because of the scaling of β with α the pinch is brought again to an unstable configuration as it collapses. If the equation of state is modified to include the detailed branching ratio and ionization state, then the scaling with α is not available analytically. One alternative is then to use the 1-D code on the self similar problem and compute the stability function, as shown in Fig. 4. The different equation of state shows its effect in altering the location and extent of the domain in (ρ,α) space where the instability would onset.

References

- 1. R.E. Terry and F.L. Cochran, NRL Memo Rep. 6491, 1989, "Energy Transfer from High Power Pulselines to the Next Generation of PRS Loads"
- 2. F.L. Cochran and J. Davis, "Evolution of an X-pinch Plasma", submitted to PFB.
- 3. E. Hameiri, ERDA Report C00-3077-123, MF-85.
- 4. A. Bondeson, et. al., PF 30(7), 1987, p.2167.
- 5. A. Bondeson, et. al., PFB 1(7), 1989, p.1431.

IX. Electrostatic Turbulence in the Z-pinch Corona

Introduction

Earlier work^{6,7} with gyrokinetic descriptions of the Z-pinch corona was intended to study the propagation dynamics of radial TEM modes within a magnetically insulated transmission line using a moment equation formulation similar to that discussed below in regard to self-similar distributions. While the propagation problem is well posed from an electromagnetic viewpoint, the fluid description of the "collisionless" plasma provides a challenge in that, with no dissipative phenomena to spread the influence of rapid changes across some characteristic length, the problem tends to stagnate at an ever sharper shock front (in the ExB drift velocity) and thus provide answers which are both limited in validity and difficult to compute. The discovery of self-similar solutions for the meta equilibrium distribution function allowed some progress in understanding the energy transfer, but the constraints on such flows are severe and a more general basis for understanding the propagation of power through the corona is needed.

Any general study of collective phenomena which might form a basis for the expected dissipative processes must begin with the collisionless unperturbed distributions which constitute the metaequilibria available to the system. The general characteristics of such equilibria are set out in the following section. The following section develops the quasi-linear theory of electrostatic perturbations in the collective fields and distribution functions in the limit of free streaming ions and gyrokinetic electrons. Finally the general structure of unstable ion sound like electrostatic modes is mapped out in some detail and one can reach some conclusions as to the probable means of saturation – which will in turn determine the effective level of turbulence responsible for the dissipative processes.

Equilibrium Formulation

While the observables of the kinetic theory are always interrelated through the moment equations, those macroscopic quantities that enter into the moment equations are averages over the particle distribution function. The equilibrium distribution functions of interest here solve the gyrokinetic equation to arbitrary order in $\Omega \tau$ and contain a class of separable functions of the form g(r,t) $F(\mu,p_{\theta},r_0)$. Here, instead of writing the distribution in terms of the velocity components in cylindrical geometry, it is better to use the dynamical invariants, the magnetic moment μ and the angular momentum p_{θ} . The two equivalent representations of the gyroaveraged distribution function are connected by

$$f(r,v,t) = \left[\frac{m^2 r}{2\pi B(r,t)}\right] n(r,t) F(\mu,p_{\theta},r_0).$$
 (2)

The factor in [...] is the Jacobian of the transformation from v to μ , p_{θ} , and ϕ the gyrophase. Without collisions the invariants for each particle do not change, and the velocity function F is constant in time along a guiding center trajectory, $r(r_0, t)$. The particle density n(r,t) is no longer part of F, which is normalized as

$$\left[\frac{m^2 r_0}{2\pi B_0(r_0)}\right] \int d\mu dp_{\theta} F(\mu, p_{\theta}, r_0) = 1, \qquad (3)$$

for both electrons and ions. With the assumption of quasineutrality the mass density ρ is $\rho = (Zm_{elec} + m_{ion})n(r, t)$.

Without collisions the distribution function is not necessarily Maxwellian. Instead, the distribution function should be computed by modeling the transition between the collisional and the collisionless plasma. While this is a complicated problem, outside the limited scope of this paper, the general result⁸ is a 10 fold increase in mean kinetic energy before the electrons become collisionless. Here the distribution function is viewed as an input to the problem, and, for the purposes of microstability analysis, a Maxwellian is used in lieu of a detailed startup calculation. Insofar as (i) the true asymptotic electron distribution is also monotone decreasing in energy, (ii) the ions would remain Maxwellian during the transition, and (iii) the free energy source is the neutral flow orthogonal to the electron drift, the use of a three temperature Maxwellian for particular stability calculations will not alter the results significantly.

The parallel (to B_{θ}) pressure is defined through the average value of p_{θ} ,

$$r^2 P_{||} = \rho L_{||}^2 = \rho \int d\mu dp_\theta \ F \frac{p_\theta^2}{m^2},$$
 (4a)

and the perpendicular pressure becomes

$$P_{\perp} = \rho B M_{\perp} = \rho B \int d\mu dp_{\theta} F \mu / m . \qquad (4b)$$

Here, and in other moments, the summation over species is implicit.

The axial current density, defined by averaging of the axial drift velocity of the guiding center

$$nev_z \equiv (nc/B) \left(\frac{mv_\theta^2}{r} + mc \frac{D(E/B)}{Dt} - w_\perp \frac{\partial \ln B}{\partial r} \right),$$

is then readily calculated by momentum balance to be

$$J_{z} = \frac{\rho c^{2}}{B} \frac{D(E/B)}{Dt} + \frac{c}{B} \left[\frac{\rho L_{||}^{2}}{r^{3}} - \frac{1}{r} \frac{\partial (r \rho B M_{\perp})}{\partial r} \right]. \tag{5}$$

The first term is related to the acceleration of the $E \times B$ drift motion, the second comes from angular momentum conservation, or P_{\parallel} , and the third is the magnetization contribution, from P_{\perp} . In the acceleration term the ions dominate; the electrons are more important for the two pressure-related terms, without thermal equilibrium between electrons and ions.

In this gyrokinetic description the Maxwell-Vlasov system, as completed by the momentum balance including the anisotropic pressure \overrightarrow{P} , can be summarized in the following equations

$$\partial n/\partial t + \nabla \cdot (nW) = 0$$
, (7a)

$$\partial B/\partial t = \nabla \times (W \times B) , \qquad (7b)$$

$$\nabla \times B = 4\pi J/c + 1/c\partial E/\partial t , \qquad (7c)$$

The displacement current is retained in the analysis in order to make connection with external power sources or sinks. For a cylindrically symmetric geometry the non-vanishing dependent variables are: the fluid density ρ , the radial component of the fluid velocity $W_r = cU$, the axial component of the current density $J_z = J$, the azimuthal component of the magnetic field $B_\theta = B$, and the parallel and perpendicular moments L_{\parallel} and M_{\perp} .

In the limit of homogeneous compression $(U \propto r)$, special initial conditions in these variables allow the equations to simplify. The dependent variables and their derivatives are then functions of the single self-similar invariant $\xi = r/r_{\star}\alpha(\tau)$. Here r_{\star} is a dimensionless scale length which arises directly in the transformation, viz. $r_{\star} \equiv \omega_{\dot{E}}/\omega_A = r_{\star}/l_0$ with $ct_0 = l_0$ and $\tau = t/t_0$. The time scale t_0 is a free parameter only to the extent that a particular implosion timescale for the core plasma remains arbitrary. The variable $\alpha(\tau)$ contains the sole time dependence, e.g. $U = \dot{\alpha}r_0$, $DU/D\tau = \ddot{\alpha}r_0$.

A self-similar oscillation is possible only when the accelerations are proportional to the pinch radius. For an isotropic pressure the proportionality of $J_z B_\theta/n$ to radius implies that the magnetic field is proportional to $\sqrt{\rho}$. In the anisotropic case additional profiles must be defined self-consistently. Using Eq. (7c) to eliminate J, and separating the four distinct spatial dependencies that arise,

$$\ddot{\alpha} = \frac{\omega_{\parallel}^2}{\alpha^3} + \frac{\omega_{\perp}^2}{\alpha^2} - \frac{\omega_{A}^2}{\alpha} + \frac{\omega_{\dot{E}}^2}{\alpha} \dot{\alpha}^2. \tag{8}$$

The oscillatory term related to the magnetic field pressure is $-\omega_A^2/\alpha$, where $\tau_A = \omega_A^{-1}$ is the transit time of an Alfven wave with velocity c_A through the pinch scale length r_{\star} , viz. $\omega_A^2 \equiv c_A^2/c^2 = B^2/4\pi\rho c^2$. As expected this term also occurs in the corresponding equation for the isotropic ideal hydromagnetic case. The two new terms related to the anisotropy are the parallel pressure term, with $\omega_{\parallel}^2 \equiv c_{\parallel}^2/c^2$; and the perpendicular pressure term, with $\omega_{\perp}^2 \equiv c_{\perp}^2/c^2$. The velocities c_A , c_{\parallel} , and c_{\perp} are thus alternate measures of the strengths of the fundamental moments in the theory, serving to parametrize the corresponding separation constants. Each dimensionless frequency $(\omega_k \equiv \tau_k^{-1})$ derives from a separate term in the momentum equation,

the velocity ratios obtain from the normalization of the moments to the light speed and the required dimensionality, viz. $L_{\parallel}^2 \sim l_0^2 c_{\parallel}^2 h_{\parallel}(\xi)$ and $BM_{\perp} \sim c_{\perp}^2 h_{\perp}(\xi)$. The final term, proportional to $\dot{\alpha}^2$, arises here only when we keep the full effects of displacement current; $\tau_{\dot{E}} = \omega_{\dot{E}}^{-1}$ is a measure of the overall dielectric strength characterizing any particular flow.

The four frequencies appearing in Eq.(A8) are connected to four constraint relations which define the required plasma profiles for enclosed current $I(\xi) = (\frac{cl_0 r_{\pm}}{2}) \xi B_0(\xi)$, number density $n_0(\xi)$, perpendicular (kinetic) temperature $h_{\perp}(\xi)$, and parallel (kinetic) temperature $h_{\parallel}(\xi)$. With the dielectric coefficient $\varepsilon(\xi)$ given by

$$\varepsilon(\xi) = \sqrt{1 + \frac{(4\pi m_i c^2) n_0(\xi)}{B_0^2(\xi)}}, \qquad (9a)$$

the constraints are given by

$$\omega_{\parallel}^2 = \frac{c_{\parallel}^2}{c^2} h_{\parallel}(\xi) \left[1 - \frac{1}{\varepsilon^2(\xi)} \right], \tag{9b}$$

$$\omega_{\perp}^{2} = -\frac{c_{\perp}^{2}}{c^{2}} \frac{\left[1 - \frac{1}{e^{2}(\xi)}\right]}{r_{+}^{2} \xi^{2} n_{0}(\xi)} \partial_{\xi} \left[\xi n_{0}(\xi) h_{\perp}(\xi)\right], \tag{9c}$$

$$r_{\star}^{2} = \frac{1 + \xi \partial_{\xi} \ln B_{0}(\xi)}{\varepsilon^{2} \xi^{2}}, \qquad (9d)$$

$$1 = \frac{2 + \xi \partial_{\xi} \ln B_0(\xi)}{\varepsilon^2}. \tag{9e}$$

These equations require $\omega_{\dot{E}} < 1$ to obtain a positive definite number density profiles and offer bounded solutions for each of the variables, usually over a finite range $[\xi_{<}, \xi_{>}]$. The spatial range used can be chosen to fit whatever physical dimensions are imposed because these solutions are simply following the motion of the single particle gyrokinetic trajectories. In other words, clipping these solutions in radius is admissible so long as the profile values and derivatives on the interior of any such domain limit to the proper values as one approaches the boundary.

Quasi-linear Theory for Electrostatic Waves

The equilibrium described above drifts radially inward in response to the averaged stresses arising from tensor pressure gradients, polarization and displacment currents, and the constraints of angular momentum conservation in the azimuthal and r-z degrees of freedom. If the drift velocity U_r is sufficiently great, then the free energy of this radial motion can cross couple to the azimuthal direction and excite electrostatic waves, which in turn serve to heat the coronal plasma in the azimuthal direction, as measured by T_{\parallel} . The gyrokinetic equation for $f = gF_o + f_1$, with $g = \frac{mrn}{2\pi B}$ the only equilibrium component which depends explicity on spatial variables and F_o a function only of strict invariants along the guiding center orbit, can be written

$$Lf_1 = -\frac{q}{m} E_{\theta} g F_o \partial_{u_{\theta}} ln F_o , \qquad (10)$$

with the characteristics of the guiding center determined by solutions to the drift operator acting on the LHS, viz.

$$Lf = \{\partial_t + U_r \partial_r + \frac{u_\theta}{r} \partial_\theta - \frac{U_r u_\theta}{r} \partial_{u_\theta}\} f.$$
 (11)

The equilibrium nature of $f_o = gF_o$ is reflected in the fact that $Lf_o = 0$, and one can write the formal solution for f_1 using the orbit propagator

$$\Pi(t,t_1) = exp - \int_{t_1}^t d\tau_2 \{ U_r \partial_r + \frac{u_\theta}{r} \partial_\theta - \frac{U_r u_\theta}{r} \partial_{u_\theta} \} (\tau_2)$$
 (12a)

as

$$f_1 = -\int_{t_o}^t d\tau_1 \Pi(t, t_1) \left\{ \frac{q}{m} g F_o \partial_{u_\theta} ln F_o \right\} E_\theta(\tau_1)$$
 (12b)

Transforming to Fourier components (k,ω) , inserting the special forms for the characteristics of the self-similar equilibria, with the approximations that (i)

$$r_o \alpha(\tau) \approx r_o (1 - \frac{U_r \tau}{r_o})$$
, (13a)

$$\int_{o}^{\tau} d\tau_{1}/\alpha(\tau_{1})^{2} \approx \tau/\alpha^{2} , \qquad (13b)$$

in the limit that $U_r\tau \ll r_o$, produces the Fourier components of the perturbed distribution. After averaging the $f_1(k,\omega)$ result to form the current density $j_1(k,\omega)$ and forming the conductivity tensor, the dielectric function for the gyrokinetic plasma becomes

$$D(\xi) = 1 + (\frac{k_D}{k})^2 [D_e(\xi_e) + D_i(\xi_i)]$$
 (14a)

$$D_{e}(\xi_{e}) = (\frac{T_{i}/T_{e}}{\xi_{e} - \Delta})(i\nu + (\xi_{e} + 2i\nu(\xi_{e}^{2} - 1))(1 + i\xi_{e}\Lambda(\xi_{e})))$$
(14b)

$$D_i(\xi_i) = Z(1 + i\xi_i\Lambda(\xi_i)) \tag{14c}$$

The fundamental variables which set the scale for the arguments of Λ , the plasma dispersion function, are given by

$$\Delta = \delta_e \frac{kU_r}{\omega_{pi}} ,$$

which measures the strength of the radial ExB drift (U_r) and kr_o , which measures the number of oscillations around an azimuthal flux tube. From these are constructed three auxilliary scale factors appearing in Eqn. 14, viz.

$$\nu = \frac{\sqrt{2}}{kr_o} \delta_e \Delta \ ,$$

$$\xi_e = \delta_e(\frac{k}{k_{Debue}}, \frac{T_{e,\parallel}}{T_i})[\omega + i\gamma - \Delta \sin\theta \cos\phi]$$
,

and,

$$\xi_i = \delta_i \left(\frac{k}{k_{Debue}}\right) [\omega + i\gamma] .$$

The angles appearing above denote the direction of the electrostatic wave's propagation relative to two basic directions, i.e. $\cos \theta = \hat{k} \cdot \hat{\theta}$ and $\cos \phi = \hat{k} \cdot \hat{r}$. The fundamental set of independent variables that serves to characterize the propagation is then kr_o , Δ , and $\frac{T_{e,\parallel}}{T_i}$.

Results

The spectrum of unstable modes arising from the gyrokinetic dielectric function is most readily classified according to propagation angle. In the figures below the complex plane has been transformed to the domain of complex phase velocity rather than frequency because it is easier to examine the variation of the root with $\frac{k}{k p_{chie}}$.

The modes which propagate against the radial drift, normally denoted "negative energy" waves, are in fact **stable**. This is in sharp contrast to the usual ion sound instability which destabilizes an ordinarily Landau damped root in the negative real frequency domain and thus preferentially grows in the direction opposite to the electron drift. If one examines the evolution of complex roots in the case of "counter streaming" propagation, the increase in drift speed draws a new stable root from the origin (Fig. 5a,b,c), at fixed wavenumber. Fixing the drift parameter and lowering the wavenumber from $2k_{Debye}$, this stable root displaces a root near the origin and moves it to higher (real) phase velocity (Fig. 5d,b,e).

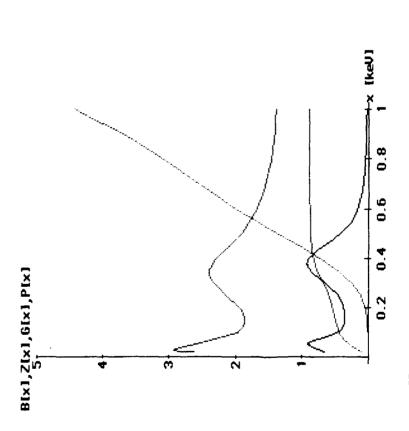
If we now turn to mode propagating along the drift, "costreaming propagation", a similar series of plots now reveals the instability. Fixing the wavenumber the increase in drift speed draws a root from the origin as before, but it becomes more unstable monotonically as the drift parameter is increased (Fig. 6a,b,c). Fixing the drift parameter and lowering the wavenumber from $2k_{Debye}$, this unstable root first increases its growth rate and then decreases it as the (real) phase velocity magnitude becomes larger.

The unstable branch generally grows faster at higher drift velocities and lower electron temperatures, as indicated in Fig. 7a,b. The faster growth rates exceed similar ion sound growth rates by perhaps a factor of three, and thus one can expect a fair amount of turbulence to be generated by this phenomena. Just how much depends sensitively on the saturation mechanisms which will operate here. Since there is a manifold of stable roots just across the $\sigma=0$ line, the usual Landau damped solutions, the mode conversion to each of these in turn at the lower values of wavenumber (as the real part of the unstable mode crosses the real part of the stable modes) would be likely to saturate the lower end of the k space. Since the stable counter streaming wave also has a similar magnitude to its real part, it too would be expected to mode couple to the growing mode. Finally since the turbulence would be expected to heat the azimuthal velocity component, the increase in $\frac{T_{e,\parallel}}{T_i}$ with turbulence amplitude would be expected to lower the growth rate. The resolution

of these various saturation channels is presently under investigation.

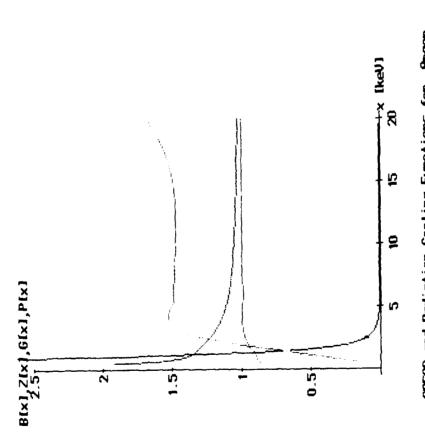
References

- 6. R. E. Terry, in NRL Memorandum Report 6051(1987), p. 49 ff.
- 7. R.E. Terry, to appear in PFB.



CMEOS and Radiation Cooling Functions for Argon Branching Ratio: BLx1, Ionization: $\{Z[x] \ / \ 18\}$, Grayness: G[x], Cooling Power: $\{P[x] \ / \ 5.0 \ E$, IkeU/s]

Figure la



CMEOS and Radiation Cooling Functions for Argon Branching Ratio: Blx], Janization: {Zlx] / 18}. Grayness: {100 Glx] }, Cooling Power: {Plx] / 5.0 E 9 [keU/s]}

Wirare 1b

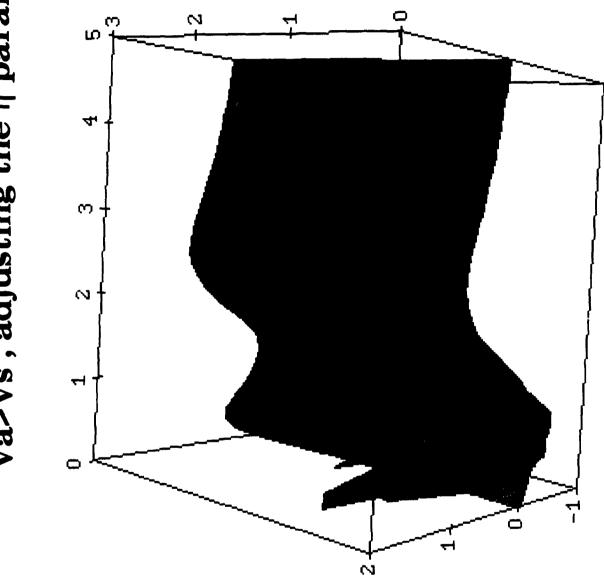


Figure 2a

Va<Vs, adjusting the n parameter.

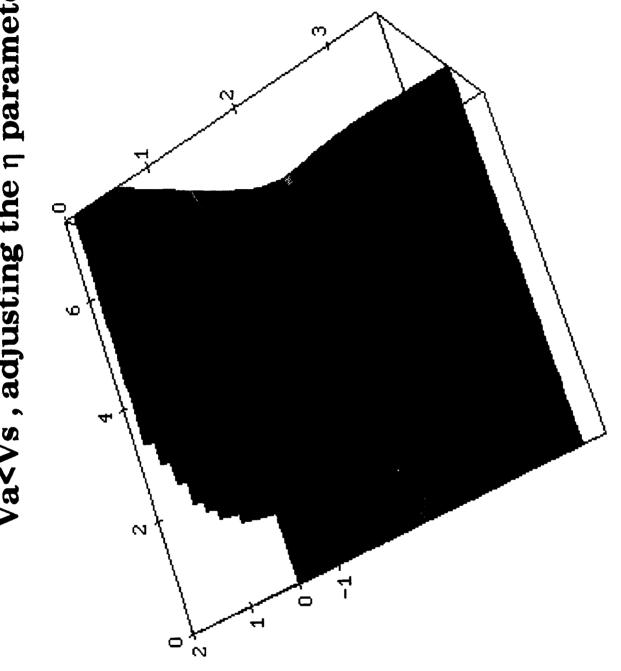
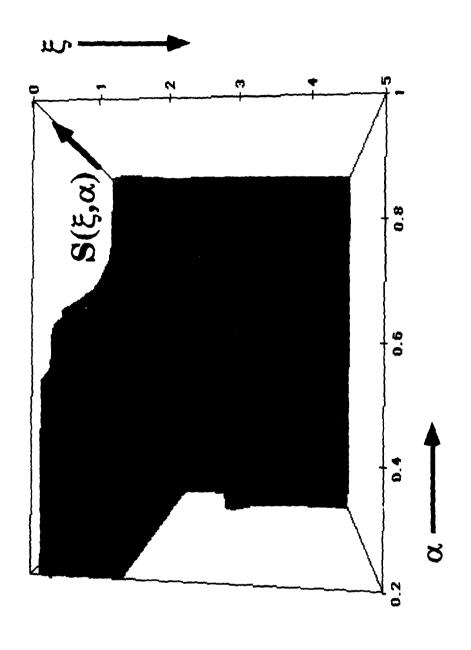
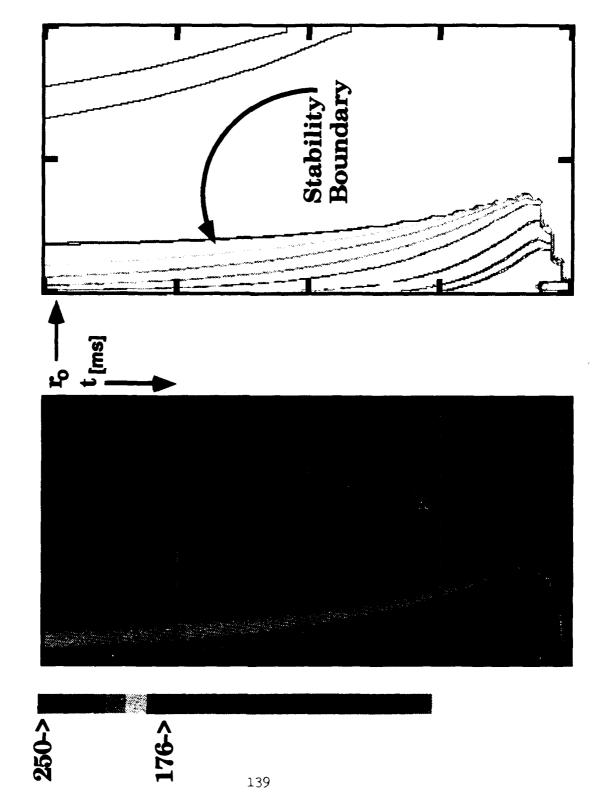


Figure 2b



and adiabatic compression ratio α , at areturn cage winding $N_{wnd} = 0.0$, and axial flow $\eta = v_{\mathbf{r}}(\mathbf{x})/v_{[A,z]} = [10.0]$ as a function of radius ξ=r/ao Suydam Stability Criterion



Map of the Gyroacoustic Dispersion Relation θ =45, ϕ =0, u/v = 0.05, kr=1000, k=kD

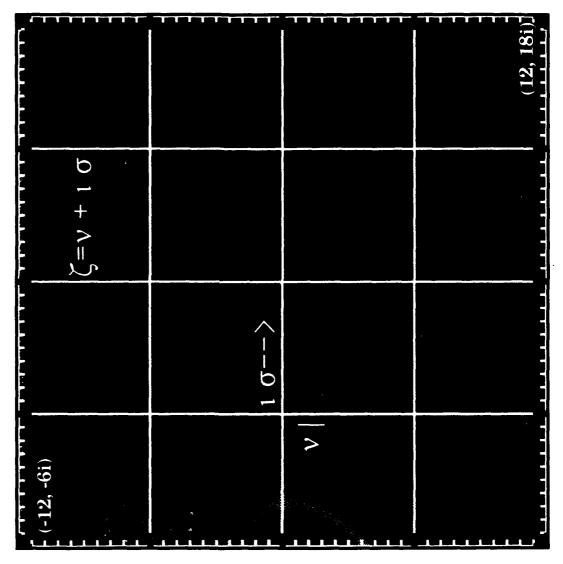


Figure 5a

Map of the Gyroacoustic Dispersion Relation θ =45, ϕ =0, u/v = 6.0 , kr=1000, k=kD

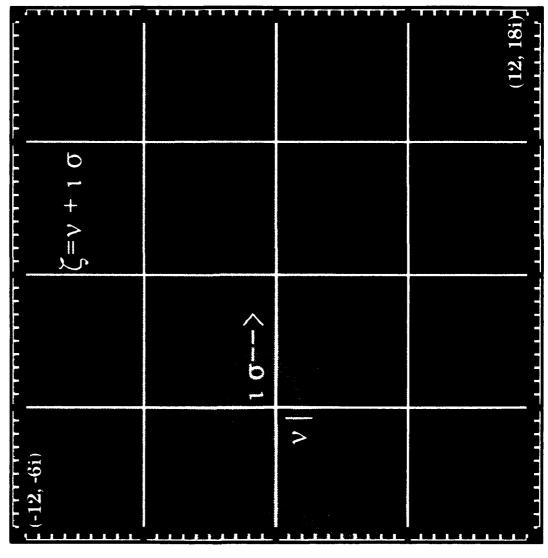


Figure 5b

Map of the Gyroacoustic Dispersion Relation θ =45, ϕ =0, u/v = 15.0 , kr=1000, k= kD

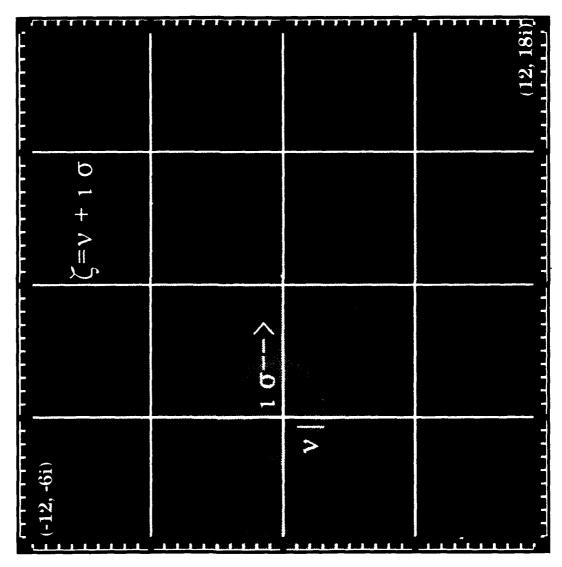


Figure 5c

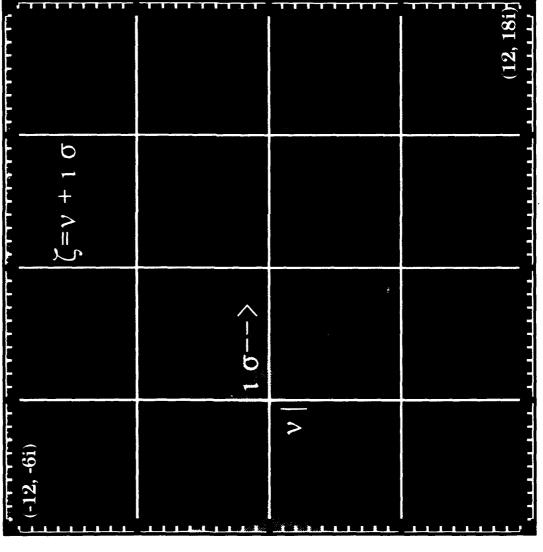


Figure 5d

Map of the Gyroacoustic Dispersion Relation θ =45, ϕ =0, u/v = 6.0 , kr=0500, k= 0.5 x kD

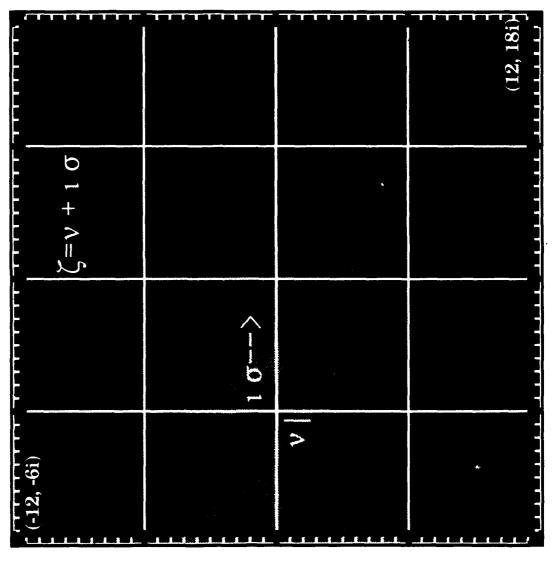


Figure 5e

			18i)
			18
			(12,
ζ=ν + 1 σ			
			
+			
>			
.			
5			
*			
	^		
			5
	0		
	Q		
	, , , , , , , , , , , , , , , , , , , 		
			_
		>	
(-12, -6i)			
9-			
. <u>%</u>		MALE A	
<u> </u>			

Figure 6a

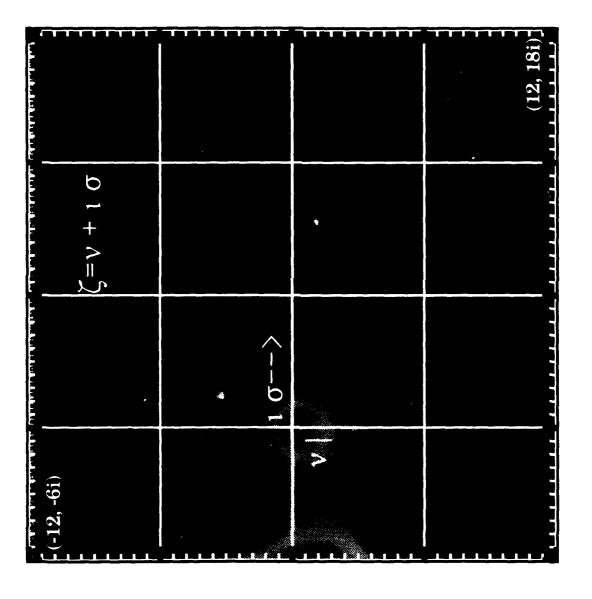


Figure 6b

Map of the Gyroacoustic Dispersion Relation $\theta=45$, $\phi=180$, u/v=15.0, k=1000, k=kD

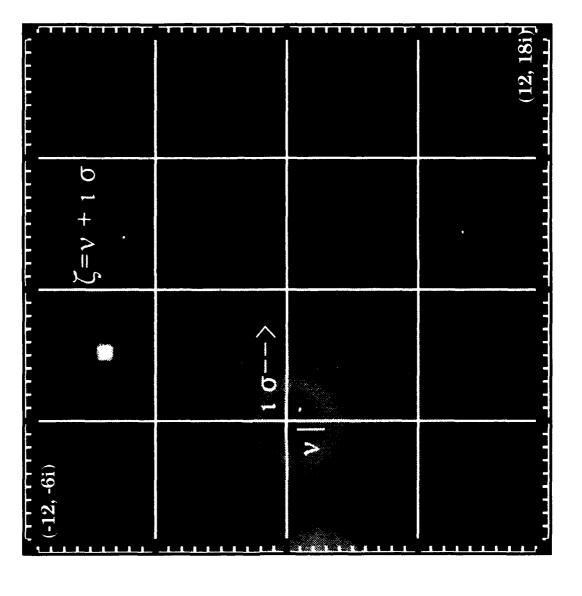


Figure 6c

Map of the Gyroacoustic Dispersion Relation $\theta=45$, $\phi=180$, u/v=6.0, k=2000, $k=2 \times kD$

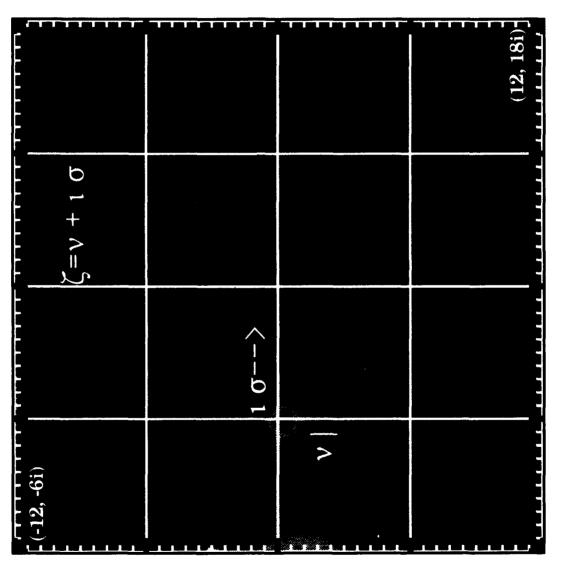


Figure 6d

Map of the Gyroacoustic Dispersion Relation $\theta=45$, $\phi=180$, u/v=6.0, kr=0500, k=0.5 x kD

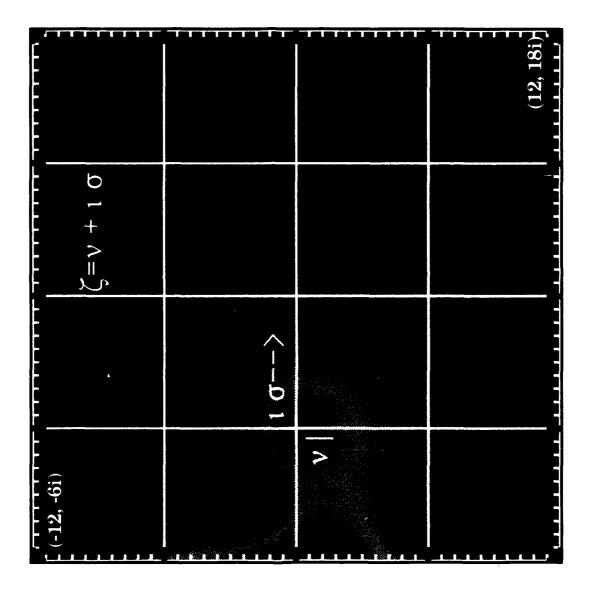
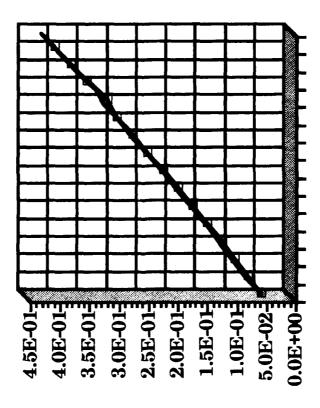


Figure 6e

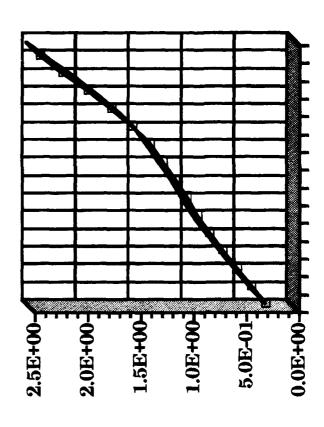
Growth Rate Variation with Drift Speed

* Hot/Cold Electrons with $\Delta = [50,300]$, γ in units of ω pi.



161

+ Hot

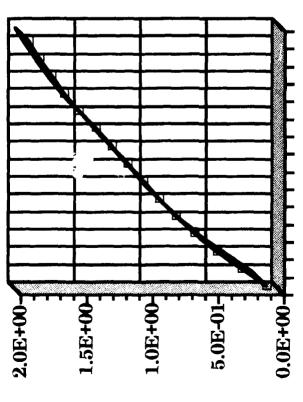


+ Cold

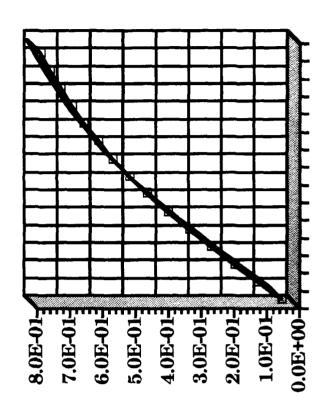
Figure 7a

Growth Rate Variation with Temperature





+ Fast



4 Slow

Plympe T